RAMAN SPECTRA AND OPTICAL ABSORPTION ANALYSES OF CARBONEOUS FILMS DEPOSITED FROM C_{60} IN NITROGEN ENVIRONMENT BY PULSED LASER DEPOSITION

Ahmed Zubair

MASTER OF SCIENCE IN ELECTRICAL AND ELECRONIC ENGINEERING

Department of Electrical and Electronic Engineering

BANGLADESH UNIVERSITY OF ENGINEERING AND TECHNOLOGY

October, 2011

CHAPTER 1

INTRODUCTION

Silicon, which is much available semiconductor, has been widely used. Though silicon have dominated the market for the last few decades, scientists are always on the lookout for new materials that ultimately reduces costs or provide improved performance relative to silicon for electronic applications, optoelectronic applications and high speed devices. Carbon has attracted the attention of researchers because it has some good properties over other semiconducting materials like silicon. Interestingly, carbon has several properties that can be tailored over an unusual wide range from that of semi-metallic graphite to that of insulating diamond. Due to its extraordinary tunable characteristics, extensive work is done for its application especially in mechanical, bio-medical, electronic and industrial applications [1-3] for the last few decades. Diamond like carbon (DLC) based chips are desirable because they can operate at high temperature, handle very high power, and operate in high radioactive environments. Besides this, carbon is found in nature in numerous amorphous forms. The DLC and amorphous carbon have high defects and their doping is difficult. Furthermore with the discovery of a new class of carbon materials, fullerene, by Kroto *et al.* [4] in 1985, and specially after synthesizing macroscopic quantities of C_{60} by Krätschmer *et al.* [5] in 1990, carbon research has opened several new directions because of the many interesting properties and notable extremely small feature size of this form of carbon allotrope. Effort is being made in the direction of electronic device applications fullerene [6, 7] and its photovoltaic (PV) properties are also investigated. PV solar cells reveal the technological potential of fullerene films in solid state [8, 9] and organic [10, 11] solar cell.

1.1 Background

The carboneous thin films produced from C_{60} have disorder and defects resulting less mobility. Again to make C_{60} suitable for electronic device applications a semiconducting film i.e. doped film produced from it is necessary. Doping of C_{60} is

difficult and C_{60} doping is yet to be reported. Again, for organic solar cell applications, doping of C_{60} is necessary because of low conductivity of the constructing organic materials. The carbon films film produced from C_{60} reported earlier to be amorphous and many energy states is present in the shallow region of energy band resulting in broad optical absorption spectra. Because of weak van der Waals force Fullerene (C_{60}) is chemically unstable and that's why the study of modification of C_{60} is continued since its discovery. Modification in structure of C_{60} makes C_{60} more useful in various applications [12-16] since its physical and chemical characteristics are changed. Modifications of physical properties are reported by various research groups [17-23].

Bajwa *et al.* [17] deposited C_{60} on various substrates such as Si and quartz using resistive heating method. High fluence irradiation results in submolecular formations and amorphous semiconducting carbon, indicating overall damage (fragmentation) of the fullerene molecules. Voevodin *et al.* [24] investigated the growth and the structure of fullerene like CN_x films produced by laser ablation of graphite in low pressure nitrogen. Lotha *et al.* [19] studied the heavy ion irradiated films produced from C_{60} by Raman spectroscopy which indicated polymerization and damage of the film with ion fluence. Zauco *et al.* [21] made an experiment to grow C_{60} thin films by physical vapor deposition (PVD) onto Si substrates at room temperature in a vacuum chamber kept at 10^{-6} Torr and found The optimal experimental conditions for fullerene photopolymerization for areas larger than 1 cm^2, reducing the undesirable formation of other carbon phases. Karachevtsev *et al.* [16] performed the simultaneous deposition and irradiation. The photopolymerization process was monitored as a function of irradiation time using Raman and infrared (IR) spectroscopy. Electron microscopy and diffraction studies revealed the amorphous nature of the photopolymerized films which comprised of crystals with a linear dimension of ~40–60 nm.

Stimpel *et al.* [25] studied the growth of fullerene C_{60} on Si(111) surfaces. They found that due to the high density of dangling bonds on the Si surface and the resulting low-surface mobility of C_{60}, neither the growth of monocrystalline layers of C_{60} nor a reconstruction of C_{60} is possible on this surface. Dharmarasu *et al.* [26] investigated conductivity control of the boron and phosphorus ion implanted C_{60} films subjected to various doses of multiple energies. Temperature dependent

conductivity shows the semiconducting nature of the B^+ and P^+ implanted films. The B^+ and P^+ implantation into C_{60} and amorphous carbon suggests the possibility of fabricating carbon based homojunction solar cells. Narayanan *et al.* [9] deposited thin films of C_{60} on *p*-type Si (100) wafer which are implanted with low energy phosphorous ions for the photovoltaic applications. But they have found low efficiency of thin films which is attributed to the ion implantation induced damage effects and subsequent larger series resistance values. Mominuzzaman *et al.* [22] deposited the polymeric semiconducting carbon films on silicon and quartz substrates by excimer (XeCl) pulsed laser deposition (PLD) technique using fullerene C_{60} precursor and varying the substrate temperature and found its better crystalline structure compared to the typical amorphous carbon films and more suitable for device such as, optoelectronic applications. Nitrogen (N_2) is reported to modify the carbon films by numerous researchers [27-29].

N_2 incorporation in C_{60} is not experimented yet except Mominuzzaman *et al.* Again doping of C_{60} by N_2 incorporation is yet to be reported. The optical and structural properties of the carboneous films from C_{60} precursor after N_2 incorporation are not studied. In order to understand the structural and optoelectronic modification of the carboneous films produced in nitrogen environment using C_{60} as target material, in depth study on the these films is necessary.

1.2 Objective of the Work

Thin films were deposited from C_{60} precursor in vacuum and under nitrogen environment at room temperature and the Raman, transmittance and reflectance spectra of the films was measured earlier. In this work, these experimentally obtained data was collected and used to investigate the electronic, structural and optical properties of the films. Raman spectra are investigated to study of structural modification of the films deposited under vacuum condition and nitrogen environment. Optical absorption behavior of the thin film is found from the reflectance and transmittance spectra. Urbach region density of states resulting from structural disorder is also investigated from the optical absorption coefficient. Structural properties obtained from Raman spectra are correlated with that resulted from optical absorption behavior. Characteristics of the deposited films are

compared with those carbon films deposited from camphor and graphite precursor. With all the parameters found from analyses, the scope of electronic device application of the deposited thin films is outlined.

1.3 Thesis Layout

The organization of this thesis is divided into four chapters.

Chapter one provides general introduction followed by the background and the objective of the work.

Chapter two covers the review on carbon, C_{60} and related materials and their optoelectronic application. The review of carbon materials has been described elaborately. A broad review on fullerene (C_{60}) is presented in the chapter. Basic principle of Raman Scattering is also reviewed. Different intramolecular and intermolecular modes of Raman of Fullerene are discussed extensively. The principle of curve fitting technique for the analysis of Raman spectra are presented in the chapter. The theory of finding band gap and Tauc parameter from the experimental transmittance and reflectance data is described in this chapter.

Chapter three shows the results and discussions of analysis of Raman Spectra, optical absorption behavior of nitrogen incorporated carboneous thin films. The detailed investigation of the fitted spectra for determination the effect of nitrogen incorporation in fullerene film deposition is shown in this chapter. The band gap and Urbach region density of states is also investigated from the optical absorption coefficient. Structural properties found from Raman Spectra are correlated with that found from optical absorption behavior. Characteristics comparison between of the deposited films and those carbon films deposited from camphor and graphite precursor is given in this chapter. A model for the characteristics peak as the combination of Gaussian and Lorentzian line shape as a function of NPP is proposed. An overall discussion using the results of the analyses is made at end section of the chapter.

Chapter four provides conclusive discussions and remarks for the work. Some scopes for the future works in relation with the present study are also presented in the chapter.

CHAPTER 2

REVIEW ON CARBON, C_{60} AND RELATED MATERIALS AND THEIR OPTOELECTRONIC PROPERTIES

2.1 Review of Carbon

Carbon is unique as an electronic material. It can be a good metal in the form of graphite, a wide gap semiconductor in the form of diamond or fullerenes, a superconductor when intercalated with appropriate guest species, or a polymer when reacted with hydrogen and other species. Furthermore, carbon-based electronic materials provide examples of materials showing the entire range of dimensionalities from fullerenes, which are zero-dimensional quantum dots, to carbon nanotubes, which are one-dimensional quantum wires, to graphite, a two-dimensional layered anisotropic material, and finally to diamond, a three-dimensional wide gap semiconductor. In this section, graphite, diamond, diamond like carbon, hydrogenated carbon is reviewed. Fullerene is extensively reviewed in the next section.

2.1.1 Graphite

The mineral graphite is one of the allotropes of carbon. It was named by Abraham Gottlob Werner in 1789 from the Greek γραφειν (graphein): "to draw/write", for its use in pencils, where it is commonly called lead, as distinguished from the actual metallic element lead. Unlike diamond (another carbon allotrope), graphite is an electrical conductor, a semimetal, and can be used, for instance, in the electrodes of an arc lamp. Figure 2.1 shows the structure of graphite. Graphite holds the distinction of being the most stable form of carbon under standard conditions. Therefore, it is used in thermochemistry as the standard state for defining the heat of formation of carbon compounds. Graphite may be considered the highest grade of

coal, just above anthracite and alternatively called meta-anthracite, although it is not normally used as fuel because it is hard to ignite.

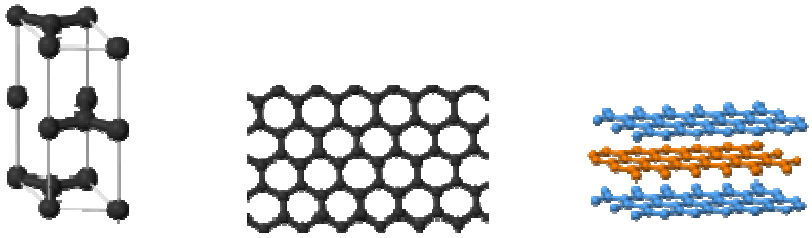

(a) (b) (c)

Figure 2.1 Graphite structure (a) Graphite cell, (b) Graphite layer and (c) side view of layer stacking

Graphite is used in steelmaking industries. Natural amorphous and fine flake graphite are used in brake linings or brake shoes for heavier (nonautomotive) vehicles. Natural graphite has found uses as the marking material ("lead") in common pencils, in zinc-carbon batteries, in electric motor brushes, and various specialized applications. Graphite can be used as Electrode. Graphite (carbon) fiber and carbon nanotubes are also used in carbon fiber reinforced plastics, and in heat-resistant composites such as reinforced carbon-carbon (RCC). Synthetic graphite also finds use as a matrix and neutron moderator within nuclear reactors. Graphite also has the interesting property that, under certain conditions, it can serve as a form of armor against nuclear weapons.

2.1.2 Diamond

Diamond (from the ancient Greek ἀδάμας, adámas) is the allotrope of carbon where the carbon atoms are arranged in an isometric-hexoctahedral crystal lattice. After graphite, diamond is the second most stable form of carbon. Its hardness and high

dispersion of light make it useful for industrial applications and jewelry. It is the hardest known naturally occurring mineral. It is possible to treat regular diamonds under a combination of high pressure and high temperature to produce diamonds that are harder than the diamonds used in hardness gauges.

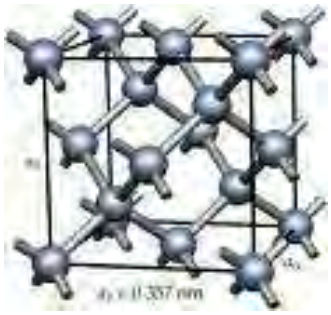

Figure 2.2 Structure of Diamond

Diamond is tough material. Diamond is electrically nonconductive and has high thermal conductivity and is thermally stable. Figure 2.2 shows the structure of diamond.

2.1.3 Amorphous Carbon and Hydrogenated Carbon

Amorphous carbon or free, reactive carbon, is an allotrope of carbon that does not have any crystalline structure. As with all glassy materials, some short-range order can be observed. Amorphous carbon is often abbreviated to a-C for general amorphous carbon, a-C:H for hydrogenated amorphous carbon, or to ta-C for tetrahedral amorphous carbon (also called diamond-like carbon). Figure 2.3 shows the ternary phase diagram of H free and hydrogenated carbon.

Diamond-like carbon (DLC) is an amorphous carbon with a significant fraction of C-C sp^3 bonds [1, 30]. Tetrahedral amorphous carbon (ta-C) is the DLC with the

maximum sp^3 content. We classify hydrogenated amorphous carbons into four classes:

(1) a-C:H films with the highest H content (40–60%). These films can have up to 70% sp^3. However, most of the sp^3 bonds are hydrogen terminated, and this material is soft and with low density. We call these films polymer-like a-C:H (PLCH). Their band gap is above 2 eV and can reach 4 eV [1].

(2) a-C:H films with intermediate H content (20–40%). Even if these films have a lower overall sp^3 content, they have more C-C sp^3 bonds compared to PLCH. Thus, they have better mechanical properties. Their optical gap is between 1 and 2 eV [1].We call these films diamond-like a-C:H (DLCH).

(3) Hydrogenated tetrahedral amorphous carbon films (ta- C:H). ta-C:H films are a class of DLCH for which the C-C sp^3 content can be increased whilst keeping a fixed H content. Thus, most films defined in literature as ta-C:H are just DLCHs. However, the ta-C:H films with the highest sp^3 content (~70%) and ~25 at.% H content do really fall in a different category as also shown by their Raman spectra, their higher density (up to 2.4 g/cm^3) and Young's Modulus (up to 300 GPa) [31]. The optical gap can reach 2.4 eV [32].

(4) a-C:H with low H content (less than 20%). They have a high sp^2 content and sp^2 clustering. The gap is under 1eV. We call these films graphite-like a-C:H(GLCH).

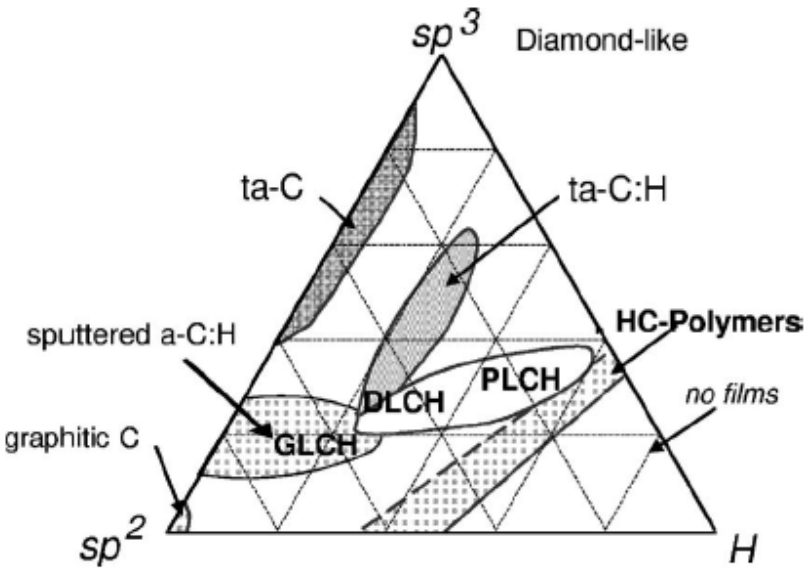

Figure 2.3 Ternary phase diagram for H free and hydrogenated amorphous carbon[33]

The key parameters of interest in such materials are

(1) the sp^3 content;

(2) the clustering of the sp^2 phase;

(3) the orientation of the sp^2 phase;

(4) the cross-sectional nanostructure;

(5) the H content.

Applications of DLC typically utilize the ability of the material to reduce abrasive wear. Tooling components, such as endmills, drill bits, dies and molds often use DLC in this manner. DLC is also used in the engines of modern supersport motorcycles, Formula 1 racecars, NASCAR vehicles, and as a coating on hard-disk platters and hard-disk read heads to protect against head crashes. Virtually all of the multi-bladed razors used for wet shaving have the edges coated with hydrogen-free DLC to reduce friction, preventing abrasion of sensitive skin. Some forms have been certified in the EU for food service and find extensive uses in the high-speed actions involved in processing novelty foods such as "chips" and in guiding material flows in packaging foodstuffs with plastic wraps. DLC coats the cutting edges of tools for the high-speed, dry shaping of difficult exposed surfaces of wood and aluminum, for example on automobile dashboards. The implantable human heart pump can be considered the ultimate biomedical application where DLC coating is used on blood contacting surfaces of the key components of the device. Other medical applications such as Percutaneous coronary intervention employing brachytherapy find additional benefits from the unique electrical properities of DLC. At low voltages and low temperatures electrodes coated with DLC can emit enough electrons to be arranged into disposable, micro-X-ray tubes as small as the radioactive seeds that are introduced into arteries or tumors in conventional brachytherapy. The same dose of prescribed radiation can be applied from the inside, out with the additional possibility to switch on and off the radiation in the prescribed pattern for the X-rays being used.

2.2 Review of Fullerene

2.2.1 Introduction

In carbon family of electronic materials, fullerenes are one of the newest additions and the subject of this review. Fullerene solids differ from conventional electronic materials because, in common with most polymeric materials, the fullerene molecule is the fundamental building block of the crystalline phase. This basic difference in structure is reflected in the electronic structure and properties that are summarized here. The modifications to the structure and electronic properties produced by alkali-metal doping are then reviewed. Potential applications for fullerene-based electronic materials are suggested. In early gas phase work, a molecule with 60 carbon atoms was established experimentally by mass spectrographic analysis [4], and it was conjectured that C_{60} had icosahedral symmetry. The name of fullerene was given to this family of gas phase molecules by Kroto & Smalley [4] because of the resemblance of these molecules to the geodesic dome designed and built by R. Buckminster Fuller [34]. The name Buckminster fullerene simply "buckyball" was given specifically to the C_{60} molecule. In the early gas phase work, the fullerene molecules were produced by the laser vaporization of carbon from a graphite target in a pulsed jet of helium [4]. In the fall of 1990, a new type of condensed matter, based on C_{60}, was synthesized for the first time by Krätschmer, Huffman, and co-workers [5], who found a simple carbon arc method for preparing gram quantities of C_{60}, which had previously only been available in trace quantities in the gas phase [4, 35]. The availability of large quantities of fullerenes provided a great stimulus to this research field. It was soon found [36] that the intercalation of alkali-metals into C_{60} to a stoichiometry M_3C_{60} (where M = K, Rb, Cs) greatly modifies the electronic properties of the host fullerenes and yields relatively high transition temperature ($18 \leq T_c \leq 40$ K) superconductors [37]. The discovery of superconductivity [38, 39] in C_{60} compounds further spurred research activity in this field of C_{60}-related materials. This section reviews synthesis of fullerenes, the structure of fullerene molecules and of their crystalline forms, their electronic structure and optical properties and possible application of fullerene.

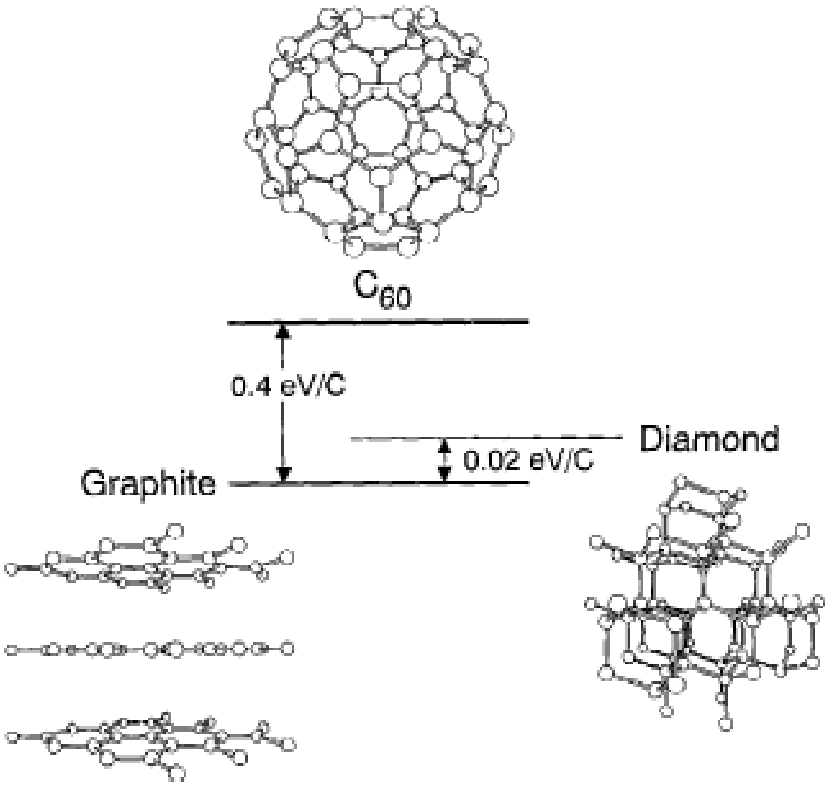

Figure 2.4 Schematic showing the relationship between the crystal structures of the three forms of carbon and their relative binding energies per carbon atom. Under normal conditions there are energy barriers present that prevent the spontaneous conversion of C_{60} to diamond or graphite [40].

2.2.2 Production of Fullerene:

C_{60} has often been referred to as the third form of carbon, after diamond and graphite. Figure 2.4 shows the relationship between the crystal structure of these solids and the relative binding energies per carbon atom. Thus graphite with sp^2 bonding, an intraplanar C-C distance of 1.42 Å, and a separation between planes of 3.35 Å is more stable by 0.02 eV/C than diamond [42], which has 3 bonding and a C-C distance of 1.55 Å. This energy is comparable to k_BT at room temperature but, owing to the large activation energy barrier between the two phases diamonds are forever. In contrast, C_{60} with its 1.45 Å single and 1.40 Å double bonds is, in the face-centered cubic structure, 0.4 eV/C less stable than graphite [41, 42]. The barrier inhibiting a C_{60} -diamond transformation is evidently low enough to allow this conversion by the non-hydrostatic compression of C_{60} to pressures of 20± 5 GPa at room temperature [43].

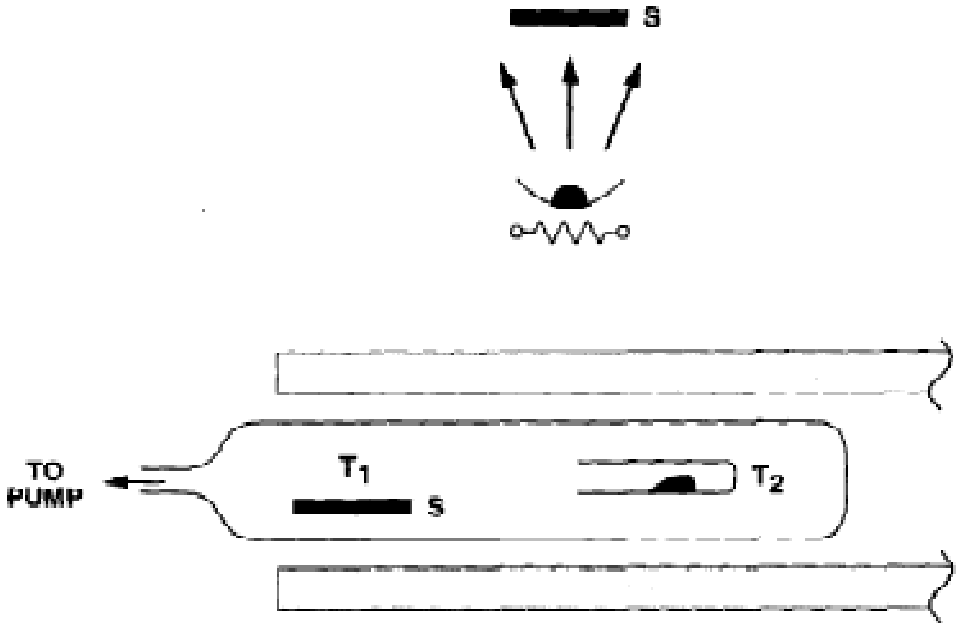

Figure 2.5 C_{60} or C_{70} can be deposited as thin films by vapor sublimation (top) onto either room-temperature or heated substrates (S). Vapor transport in a temperature gradient (bottom) can be used to grow crystals or crystalline films with the size and spacing of the crystals depending on the magnitude and differences between the temperatures T_1 and T_2 [40].

Crystals and films of C_{60} and higher fullerenes can be easily prepared by vapor sublimation [44] (as shown in figure 2.5). In the first, pure C_{60} (or C_{70}) is placed in a temperature-regulated resistively-heated crucible, and the fullerene source material is vacuum sublimated onto a nearby substrate. Sublimation temperatures can be as low as 250°C for pure C_{60} and 300°C for pure C_{70} [45], well below the few thousand degree temperatures that an individual C_{60} molecule survives during formation in the arc furnace. Smooth films with a face-centered cubic (fcc) crystal structure and small grain size (60 Å) can be reproducibly grown [45]. The second sublimation technique (see Figure 2.5 (bottom)) utilizes vapor transport in a temperature gradient [46, 47]. Solid C_{60} is heated in an evacuated quartz tube to approximately 500°C at the hot (T_2) end, and crystals form at the cool (T_1) end. Single crystals with sizes up to 2 mm [47] have been grown, and single crystal diffractometer data are consistent with space group symmetry Fm3 and a fcc unit cell with lattice parameter a = 14.1981 Å [46]. The success these sublimation techniques is facilitated by the relatively high vapor pressure of both C_{60} and C_{70}, which has been directly measured

by the Knudsen effusion thermogravimetric technique and found at 500°C to be ~5.0 x 10^{-4} torr [48].

2.2.3 Structure of Fullerene

We first review the structure of the molecules, followed by a review of the structure of these molecular solids because the structure and properties of fullerene solids are strongly dependent on the structure and properties of the constituent fullerene molecules.

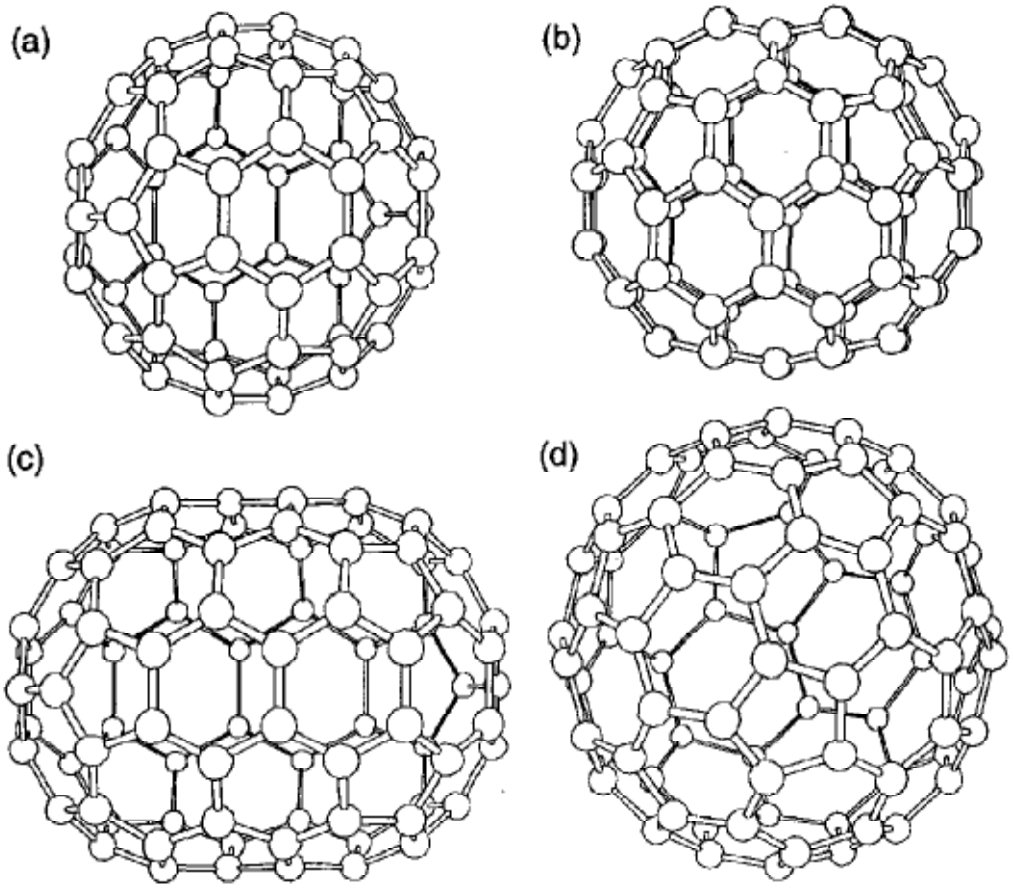

Figure 2.6 (a) The icosahedral C_{60} molecule. (b) The C_{70} molecule as a rugby ball-shaped molecule. (c) The C_{80} molecule as an extended rugby ball-shaped molecule. (d) The C_{80} molecule as an icosahedrons [49].

2.2.3.1 Structure of C_{60}

In C_{60} the 60 carbon atoms are located at the vertices of a regular truncated icosahedron. Every carbon site on the C_{60} molecule is equivalent to every other site (see figure 2.6(a)), consistent with a single sharp line in the NMR spectrum [50, 51]. The average nearest neighbor carbon-carbon (C-C) distance $a_{c\text{-}c}$ in C_{60} (1.44 Å) is almost identical to that in graphite (1.42 Å).

Each carbon atom in C_{60} (like in graphite) is trigonally bonded to other carbon atoms, and most of the faces on the regular truncated icosahedrons are hexagons. Thus many have considered the C_{60} molecule as a rolled-up graphene sheet (a single layer of crystalline graphite). The regular truncated icosahedrons has 20 hexagonal faces and 12 additional pentagonal faces to form a closed shell, in keeping with Euler's theorem, which states that a closed surface consisting of hexagons and pentagons has exactly 12 pentagons and an arbitrary number of hexagons [52]. The symmetry operation of the icosahedrons consists of the identity operation: 6 fivefold axes through the centers of the pentagonal faces, 10 threefold axes through the centers of the hexagonal faces and 15 twofold axes through centers of the edges joining two hexagons. Each of the 60 rotational symmetry operations can be compounded with the inversion operation, resulting in 120 symmetry operations in the icosahedral point group I_h [53] (see figure 2.6(a)). Molecules with I_h symmetry, C_{60} being the most prominent example, have the highest degree of symmetry of any known molecule. The diameter of the C_{60} molecule is 7.10 Å (see table 2.1), treating the carbon atoms as points [1, 54]. The outer diameter of the C_{60} molecule becomes 10.18 Å when taking account of the size of the z-electron cloud associated with the carbon atoms.

From Euler's theorem it follows that the smallest possible fullerene is C_{20}, which would form a regular dodecahedron with 12 pentagonal faces. However, it is considered energetically unfavorable for two pentagons to be adjacent to each other (referred to as the isolated pentagon rule) as this would lead to higher local curvature and high strain on the fullerene molecule. Because the addition of a single hexagon adds two carbon atoms, all fullerenes must have an even number of carbon atoms, in agreement with the observed mass spectra for fullerenes.

Table 2.1 Physical constants for C_{60} materials

Quality	Value	Reference
Average C-C distance	1.44 Å	58
fcc lattice constant	14.17 Å	57
C_{60} mean molecule diameter	7.10 Å	59
C_{60}-C_{60} distance	10.02 Å	57
Tetrahedral site radius	1.12 Å	59
Octahedral site radius	2.07 Å	59
Mass density	1.72 g/cm^3	59
Molecular density	1.44 x 10^{21} /cm^3	59
Compressibility (-d In *V/dP)*	6.9 x 10^{-12} cm^2 /dyn	60
Bulk modulus	14 GPa	61
Structural phase transition	260 K	62
Binding energy per atom	7.40 eV	63
Electron affinity (pristine C_{60})	2.65 eV	64
Ionization potential (1^{st})	7.58 eV	65
Ionization potential (2^{nd})	11.5 eV	66
Volume coefficient of thermal expansion	6.2×10^{-5} /K	67
Bandgap (HOMO-LUMO) [a]	1.7 eV	68
Spin-orbit splitting of C(2p)	0.00022 eV	69
Velocity of sound v_t	2.1×10^5 cm/s	70
Velocity of sound v_l	3.6×10^5 cm/s	70
Thermal conductivity (300 K)	0.4 W/mK	71
Phonon mean free path	50 Å	71
Static dielectric constant	4.0-4.5	72, 73

[a] Strictly speaking, it is the optical absorption edge that is at ~ 1.7 eV.

Although each carbon atom in C_{60} is equivalent to every other carbon atom, the three bonds emanating from each atom are not completely equivalent. Each of the four valence electrons of the carbon atoms are engaged in covalent bonds, so that two of the three bonds are electron poor single bonds, and one is an electron-rich

double bond. Consistent with X-ray diffraction evidence, the structure of C_{60} is further stabilized by introducing a small distortion of the bond lengths to form the Kekulé structure of alternating single and double bonds around the hexagonal face. We note that the icosahedral I_h symmetry is preserved under these distortions. The single bonds that define the pentagonal faces are increased from the average bond length of 1.44 Å to 1.46 Å, whereas the double bonds are decreased to 1.40 Å [55, 56]. As valence requirements of each carbon atom are fully satisfied, the C_{60} molecules are expected to form a nonconducting (an insulator or semiconductor) van der Waals bonded solid.

2.2.3.2 Structure of C_{70} and Higher Fullerenes

In the synthesis of C_{60}, larger molecular weight fullerenes C, (n > 60) are also formed, by far the most abundant being C_{70}. However, significant quantities of C_{76}, C_{78}, C_{84}, and higher mass fullerenes have also been isolated and studied in some detail. C_{70} has been found to exhibit a rugby ball shape [74], and its form can be envisioned by adding either a ring of ten carbon atoms or a belt of five hexagons around the equatorial plane of the C_{60} molecule normal to one of the fivefold axes (see figure 2.6(b)). In contrast to the C_{60} molecule with symmetry, the C_{70} molecule has the lower symmetry D_{5h}, which is a subgroup of I (lacking inversion symmetry). As a carbon atom C_n can correspond to molecules with different geometric structures, Fullerenes often form isomers [74, 75]. For example, C_{80} might formed in the shape of an elongated rugby ball prepared by adding two rows of five hexagons normal to a fivefold axis of C_{60} at the equator (see figure 2.6(c)) and an icosahedral form of C_{80} can also be specified, as shown in figure 2.6d. C_{78}, another example of fullerene isomers, has been shown to have five distinct isomers, one with D_3 symmetry, two with C_{2v} symmetry and two with D_{3h} symmetry [76]. In addition, isomers giving rise to right and left-handed optical activity are expected to occur in molecules belonging to group I (rather than I_h), and not to have inversion symmetry.

2.2.4 Crystalline Structure

The crystalline structure of C_{60} and C_{70}, and various phases have been identified as a function of temperature because of extensive research. Less information is available

about the crystal structure of higher fullerenes. To gain a microscopic understanding of the electronic properties of fullerene solids, knowledge of the structure is necessary.

2.2.4.1 Crystalline C_{60}

The C_{60} molecules crystallize into a cubic structure with lattice constant of 14.17 Å, a nearest neighbor C_{60}-C_{60} distance of 10.02 Å [54], and a density of 1.72 g/cm^3

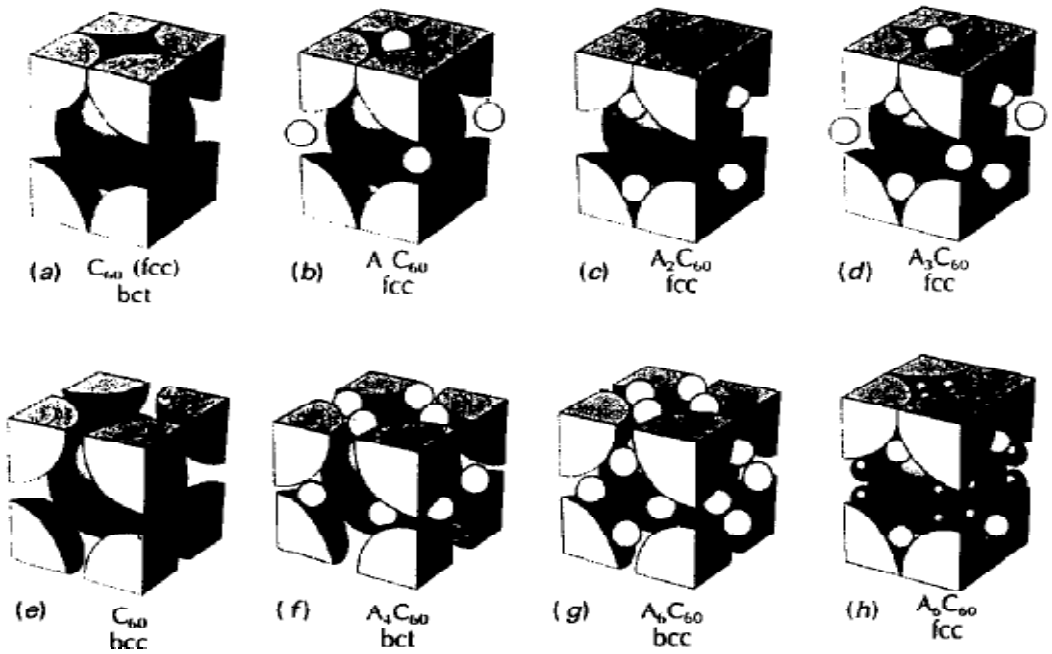

Figure 2.7 Structures for solid (a) C_{60}(fcc), (b) AC_{60}(f cc), (c) A_2C_{60}(fcc), (d) A_3C_{60} (e) C_{60} (bcc), (f) A_4C_{60} (bct), and two structures A_6C_{60}: (g) A_6C_{60} (bcc for (A = K, Rb, Cs); and (h) A_6C_{60} (fcc), which is appropriate for A = Na, using the notation Reference 74. The large balls denote C_{60} molecules, and the small balls denote alkali metal ions. For fcc A_3C_{60}, which has four C_{60} molecules per cubic unit cell, the A atoms can be on either octahedral or tetrahedral sites. Undoped solid C_{60} also exhibits this crystal structure, but in this case, all tetrahedral and octahedral sites are unoccupied. For (h) bcc A_6C_{60}, all the A atoms are on distorted tetrahedral sites. For (f) bct A_4C_{60}, the dopant is also found on distorted tetrahedral sites. For (c) pertaining to small alkali metal ions such as Na, only the tetrahedral sites are occupied. For (h), four Na ions can occupy an octahedral site of this fcc lattice. (here A ≡ M) [49].

(corresponding to 1.44× 10^{21} C_{60} molecules/cm^3) in the solid state. At room temperature, the C_{60} molecules rotate rapidly with three degrees of rotational freedom, and the molecules are arranged on a face-centered cubic (fcc) lattice with one C_{60} molecule per primitive fcc unit cell, or four molecules per simple cubic unit cell (see figure 2.7(a)). The pertinent space group is O_h^5, or *Fm3m* which has been determined by X-ray and neutron diffraction [64, 78, 79]. Relative to the other allotropic forms of carbon, solid C_{60} is relatively compressible, with an isothermal volume compressibility (see table 2.1) of 6.9 × 10^{-12} cm^2/dyn [55]. Below about 260 K, the C_{60} molecules completely lose two of their three degrees of rotational freedom, and the residual rotational motion, described as a ratcheting motion [55, 64, 79], for each of the four molecules within the unit cell is about a different <111> axis. The structure of solid C_{60} below ~ 260 K thus becomes simple cubic (space group T_h^6 or Pa3), with a lattice constant a_0 = 14.17 Å and four C_{60} molecules per unit cell, as the four molecules within the fcc structure become inequivalent (see figure 2.7(a)) [64, 79]. Supporting evidence for the 260 K phase transition provided

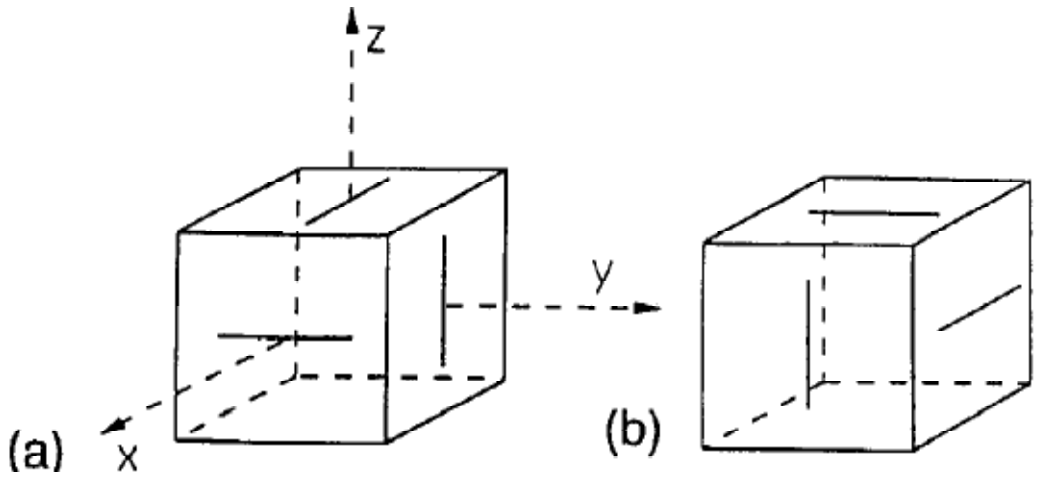

Figure 2.8 (a) One standard orientation for the Cartesian axes in a cubic crystal so that these axes pass through three orthogonal twofold axes. (b) The other standard orientation related to that in (a) by a 90° rotation about any of the Cartesian axes. The inscribed icosahedron has mirror planes perpendicular to the three <100> directions. In this orientation, six of the icosahedral edges lie in planes parallel to the mirror planes so that when the icosahedron is circumscribed by a minimal cube, these edges lie in the cube faces, as shown. Each <111> direction is a threshold axis[80].

by many property measurements [52]. Further ordering of the C_{60} molecules occurs, whereby adjacent C_{60} molecules develop correlated orientations as the temperature lowered below 260 K. The degree of order achieved in the crystal structure at low temperature can be understood by referring to Figure 2.8a, where the standard orientation of a C_{60} molecule is shown with respect to a cubic coordinate system [80]. Here the [100] axes pass through three, mutually orthogonal twofold Molecular axes (the centers of the electron-rich hexagon-hexagon edges), and four <111 > axes pass through the centers of the hexagonal faces. The alternate standard orientation is shown in figure 2.8b, which is obtained from figure 2.8a through rotation by $\pi/2$ about the [100] axes. The two standard orientations are equivalent. So the C_{60} molecules have an approximately many property measurements [52]. Further ordering of the C_{60} molecules occurs, equal probability to be in either of these orientations, leading to what is called merohedral disorder with regard to alignment of the twofold axes. Merohedral disorder persists to the lowest temperatures and contributes to carrier scattering in transport properties. In the low temperature structure, the relative

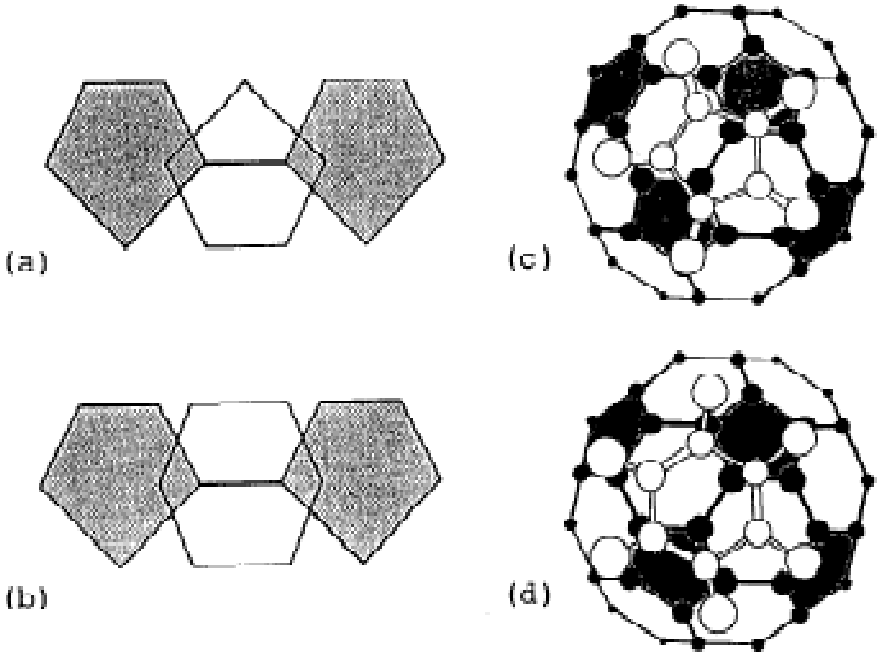

Figure 2.9 Electron-rich double bond on one C_{60} molecule opposite an electron-poor (a) pentagonal face, (b) hexagonal face on the adjacent molecule (51): In view (c), centers nearest-neighbor C_{60} molecules follow arrangement (a). In view(d), rotation of (c) 60° about a threefold axis brings the hexagonal face of one molecule adjacent to the twofold axis of a second molecule [49].

orientation of adjacent molecules is stabilized by aligning an electron-rich double bond on one molecule opposite the electron-poor pentagonal face of an adjacent C_{60} molecule (see Figure 2.9(a)) to achieve a minimum in the orientational potential that governs the alignment. Another structure with only slightly higher energy places the electron rich double bond on one C_{60} molecule opposite an electron-poor hexagonal face (see Figure 2.9(b)). This orientation can be achieved from the lower energy orientation described above by rotation of the C_{60} molecule by 60 around a <111 > axis [70]. As the temperature T is lowered below 260 the probability of occupying the lower energy configuration increases [70]. Evidence for residual structural disorder in the low-temperature molecular alignment is found from neutron scattering experiments [55] and many others [52]. The mechanism by which partial orientational alignment achieved is by the ratcheting motion of the C_{60} molecules around the <111> axes as they execute their hindered rotational motion. The ratcheting motion begins below the 260 K phase transition and continues down to low temperatures.

2.2.4.2 Crystalline C_{70} and Higher Fullerenes

The crystal structure of C_{70} is more complex than that of C_{70} [81-85] At high temperature (T >> 340K), the fcc phase (a = 15.01 Å) of C_{70} with freely rotating molecules is most stable, but because the ideal hexagonal close-packed (hcp) phase with *c/a* = 1.63 is almost equally stable, fcc crystals of C_{70} tend to be severely twinned and show many stacking faults. A transition to another hcp with a = b = 10.11 Å and a larger *c/a* ratio of 1.82 occurs at ~340 K. This larger *c/a* ratio is associated with the orientation of the C_{70} molecules along their long axis, as the free molecular rotation (full rotational symmetry) that is prevalent in the higher temperature phase goes into rotation about the fivefold axis of the C_{70} molecule [82, 85]. As the temperature is lowered further to ~ 280 K, the free rotation about the c-axis also becomes frozen, resulting in a monoclinic structure with the unique axis along the c-axis of the hcp structure. The higher mass fullerenes (C_{76}, C_{84}) have also been shown to crystallize in the fcc structure at room temperature, with an fcc lattice constant that is proportional to n, the number of carbon atoms in the fullerene [86].

2.2.5 Electronic Structure of C_{60}

Fullerenes form molecular solids because of weak intermolecular forces. Thus their electronic structures are expected to be closely related to the electronic levels of the isolated molecules. We know from fullerene structure that each carbon atom in C_{60} has two single bonds along adjacent sides of a pentagon and one double bond between two adjoining hexagons. As all the four valance electrons are occupied fullerenes should be insulators. If these bonds were coplanar, they would be very similar to the sp^2 trigonal bonding in graphite but the curvature of fullerene causes the planner derived trigonal orbitals to hybridize, thereby admixing some sp^3 character to the sp^2 bonding. The shortening of the double bonds and lengthening of the single bonds in the Kekulé arrangement of the C_{60} molecule also strongly influence the electronic structure. To obtain the molecular orbital for C_{60}, the multi-electron problem for the free molecule must first be solved [87]. Representative results for the free C_{60} molecule are shown in figure 2.10 (a) (left panel) [88]. Because of the molecular nature of solid C_{60}, the electronic structure for the solid phase would be expected to be closely related to that of the free molecule [89]. A molecular approach is especially useful for explaining a large body of experimental observations pertinent to the optical properties of C_{60}.

In figure 2.10 (a) (right panel) and in figure 2.10 (b) we see results for fcc solid, based on total energy calculations using norm-conserving pseudopotentials, a local density approximation in density functional theory, and a Gaussian orbital basis set [88]. The various band calculations for C_{60} [90, 88] yield a narrow band (~0.4-0.6 eV bandwidth) solid, a highest occupied molecular orbital-lowest unoccupied molecular orbital (HOMO-LUMO)-derived direct band gap of ~ 1.5 eV at the X point the fcc Brillouin zone. Where the highest occupied state of the C_{60} cluster is the h_u state and it is completely occupied by 10 electrons. The energy gap between the h_u and the lowest unoccupied state, t_{1u} is about 1.9 eV. In the energy levels of the C_{60} cluster, the lowest six optically allowed excitations, $h_u \rightarrow t_{1g}$, $h_g \rightarrow t_{1u}$, $h_u \rightarrow h_g$, $g_g \rightarrow t_{2u}$, $h_g \rightarrow t_{2u}$, and $h_u \rightarrow g_g$, are shown by arrows in figure 2.10 (a).

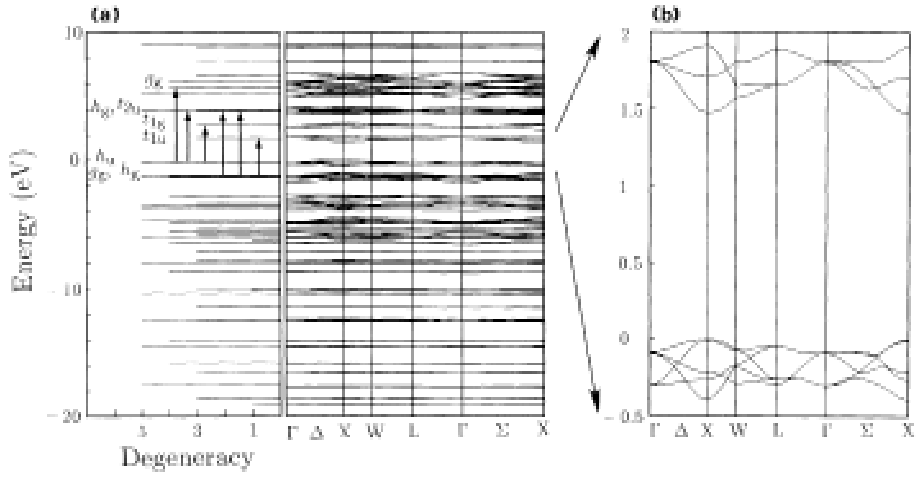

Figure 2.10 (a) Electronic energy levels of the C_{60} cluster (left panel) and the band structure of the fcc C_{60} crystal (right panel).fcc C_{60} is found to be a semiconductor and the valance band top at the X point is defined as the zero energy. The cluster energy levels have been shifted so that the highest occupied state (h_u) is aligned at the mean value of the five highest occupied bands of fcc C_{60} at the Γ point. The optically allowed transitions with excitation energies less than 6 eV are indicated by arrows. (b) Band structure of fcc C_{60} around the energy gap. Both the valance band top and the conduction band bottom are at the X point [49].

According to the molecular approach, many-electron-orbitals for the valence and conduction electron states are constructed for the π-electrons on the C_{60} molecule. The lower-lying σ orbitals are filled and are not generally probed by optical experiments. The number of π-electrons on the C_{60} molecule is 60 (i.e. one state per carbon atom), which is exactly the correct number to fully occupy the h_u (HOMO) level and specifies its symmetry in terms of the icosahedral group I_h. In relating the icosahedral levels to those of full rotational symmetry, we note that 50 π-electrons fully occupy the angular momentum states through l = 4, and the remaining 10 electrons are available to start filling the l = 5 state. In full spherical symmetry, the l = 5 state can accommodate 22 electrons, and the splitting of the l = 5 state in icosahedral symmetryis into the $h_u + t_{1u} + t_{2u}$ irreducible representations. The h_u level is fully occupied and the two threefold t_{1u} and t_{2u} levels are empty.

Doping C_{60} with an alkali-metal transfers electrons to the LUMO levels, which because of their t_{1u} symmetry (figure 2.10) can accommodate three spin-up and three

spin-down electrons. Assuming one electron to be transferred to the C_{60} molecule per alkalimetal atom dopant, the LUMO levels are expected to be half occupied at M_3C_{60} and fully occupied at M_6C_{60}, thereby leading to a filled shell configuration. Thus M_6C_{60} would be expected to be semiconducting, with a band gap between the t_{1u} and t_{2g} levels (see Figure 2.10), whereas M_3C_{60} should be metallic provided that no band gap is introduced at the Fermi level by a Peierls distortion. The large increase in optical absorpitivity in M_xC_{60} with alkali-metal doping is observed as x = 3, and this observation supports the metallic nature of M_3C_{60}. Below ~ 0.5 eV, the free electron contribution to the optical properties is dominant, and above ~ 0.5 eV, interband transitions from the partially occupied t_{1u}, level to the higher lying t_{1g} level take place. It should be emphasized that the level-filling arguments for M_xC_{60} pertain to the free molecule as well as to the levels in the solid state. Because of the high electro-negativity of C_{60}, it is not likely that holes would be created in the h_u-derived C_{60} HOMO level, also in agreement with experiment [56].

Photoemission and inverse photoemission experiments have been especially useful in providing information on the density of states within a few eV of the Fermi level for both undoped and doped fullerenes. Typical photoemission spectra ($E < E_F$, where E_F is the Fermi energy) and inverse photoemission [91] spectra ($E > E_F$) are shown in figure 2.11 [92] for C_{60} and K_xC_{60} ($0 \leq X \leq 6$) [93], where the intensity maxima correspond to peaks in the density of states on the basis of a one-electron picture and a constant matrix element approximation. In the photoemission experiments, the density of states for the occupied levels is probed, whereas in the inverse photoemission experiments, the density of unoccupied states is probed. Photoemission data thus provide evidence for charge transfer and for band filling as x in K_xC_{60} increases. Referring to figure 2.11, we can see the density of states peak associated with the h_u-derived band just above the Fermi level E_F in the C_{60} trace. As K is added to C_{60}, this peak moves closer to E_F as some K_3C_{60} phase is introduced. Upon further addition of K, the t_{1u}-related peak crosses the Fermi level and eventually, for $5.8 \leq x \leq 6.0$, the t_{1u}-derived peak falls below E_F, indicating complete filling of the t_{1u} -derived level; the data for this composition further show a small band gap to the next higher lying t_{1g} -derived level (figure 2.10). Whereas photoemission and inverse photoemission (92) studies show strong similarities between the electronic structure of K_xC_{60} and both Rb_xC_{60} and Cs_xC_{60}, differences

have also been clearly demonstrated between the density of states for K_xC_{60}, and for Na_xC_{60} and Ca_xC_{60}, where in multiple metal ions can be accommodated in the octahedral sites.

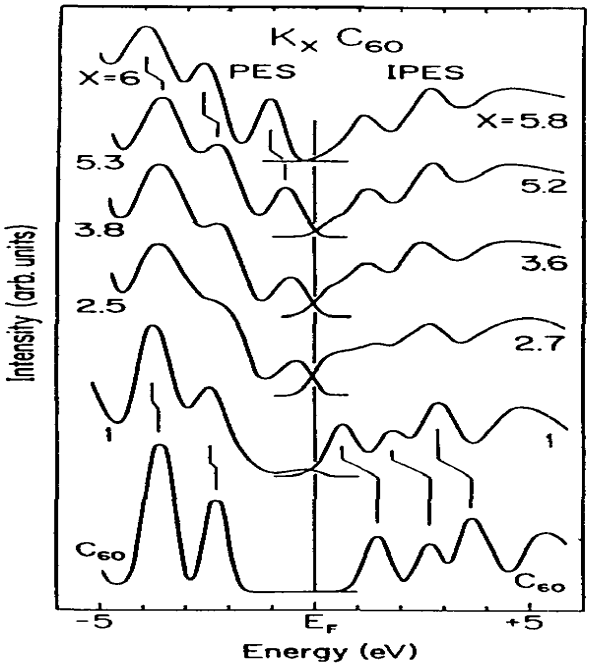

Figure 2.11 Photoemission (PES) and inverse photoemission (IPES) spectra. The spectra show the effects of K incorporation in C_{60} films. The x = 1 spectra show emission at E_F from grains of K_3C_{60}. Adding more K results in an increase of emission below E_F. and a decrease of intensity above E_F. The top spectra show that E_F shifts into the gap when the LUMO bands are filled [92].

2.2.6 Optical Properties of C_{60}

Absorption strengths C_{60} are very low, because the optical transitions near the HOMO-LUMO gap are symmetry-forbidden for electric dipole transitions. Besides, C_{60} is strongly photosensitive, so there is a chance of photo induced chemical reaction even the experiments are done in low light intensities. This causes irreversible structural changes and polymerization [65]. Results for the optical absorbance shown as the Optical density [which is defined as log10(1/transmittance)] vs wavelength in the ultraviolet (UV)- visible range (200-700 nm) for C_{60} and C_{70} in hexane [95] are depicted in figures 2.12(a) and 2.12(b),

respectively. In this figure below ~ 400nm in wavelength or above ~ 2.9 eV in energy optical absorption is strong but at longer wavelengths $490 < \lambda < 640$ nm (or $1.9 < E < 2.5$ eV), weak absorption takes place. The strong absorption indicates electric dipole-allowed transition between occupied (bonding) and empty (antibonding) molecular orbitals (shown in figure 2.10 either the $h_u \rightarrow t_{1g}$ transition or the $h_g \rightarrow t_{1u}$ transition). Where the weak absorption indicates electric dipole-forbidden transitions between the one electron HOMO level with H_u symmetry and

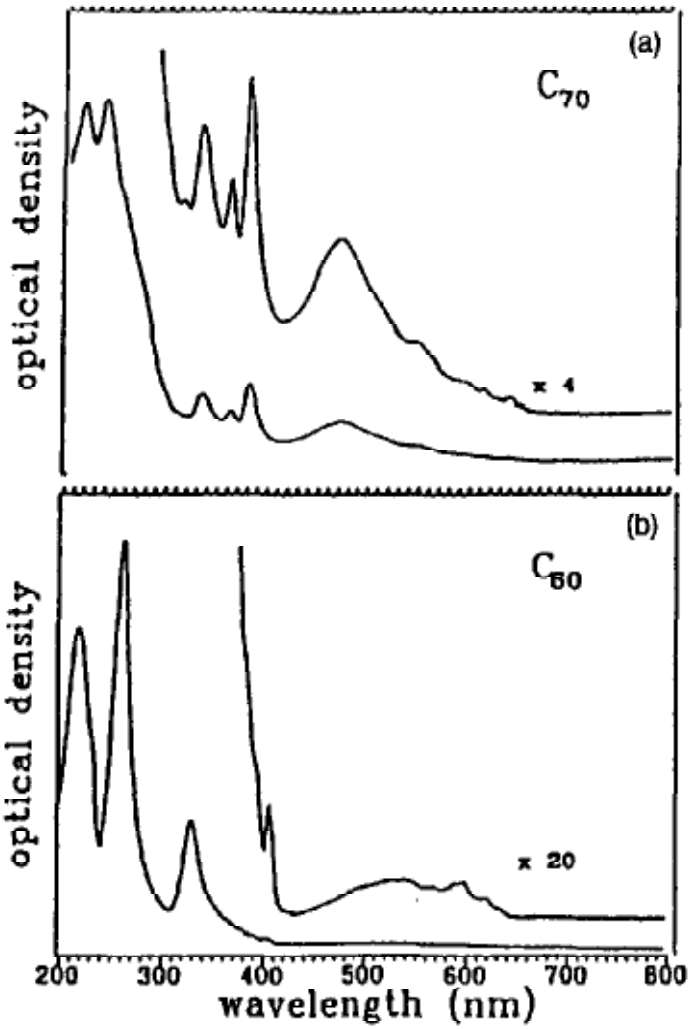

Figure 2.12 Optical density vs wavelength for (a) C_{60} and (b) C_{70} in hexane solutions, with the characteristic absorption bands identified [94].

the one-electron t_{1u} LUMO level (see above, Electronic Structure). Using many-electron molecular states [87], the fully occupied ground HOMO state is identified with singlet S_0 state. In the excited state, we have one electron (t_{1u}) and one hole

(h^9_u) each with spin ½. This interacting electron and hole can either form a singlet S_i state (S = 0), or a triplet T_i state (S= 1). Because the electric dipole matrix element does not depend on spin, there is a strong spin selection rule (ΔS= 0) for optical

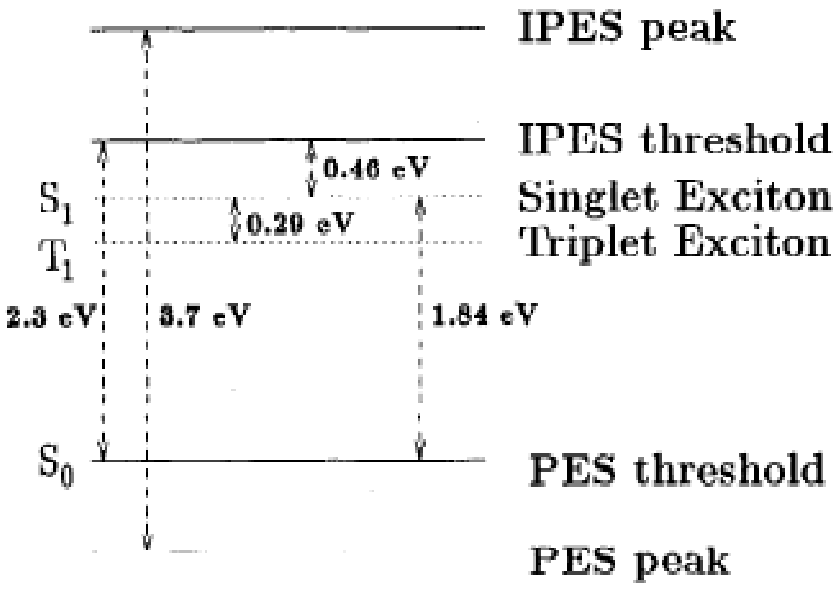

Figure 2.13 Schematic diagram energy levels close to the Fermi level for C_{60} showing the energy separation between the IPES and PES peaks and thresholds, respectively, associated with the HOMO-LUMO gap between the IPES threshold and the PES threshold. This energy differs from the energy between the IPES and PES peaks by the repulsive energy of two holes on the same C_{60} molecule, denoted by U = 1.4 eV. By using a value 1.84 eV for the singlet optical absorption edge, an exciton binding energy of 0.46 eV is obtained. The triplet level at 1.55 eV indicates an exchange energy of 0.29 eV between the singlet and triplet excitons [100].

electric dipole transitions. Because of the very weak spin-orbit interaction for carbon, which has a low atomic number (Z = 6) this strong spin selection rule arises. To satisfy the electric dipole selection rule, appropriate odd-parity vibrational modes must be admixed with the initial and (or) final electronic states for the optical transition. Thus the weak absorption below 2.9 eV involves optical transitions between appropriate vibronic levels. Optical transitions between the HOMO and LUMO levels can thus occur through the excitation, of a vibronic state with the appropriate odd-parity vibrational mode [95-99]. Because of the involvement of vibrational energy in the vibronic state, there is an energy difference between the

lowest energy absorption band [94] and the lowest energy luminescence band. A schematic diagram showing the various energies important to optical phenomena is presented in figure 2.13. The photo-excitation in the long-wavelength portion of the UV-visible spectrum leads to the promotion of C_{60} from the singlet S_0 ground state (^1A_g) into a singlet S_0 excited state, which decays quickly with a nearly 100% efficiency [101, 102] via an inter-system crossing to the lowest excited triplet state T_1.The efficient population of a metastable T_1 (lifetime is much longer) level in C_{60} by optical pumping leads to interesting nonlinear optical properties. One practical application that may follow from this nonlinear property is the development of an optical-limiting material, whose absorptivity increases with increasing light intensity [105, 106]. The emission band of fullerenes generally occurs at lower energies than the absorption band [99]. The optical absorption spectra have their counterparts in the photoluminescence spectra but are shifted by twice the frequency of the vibration involved in the vibronic state. For C_{60}, the occupation of the triplet state T_1 has been shown to be Quenched with nearly 100% efficiency by dioxygen, which leads to a very short lifetime for C_{60} in the excited T_1 state and a fast, nonradiative relaxation to the ground state in the presence of oxygen [102, 104, 107]. However, in the organic glass solvent, the effect of oxygen on the triplet state lifetime is less important because of the lower oxygen diffusion and reduced collision rate. Using photo-acoustic calorimetry [102], the triplet energy E_T = 36 kcal/mol or 1.56 eV has been obtained in C_{60}. A similar value of 1.55 eV has been reported for the triplet energy using electron energy loss spectroscopy (EELS), which is not subject to the same selection rules as the optical dipole transitions. The small singlet-triplet exchange splitting (~0.3 eV; shown in Figure 2.2.10 is consistent with the relatively large diameter of a C_{60} molecule. Using pico- and nanosecond flash photolysis, the excited-state optical properties of C_{60} in toluene have been studied to determine the $S_1 \rightarrow S_n$, [105] and $T_1 \rightarrow T_n$, [103, 104] absorption spectra. For studying the $T_1 \rightarrow T_n$, spectrum, the inter-system crossing (discussed above) is used to populate the T_1 level. The $T_1 \rightarrow T_n$ absorption has been reported to be stronger than $S_0 \rightarrow S_n$, absorption, which provides a mechanism [106] to account for the observed nonlinear absorption leading to optical limiting of transmitted, transient, visible light in both C_{60} and C_{70} (7 ns pulses at 532 nm). No phosphorescent emission from the triplet (T_1) vibronic manifold has been observed in either the solution or solid phase

emission spectra, presumably because of efficient nonradiative relaxation from the metastable T_1 state to the S_0 ground state.

2.2.7 Magnetic Properties of C_{60}

Materials with closed shell configurations are diamagnetic. Thus C_{60} itself is expected to be diamagnetic because by Hund's rule, the ground state for the C_{60} molecule is a nondegenerate J = 0 state, and paramagnetic contributions from permanent moments are not expected [89]. However, the magnitude of the diamagnetic susceptibility is quite low (-0.35×10^{-6} emu/g for C_{60} and -0.59×10^{-6} emu/g for C_{70}) [108, 109] in comparison that for graphite (-21.1×10^{-6} emu/g) [100] because of the approximate cancellation of ring currents in the hexagons (diamagnetic contribution) and in the pentagons (paramagnetic contribution) [108-110]. Under certain doping conditions, fullerene-derived materials that result in a delocalized metallic state should show Pauli paramagnetism. Other dopants with unfilled d- or f-shells are expected to be paramagnetic. Thus the use of endohedral dopants could provide one route for the preparation of magnetic fullerenes.

The most extensively studied magnetic fullerene system is that with the organic donor tetrakisdimethyl-aminoethylene (TDAE) complexed with C_{60} [111], which is interesting as the organic ferromagnet (with only s- and p-orbitals) having the highest Curie temperature of 16.1 K. The compounds TDAE-C_{70}, TDAE-C_{84}, TDAE-C_{90}, and TDAE-C_{94} have been prepared, characterized, and investigated magnetically, but none shows a phase transition to a magnetically ordered state down to 5 K [112].

2.2.8 Applications of C_{60}

Research on solid C_{60} and related materials show many exceptional properties, some of which may lead to practical applications. One promising application for C_{60} is as an optical limiter. Optical limiters are used to protect materials from damage by high-light intensities through a saturation of the transmitted light intensity with increasing incident intensity. Outstanding performance for C_{60} as an optical limiter relative to presently used optical-limiting materials has been observed at 5320 A^0 for 8 ns pulses using solutions of C_{60} in toluene and in chloroform (CH_3Cl). Although C_{70} in similar solutions also showed optical-limiting action, the performance of C_{60} was found to be superior. The proposed mechanism for the optical limiting is that C_{60} and C_{70} are more absorptive for molecules in the triplet-excited state than for the ground state. In this process, the initial absorption of a photon (which takes an electron from the singlet S_0 state to an excited singlet state) is followed by an inter-system crossing from the singlet to a triplet state. Because of the higher excitation cross-section for electrons in the metastable triplet state (relative to the ground state), the population of the metastable triplet state promotes further stronger absorption of photons[108].

Another interesting application is the photoconducting device that can be fabricated using fullerene-doped polymers. Polyvinylcarbazole (PVK) and other selected polymers, such as poly (paraphenylene-vinylene) (PPV) and phenylmethylpolysilane (PMPS), doped with a mixture of C_{60} and C_{70}, has been reported to exhibit exceptionally good photoconductive properties [113-115] that may lead to the development of future polymeric photoconductive materials. Small concentrations of fullerenes (e.g. ~ 3% by weight) lead to charge transfer of the excited electrons in the polymer to the fullerenes, thereby separating the holes and the electrons, preventing rapid recombination, and thereby promoting photoconduction by the mobile holes [116].

Amphiphilic polymers are a class of polymers that self-assemble into different types of microstructure, depending on the solvent environment and external stimuli. Negatively charged fullerene containing polymeric systems can serve as excellent nano-templates for the controlled growth of inorganic crystals at the nano- to micrometer length scale. Most biological systems are basically comprised of many

of these organised structures arranged in an intelligent manner, which impart functions and life to the system. So polymers containing fullerene can be used in the biological system.

The need for biosensors is extensive in our society. Fullerene-based fluorescence quenchers can be synthesized for numerous biosensor applications. To incorporate fullerene in biosensors amine- and carboxy-containing C_{60} is used so that could then be conjugated to biomolecules.

Fullerene can also be used in the MEMS' tunneling tips. To protect the tunneling tip from contact a monolayer of fullerene C_{60} onto the conducting plate surface is deposited. The Fullerene C_{60} molecule is approximately spherical, and a monolayer of fullerene has a thickness of one nanometer, such that a monolayer thereby establishing the theoretical distance desired between the MEMS' tunneling tip and the conducting plate. Exploiting the electrical conductivity of C_{60}, the tip can be accurately positioned by simply monitoring conductivity between the fullerene and the tunneling tip. By monitoring the conductivity between the tip and the fullerene layer as the tip is brought in proximity, the surfaces can be brought together without risk of contacting the underlying conducting surface. Once the tunneling tip is positioned at the one nanometer spacing, with only the monolayer of fullerene between the tunneling tip and the conducting plate, the monolayer of C_{60} can be broken down thermally and removed chemically leaving only the tunneling tip and the conducting plate at the ideal tunneling spacing. Alternatively, the properties of fullerene allow the tunneling process to occur directly across the fullerene monolayer.

Fullerene-doped polymers also have significant potential for use in applications as photodiodes, photovoltaic devices, and as photorefractive materials.

The phthalocyanine–fullerene dyad Pc-C_{60} is an intramolecular donor–acceptor system that can be used as photoactive material in photovoltaic devices. [2-methoxy-5-(30,70-dimethyloctyloxy)-1-4-phenylene vinylene] MDMO-PPV can be used as antenna system in these photovoltaic devices. Photocurrent increases not only in the 500 nm but also below 400-700nm range. The extension of the absorption range can be used for a better matching of the photocurrent spectrum to the solar emission spectrum. In addition, Pc-C_{60} can also be added as a third component to MDMOPPV: PCBM mixtures. Devices made with this ternary mixture showed an

increase of the photocurrent in the range of 700 nm, compared with MDMO-PPV:PCBM devices [117].

Thin films based on donor/acceptor heterojunctions, prepared by means of either consecutive evaporation or co-evaporation, and sandwiched between asymmetric contacts have photovoltaic properties (E,E,E,E)-1,4-bis[(4-styryl)styryl]-2-methoxy-5-(2'-ethylhexoxy)benzene (MEH-OPV5) and Buckminster fullerene C60 are employed as donor and acceptor materials, respectively.

C_{60}/amorphous carbon superlattice structures can be fabricated by shutter-controlled molecular beam deposition The carbon-based superlattice structure is the useful technique to control the band gap energy of carbon materials. The band gap has very important effect in solar cells [118].

With thin films of fullerodendrons (I), (II) and (III) Field-effect transistor (FET) devices can be fabricated by using solution process. The values of field-effect mobility, μ, of the fullerodendron (I) and (II) FETs were determined 4.5×10^{-4} and 1.4×10^{-3} cm^2 V^{-1} s^{-1}, respectively, at 300 K. The n-channel normally-off FET device can be made using fullerodendron (I) and (II) FET with SiO_2/Si substrate. On the other hand, the n-channel normally-on FET using fullerodendron (II) with three types of polymer gate insulators on poly(ehylene terephthalate) substrates can be made [7].

Thin films of C_{60} deposited on *p*-type Si(100) wafer are implanted with low energy phosphorous ions for the photovoltaic applications. The solar cell device is fabricated with phosphorous ion implanted C_{60} films grown on the *p*-type Si wafer. The efficiency of the structure in the multiple energy phosphorous ion implanted C_{60} film/*p*-Si heterojunction is found to be 0.01% under air mass 1.5 conditions [9].

By utilizing the strong bonding of fullerenes to clean silicon surfaces, application of a monolayer of C_{60} as a bonding agent between thin silicon wafers has been indicated [115]. This strong bonding property, together with the low chemical reactivity of fullerenes, has been utilized in the passivation of reactive surfaces by the adsorption of monolayers of C_{60} on aluminum and silicon surfaces [115]. As research on these materials proceeds, it is expected that other interesting physics and chemistry will be discovered (because of the extreme properties exhibited by carbon-based materials generally) and that promising applications will be found for C_{60}-and C_{60}-related materials.

2.3 Raman Spectroscopy

Raman spectroscopy is a spectroscopic technique used in condensed matter physics and chemistry to study vibrational, rotational, and other low-frequency modes in a system [119]. It relies on inelastic scattering, or Raman scattering, of monochromatic light, usually from a laser in the visible, near infrared, or near ultraviolet range. The laser light interacts with phonons or other excitations in the system, resulting in the energy of the laser photons being shifted up or down. The shift in energy gives information about the phonon modes in the system. Infrared spectroscopy yields similar, but complementary, information.

Typically, a sample is illuminated with a laser beam. Light from the illuminated spot is collected with a lens and sent through a monochromator. Wavelengths close to the laser line, due to elastic Rayleigh scattering, are filtered out while the rest of the collected light is dispersed onto a detector.

Spontaneous Raman scattering is typically very weak, and as a result the main difficulty of Raman spectroscopy is separating the weak inelastically scattered light from the intense Rayleigh scattered laser light. Historically, Raman spectrometers used holographic diffraction gratings and multiple dispersion stages to achieve a high degree of laser rejection. In the past, PMTs were the detectors of choice for dispersive Raman setups, which resulted in long acquisition times. However, modern instrumentation almost universally employs notch or edge filters for laser rejection and spectrographs (either Czerny-Turner, echelle or FT based) and CCD detectors.

There are a number of advanced types of Raman spectroscopy, including surface-enhanced Raman, tip-enhanced Raman, polarised Raman, stimulated Raman (analogous to stimulated emission), transmission Raman, spatially-offset Raman, and hyper Raman.

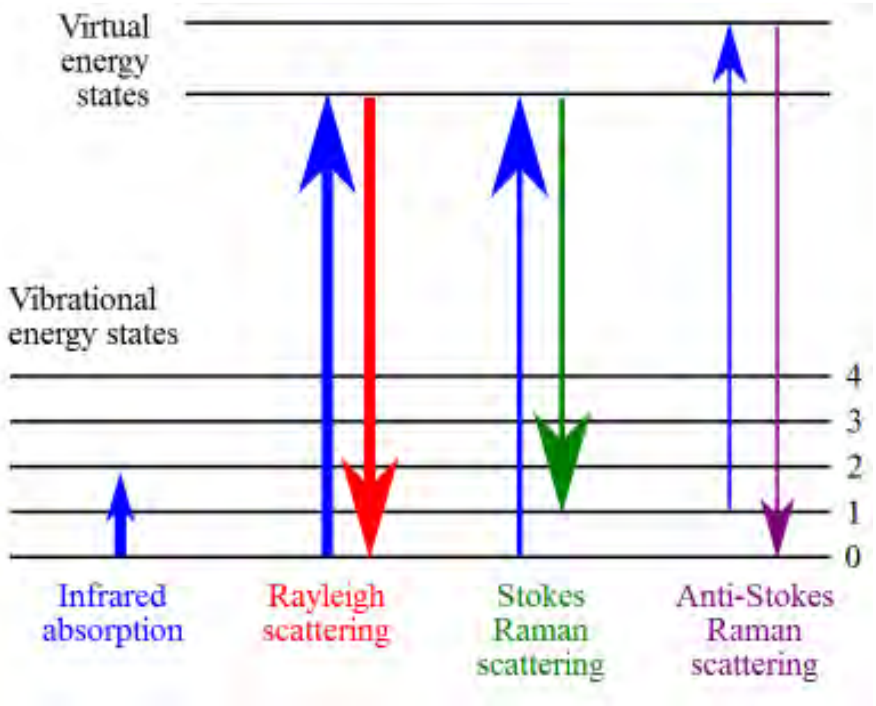

Figure 2.14 Energy level diagram showing the states involved in Raman signal. The line thickness is roughly proportional to signal strength from the different transitions

2.3.1 Principle of Raman Scattering

The Raman effect occurs when light impinges upon a molecule and interacts with the electron cloud of the bonds of that molecule. The incident photon excites one of the phonons into a virtual state. For the spontaneous Raman effect, the molecule will be excited from the ground state to a virtual energy state, and relax into a vibrational excited state, which generates Stokes Raman scattering. If the molecule was already in an elevated vibrational energy state, the Raman scattering is then called anti-Stokes Raman scattering.

A change in the molecular polarization potential or amount of deformation of the electron cloud — with respect to the vibrational coordinate is required for the molecule to exhibit the Raman effect. The amount of the polarizability change will determine the Raman scattering intensity, whereas the Raman shift is equal to the vibrational level that is involved.

2.3.2 History

Although the inelastic scattering of light was predicted by Smekal in 1923, it was not until 1928 that it was observed in practice. The Raman effect was named after one of its discoverers, the Indian scientist Sir C. V. Raman who observed the effect by means of sunlight (1928, together with K. S. Krishnan and independently by Grigory Landsberg and Leonid Mandelstam). Raman won the Nobel Prize in Physics in 1930 for this discovery accomplished using sunlight, a narrow band photographic filter to create monochromatic light and a "crossed" filter to block this monochromatic light. He found that light of changed frequency passed through the "crossed" filter.

Systematic pioneering theory of the Raman effect was developed by Czechoslovak physicist George Placzek between 1930 and 1934 [120]. The mercury arc became the principal light source, first with photographic detection and then with spectrophotometric detection. Currently lasers are used as light sources.

2.3.3 Raman Shift

Raman shift are typically expressed in wavenumbers, which have units of inverse length. In order to convert between spectral wavelength and wavenumbers of shift in the Raman spectrum, the following formula can be used:

$$\Delta\omega = (\frac{1}{\lambda_0} - \frac{1}{\lambda_1})$$

where $\Delta\omega$ is the Raman shift expressed in wavenumber, λ_0 is the excitation wavelength, and λ_1 is the Raman spectrum wavelength. Most commonly, the units chosen for expressing wavenumber in Raman spectra is inverse centimeters (cm^{-1}). Since wavelength is often expressed in units of nanometers (nm), the formula above can scale for this units conversion explicitly, giving

$$\Delta\omega\ (cm^{-1}) = \left(\frac{1}{\lambda_0(nm)} - \frac{1}{\lambda_1(nm)}\right) \times 10^7 \frac{(nm)}{(cm)}$$

2.3.4 Applications of Raman Spectroscopy

Raman spectroscopy is commonly used in chemistry, since vibrational information is specific for the chemical bonds in molecules. It therefore provides a fingerprint by which the molecule can be identified. For instance, the vibrational frequencies of SiO, Si_2O_2, and Si_3O_3 were identified and assigned on the basis of normal coordinate analyses using infrared and Raman spectra [121]. The fingerprint region of organic molecules is in the (wavenumber) range 500-2000 cm^{-1}. Another way that the technique is used is to study changes in chemical bonding, e.g., when a substrate is added to an enzyme. Raman gas analyzers have many practical applications. For instance, they are used in medicine for real-time monitoring of anaesthetic and respiratory gas mixtures during surgery.

In solid state physics, spontaneous Raman spectroscopy is used to, among other things, characterize materials, measure temperature, and find the crystallographic orientation of a sample. As with single molecules, a given solid material has characteristic phonon modes that can help an experimenter identify it. In addition, Raman spectroscopy can be used to observe other low frequency excitations of the solid, such as plasmons, magnons, and superconducting gap excitations. The spontaneous Raman signal gives information on the population of a given phonon mode in the ratio between the Stokes (downshifted) intensity and anti-Stokes (upshifted) intensity.

Raman scattering by an anisotropic crystal gives information on the crystal orientation. The polarization of the Raman scattered light with respect to the crystal and the polarization of the laser light can be used to find the orientation of the crystal, if the crystal structure (specifically, its point group) is known. Raman active fibers, such as aramid and carbon, have vibrational modes that show a shift in Raman frequency with applied stress. Polypropylene fibers also exhibit similar shifts. The radial breathing mode is a commonly used technique to evaluate the diameter of carbon nanotubes. In nanotechnology, a Raman microscope can be used to analyze nanowires to better understand the composition of the structures.

Spatially Offset Raman Spectroscopy (SORS), which is less sensitive to surface layers than conventional Raman, can be used to discover counterfeit drugs without opening

their internal packaging, and for non-invasive monitoring of biological tissue [122]. Raman spectroscopy can be used to investigate the chemical composition of historical documents such as the Book of Kells and contribute to knowledge of the social and economic conditions at the time the documents were produced [123]. Raman spectroscopy offers a non-invasive way to determine the best course of preservation or conservation treatment for such materials. Raman spectroscopy is being investigated as a means to detect explosives for airport security [124].

2.3.5 Variations in Raman Spectroscopy

Several variations of Raman spectroscopy have been developed. The usual purpose is to enhance the sensitivity (e.g., surface-enhanced Raman), to improve the spatial resolution (Raman microscopy), or to acquire very specific information (resonance Raman).

- Surface Enhanced Raman Spectroscopy (SERS) - Normally done in a silver or gold colloid or a substrate containing silver or gold. Surface plasmons of silver and gold are excited by the laser, resulting in an increase in the electric fields surrounding the metal. Given that Raman intensities are proportional to the electric field, there is large increase in the measured signal (by up to 10^{11}). This effect was originally observed by Martin Fleischmann but the prevailing explanation was proposed by Van Duyne in 1977 [125].
- Resonance Raman Spectroscopy - The excitation wavelength is matched to an electronic transition of the molecule or crystal, so that vibrational modes associated with the excited electronic state are greatly enhanced. This is useful for studying large molecules such as polypeptides, which might show hundreds of bands in "conventional" Raman spectra. It is also useful for associating normal modes with their observed frequency shifts [126].
- Surface Enhanced Resonance Raman Spectroscopy (SERRS) - A combination of SERS and resonance Raman spectroscopy which uses proximity to a surface to increase Raman intensity, and excitation wavelength matched to the maximum absorbance of the molecule being analysed.
- Hyper Raman - A non-linear effect in which the vibrational modes interact with the second harmonic of the excitation beam. This requires very high power, but

allows the observation of vibrational modes which are normally "silent". It frequently relies on SERS-type enhancement to boost the sensitivity [127].

- Spontaneous Raman Spectroscopy - Used to study the temperature dependence of the Raman spectra of molecules.
- Optical Tweezers Raman Spectroscopy (OTRS) - Used to study individual particles, and even biochemical processes in single cells trapped by optical tweezers.
- Stimulated Raman Spectroscopy - A two color pulse transfers the population from ground to a rovibrationally excited state, if the difference in energy corresponds to an allowed Raman transition. Two photon UV ionization, applied after the population transfer but before relaxation, allows the intra-molecular or inter-molecular Raman spectrum of a gas or molecular cluster (indeed, a given conformation of molecular cluster) to be collected. This is a useful molecular dynamics technique.
- Spatially Offset Raman Spectroscopy (SORS) - The Raman scatter is collected from regions laterally offset away from the excitation laser spot, leading to significantly lower contributions from the surface layer than with traditional Raman spectroscopy [128].
- Coherent anti-Stokes Raman spectroscopy (CARS) - Two laser beams is used to generate a coherent anti-Stokes frequency beam, which can be enhanced by resonance.
- Raman optical activity (ROA) - Measures vibrational optical activity by means of a small difference in the intensity of Raman scattering from chiral molecules in right- and left-circularly polarized incident light or, equivalently, a small circularly polarized component in the scattered light [129].
- Transmission Raman - Allows probing of a significant bulk of a turbid material, such as powders, capsules, living tissue, etc. It was largely ignored following investigations in the late 1960s [130] but was rediscovered in 2006 as a means of rapid assay of pharmaceutical dosage forms [131]. There are also medical diagnostic applications [132].
- Inverse Raman spectroscopy.

2.4 Raman Spectra of Carbon Films

Raman spectroscopy is a popular, non-destructive tool for structural characterization of carbon films. In this section Raman spectra of graphite, diamond and diamond like carbon (DLC) is reviewed.

2.4.1 Raman spectra of graphite

The first order Raman peak of Graphite shows a sharp, intense peak at 1580 cm^{-1} (G line) and is assigned to the C-C stretching mode within the graphite basal plane with E_{2g} symmetry. The 1354 cm^{-1} disorder peak (D line) results from the first order Raman scattering from a zone edge phonon with A_{1g} symmetry. This normally forbidden Raman mode becomes active as result of relaxation of the wave-vector conservation selection rule, probably as a result of microcrystallinity. The relationship between D and G lines can be related directly to the structure and properties of graphite. The Second order spectrum of polycrystalline graphite exhibits four distinct bands, two overtones at 2(1354) ≈ 2716 cm^{-1} and 2(1580) ≈

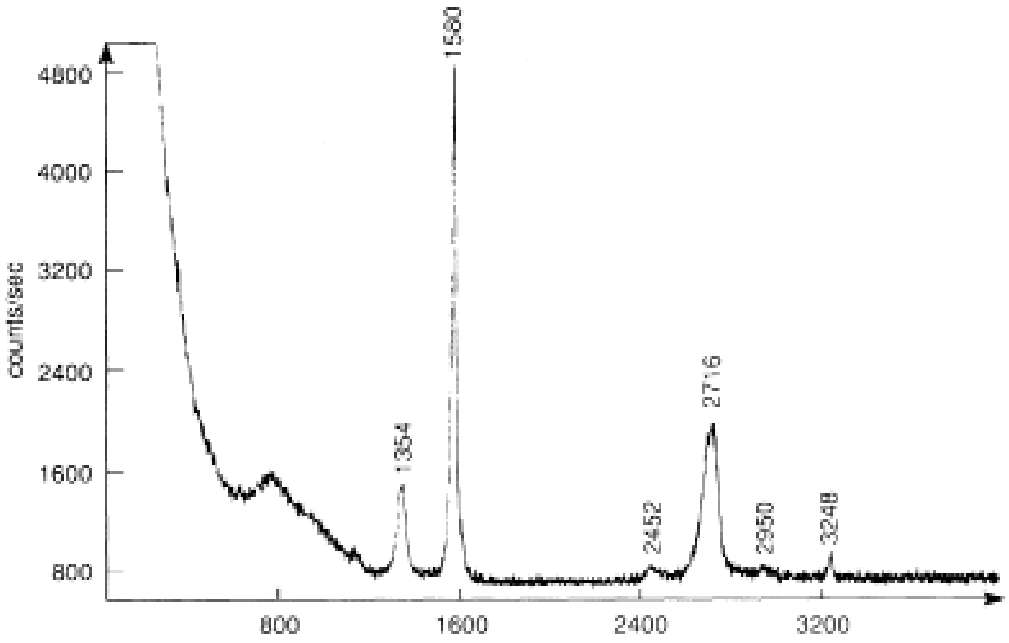

Figure 2.15 Raman Spectra of Polycrystalline Graphite [133].

3248 cm^{-1}, and two combination bands at (1354+1580) ≈ 2950 cm^{-1} and (850+1580) ≈ 2452 cm^{-1}. Figure 2.15 shows the Raman spectra of polycrystalline graphite. Bands at 850 cm^{-1} and 1620 cm^{-1} correspond to peaks in the one-phonon density of states for graphite that are not normally allowed in Raman scattering because of the wave-vector conservation selection rule. However these phonons are allowed in two-phonon Raman scattering.

2.4.2 Raman spectra of diamond

The single triply degenerate first order Raman peak of Diamond appears at 1334 cm^{-1}. For pristine diamond, second order Raman peaks corresponding to overtones and combination bands appears at 2182, 2468 and 2652 cm^{-1}. The second order peaks are weaker more than 2 orders of magnitude than the first order band. Figure 2.16 shows the Raman spectra of diamond.

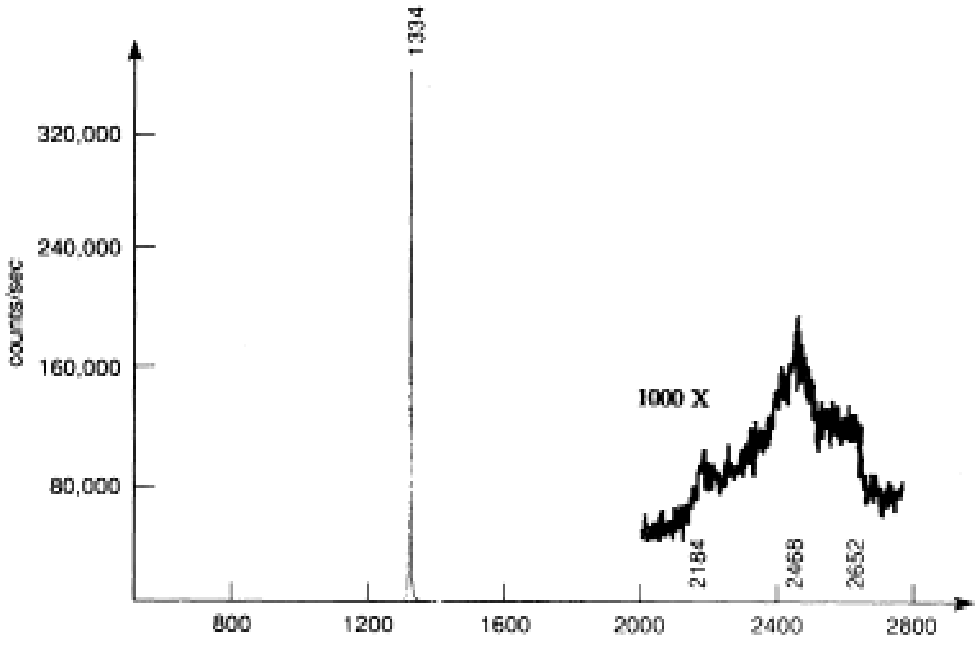

Figure 2.16 Raman Spectra of diamond [133].

2.4.3 Raman spectra of DLC

The Raman spectrum for the DLC film shows a board asymmetric peak near 1526 cm^{-1} as shown in figure 2.17. Band fitting of the asymmetric peak indicates the presence of the D line at 1357 cm^{-1} and the G line at 1533 cm^{-1}. Weak, broad second order peak appears at 300 cm^{-1}.

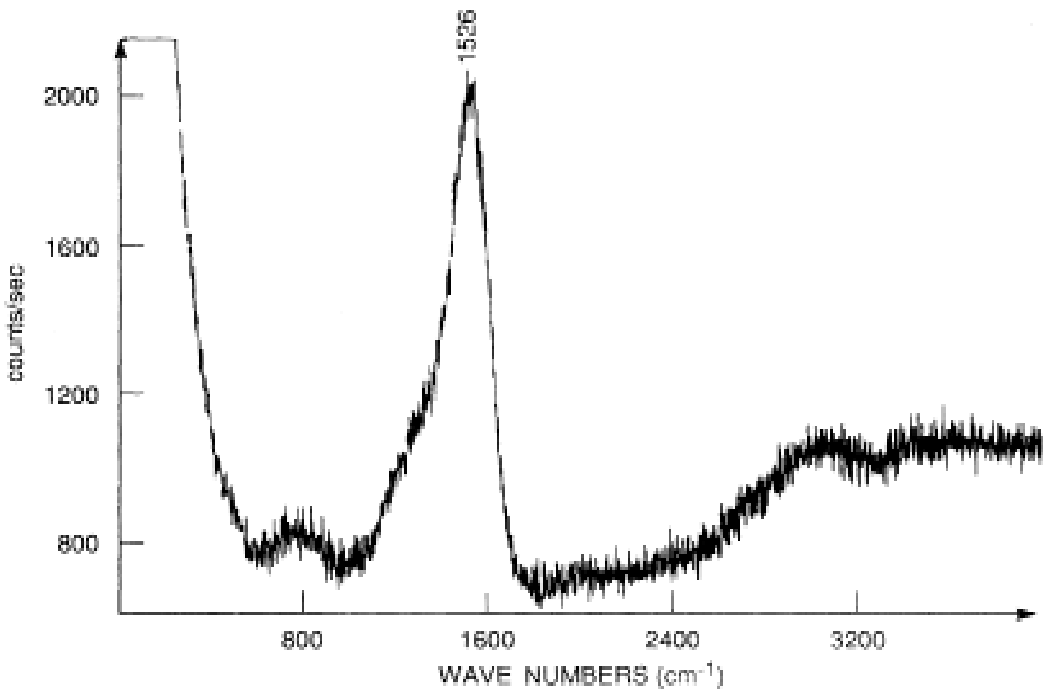

Figure 2.17 Raman spectra of DLC [133].

2.4.4 Raman spectra of nitrogen free carbon

All carbons show common features in their Raman spectra in the 800–2000 cm^{-1} region: the G and D peaks, which lie at 1560 and 1360 cm^{-1}, respectively, for visible excitation, and the T peak at 1060 cm^{-1}, seen only in ultraviolet (UV) excitation. The T peak is due to the C–C sp^3 vibrations (Gilkes *et al*. 1997, 2000; Merkulov *et al.* 1997; Ferrari & Robertson 2001b). The 'molecular' approach is the simplest way to understand the Raman spectra of amorphous carbons, where no extended graphitic

structure exists. It is important to note, nonetheless, that the vibrational and energy levels of clusters can be mapped onto those of graphite. Except for UV excitation, the Raman spectra are dominated by the sp^2 sites, because the excitation resonates with π states. The G and D peaks are due to sp^2 sites. The G peak is due to the bond stretching of all pairs of sp^2 atoms in both rings and chains. The D peak is thus due to the breathing modes of sp^2 atoms in rings. Thus, where there is no rings, there is no D peak.

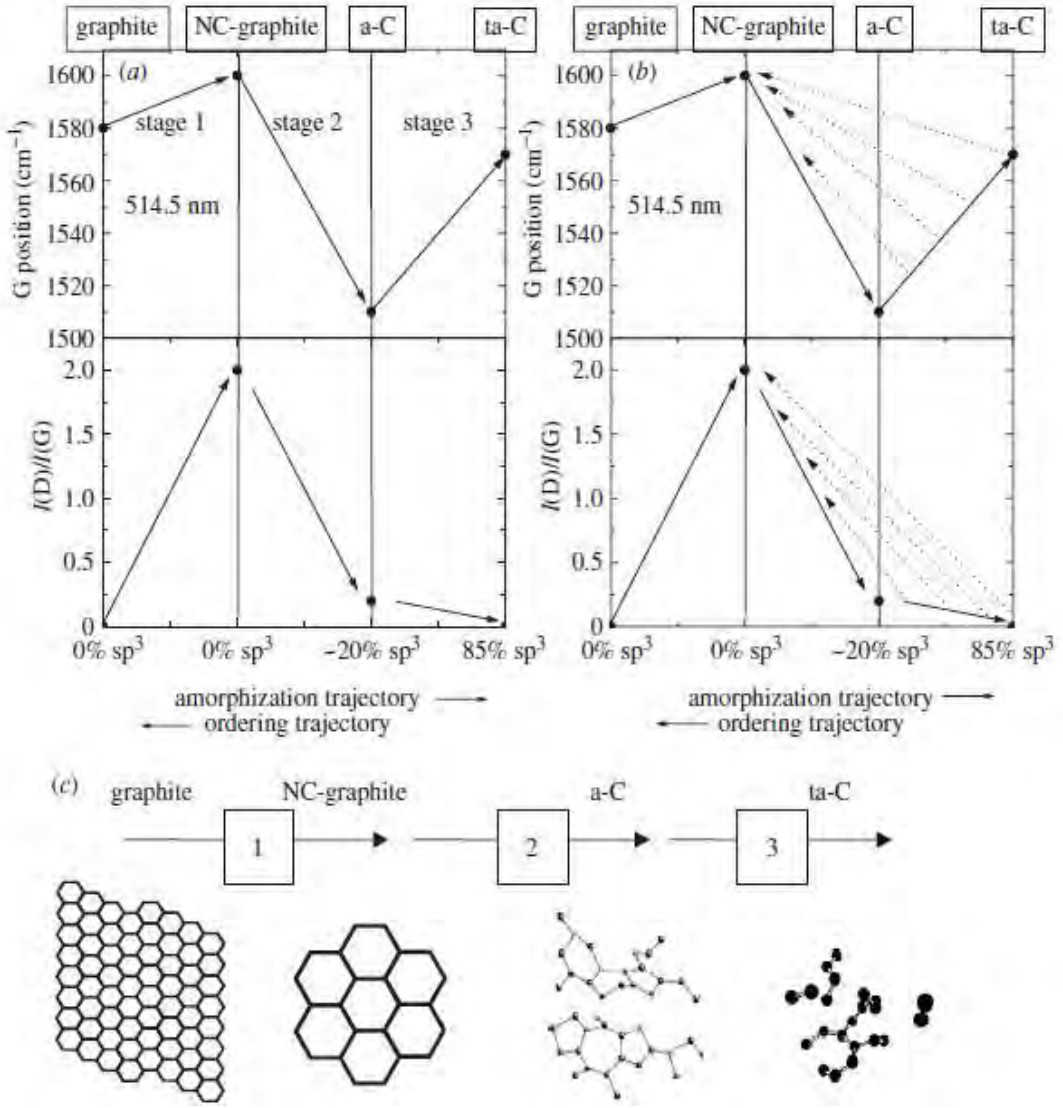

Figure 2.18 Three-stage model of the variation of the Raman G position and the D-to-G intensity ratio, $I(D)/I(G)$, with increasing disorder (Ferrari & Robertson 2000). The dotted left-pointing arrows in (*b*) mark the non-uniqueness region in the ordering trajectory. (*c*) Variation of the sp^2 configuration in the three amorphization stages [134].

The Raman spectra of all carbon films can be described within a three-stage model of increasing disorder (Ferrari & Robertson 2000, 2001*b*), as shown in figure 2.18. As we move from ordered graphite to nanocrystalline graphite, to amorphous carbon and finally to sp^3 bonded ta-C, the sp^2 groups become first smaller, then topologically disordered, and finally change from ring to chain configurations.

We call this the *amorphization trajectory*, consisting of three stages from graphite to ta-C, depicted in figure 2.4.4*c*:
(1) graphite → nanocrystalline graphite (nc-G),
(2) nanocrystalline graphite → sp^2 a-C,
(3) a-C → ta-C.
The Raman spectra depend on
(i) clustering of the sp^2 phase,
(ii) bond-length and bond-angle disorder,
(iii) presence of sp^2 rings or chains,
(iv) the sp^2/sp^3 ratio.

2.4.5 Raman spectra hydrogenated amorphous carbon

The introduction of hydrogen into an amorphous carbon links the amount and configuration of the sp^2 phase with the sp^3 content. In principle, this is quite fortunate, since it implies that for a-C:H, a single wavelength Raman study can be enough to quantify the H and sp^3 content, the optical and mechanical properties. But single wavelength analysis introduces wrong result because some deposition processes can introduce sp^2 clusters even in samples with high H content [91]. In these cases, a multiwavelength Raman spectroscopy is necessary to extract reliable information. Due to the overwhelming cross-section of the sp^2 carbon phase for visible excitation, the C–H stretching modes can only be seen for UV excitation

[68]. However, a typical signature of hydrogenated samples in visible Raman is the increasing photoluminescence background (PL) for increasing H content. This is due to the hydrogen saturation of nonradiative recombination centres [87]. For H content over ~40–45%, this background usually overshadows the Raman signal of a-C:H [68, 86, 88]. Figure 2.19 shows a sample of Raman spectra for hydrogenated amorphous carbon.

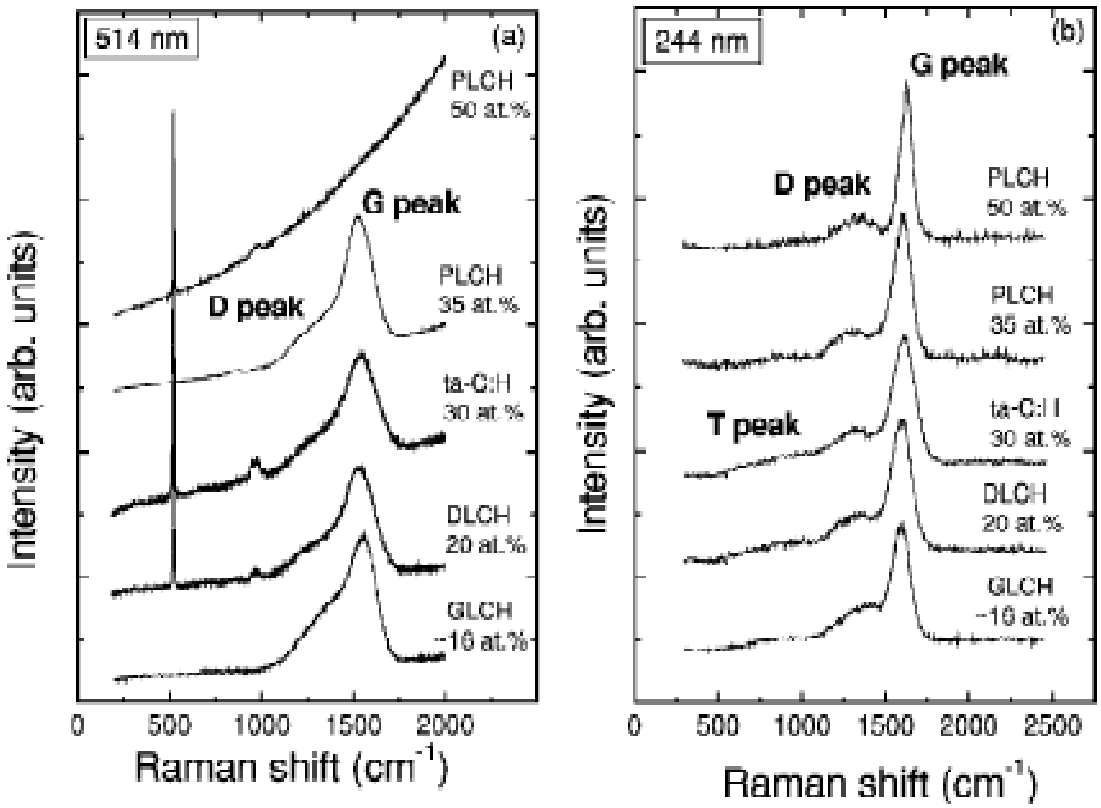

Figure 2.19 Raman spectra of template *a*-C:H films at (a) 514.5 and (b) 244 nm [135].

RAMAN SPECTRA AND OPTICAL ABSORPTION ANALYSES OF CARBONEOUS FILMS DEPOSITED FROM C_{60} IN NITROGEN ENVIRONMENT BY PULSED LASER DEPOSITION

by

Ahmed Zubair

MASTER OF SCIENCE IN ELECTRICAL AND ELECTRONIC ENGINEERING

Department of Electrical Electronic Engineering

BANGLADESH UNIVERSITY OF ENGINEERING AND TECHNOLOGY

October, 2011

2.5 Raman Spectra of C_{60}

2.5.1 Intramolecular mode

C_{60} is highly symmetrical. As we know an atom can have 3 degrees of freedom so for an isolated C_{60} molecule have 60 x 3 = 180 total degrees of freedom, and subtracting the six degrees of freedom corresponding to three translations and three rotations, yields 174 vibrational degrees of freedom. The corresponding 46 distinct intramolecular mode wavenumbers for an isolated C_{60} molecule correspond to the following symmetries:

$$\Gamma_{mol} = 2A_g + 3F_{1g} + 4F_{2g} + 6G_g + 8H_g + A_u + 4F_{1u} + 5F_{2u} + 6G_u + 7H_u \qquad (2.1)$$

where the subscripts *g* (gerade) and *u* (ungerade) refer to the symmetry of the eigenvector under the action of the inversion operator and the symmetry labels (e.g., *F_1, H)* refer to irreducible representations of the icosahedral symmetry group *(I_h).* The degeneracy for each mode symmetry (given in parentheses) also follows from group theory: $A_g(1)$, $A_u(1)$; $F_{1g}(3)$, $F_{2g}(3)$, $F_{1u}(3)$, $F_{2u}(3)$; $G_g(4)$, $G_u(4)$; and $H_g(5)$, $H_u(5)$.Group theory, furthermore, indicates that 10 of the 46 modes are Raman-active *($2A_g$ + $8H_g$)* in first order, four are infrared (IR)-active (*$4F_{1u}$,*) and the remaining 32 are optically silent. Experimental values for all of the 46 distinct modes, determined by first- and second-order Raman [136] and IR [137] spectroscopic features, are displayed in Table 2.2, [137] where the modes are identified with their appropriate symmetries and are listed in order of increasing vibrational wavenumber for each symmetry type.

The $A_g(1)$ 'breathing' mode (492 cm^{-1}) involves identical radial displacements for all 60 carbon atoms, whereas the higher-wavenumber $A_g(2)$ mode, or 'pentagonal pinch' mode (1468 cm^{-1}), involves tangential displacements, with a contraction of the pentagonal rings and an expansion of the hexagonal rings for one set of displacements. It can be seen from table 2.2 eight fivefold degenerate H_g modes span the wave number range from 269 [$H_g(1)$] to 1575 cm^{-1} [$H_g(8)$]. The tendency of the lower frequency molecular modes to have displacements that are more radial in character than those at higher frequencies can be seen in figure 2.20. Because of the degeneracy of each H_g mode, different, equally valid, sets of eigenvectors

corresponding to the same H_g mode frequency can be constructed by forming real orthonormal linear combinations of the five degenerate partners. The experimental Raman spectrum for solid C_{60}, under polarized light is shown in figure 2.22, where the 10 first-order Raman-allowed lines are indicated. For the actual C_{60} molecule, the eigenvalues and eigenvectors for the intramolecular vibrational problem depend on the solutions to the 180 x 180 dynamic matrix.

Table 2.2 Intermolecular vibrational modes of C_{60} molecule and their symmetries experiments and models*

	Even parity (cm^{-1})					Odd parity (cm^{-1})			
ω_i (R)	Expt.[a]	J[b]	Q[c]	F[d]	ω_i (R)	Expt.[a]	J[b]	Q[c]	F[d]
ω_1 (A_g)	497.5	492	478	483	ω_1 (A_u)	1143.0	1142	850	1012
ω_2 (A_g)	1470.0	1468	1499	1470	ω_1 (F_{1u})	526.5	505	547	547
ω_1 (F_{1g})	502.0	501	580	584	ω_2 (F_{1u})	575.8	589	570	578
ω_2 (F_{1g})	975.5	981	788	879	ω_3 (F_{1u})	1182.9	1208	1176	1208
ω_3 (F_{1g})	1357.5	1346	1252	1297	ω_4 (F_{1u})	1429.2	1450	1461	1445
ω_1 (F_{2g})	566.5	541	547	573	ω_1 (F_{2u})	355.5	367	342	377
ω_2 (F_{2g})	865.0	847	610	888	ω_2 (F_{2u})	680	677	738	705
ω_3 (F_{2g})	914.0	931	770	957	ω_3 (F_{2u})	1026.0	1025	962	1014
ω_4 (F_{2g})	1360.0	1351	1316	1433	ω_4 (F_{2u})	1201.0	1212	1185	1274
ω_1 (G_g)	486.0	498	486	449	ω_5 (F_{2u})	1576.5	1575	1639	1564
ω_2 (G_g)	621.0	526	571	612	ω_1 (G_u)	399.5	385	356	346
ω_3 (G_g)	806.0	805	759	840	ω_2 (G_u)	760.0	789	683	829
ω_4 (G_g)	1075.5	1056	1087	1153	ω_3 (G_u)	924.0	929	742	931
ω_5 (G_g)	1356.0	1375	1296	1396	ω_4 (G_u)	970.0	961	957	994
ω_6 (G_g)	1524.5*	1521	1505	1534	ω_5 (G_u)	1310.0	1327	1298	1425
ω_1 (H_g)	273.0	269	258	268	ω_6 (G_u)	1446.0	1413	1440	1451
ω_2 (H_g)	432.5	439	439	438	ω_1 (H_u)	342.5	361	404	387
ω_3 (H_g)	711.0	708	727	692	ω_2 (H_u)	563.0	543	539	521
ω_4 (H_g)	775.0	788	767	782	ω_3 (H_u)	696.0	700	657	667
ω_5 (H_g)	1101.0	1102	1093	1094	ω_4 (H_u)	801.0	801	737	814
ω_6 (H_g)	1251.0	1217	1244	1226	ω_5 (H_u)	1117.0	1129	1205	1141
ω_7 (H_g)	1426.5	1401	1443	1443	ω_6 (H_u)	1385.0	1385	1320	1358
ω_8 (H_g)	1577.5	1575	1575	1568	ω_7 (H_u)	1559.0	1552	1565	1558

[a] All experimental mode wavenumbers in the table are derived from a fit to first-order and higher order Raman and IR spectra. The Raman-active modes have A_g and H_g symmetry and the IR-active modes have *Flu* symmetries. The remaining 32 modes are silent.
[b] Calculated mode wavenumbers of Ref. 148.
[c] Calculated mode wavenumbers of Ref. 149.
[d] Calculated mode wavenumbers of Ref. 150.
* Interpretation of an isotopically induced line in the Raman spectra suggests that this mode should be at 1490 cm^{-1} [151].

Although these vibrational calculations are all made for an isolated molecule, the calculated results are usually are not so different from C_{60} solid phase (in solid phase there is weak van der Waals bonds between C_{60} molecule). The direct experimental

evidence in support of this procedure comes from comparison between the observed vibrational spectra of C_{60} in the gas phase, [138] the solid phase [139,140] and in solution, [140] the mode wavenumbers showing only small differences *(ca.* 5-20 cm^{-1}) from one phase to another. Since the interactions between C_{60} molecules in the solid state are weak, the crystal field resulting from the C_{60} crystal lattice may be treated as a perturbation on the molecular At room temperature, the C_{60}, molecules are rotating rapidly, at a frequency which is low compared with the intramolecular vibrational frequency (10-40 cm^{-1}), therefore, the C_{60} molecules in the solid at room temperature are orientationally disordered. In principle, the effect of the crystal field in the orientationally disordered state of C_{60} would be to make all the vibrational modes in the solid phase weakly Raman and infrared-active, with a contribution to the linewidth arising from the molecular orientational disorder [141,142]. Since the observed room temperature Raman spectra show strong selection rules, we

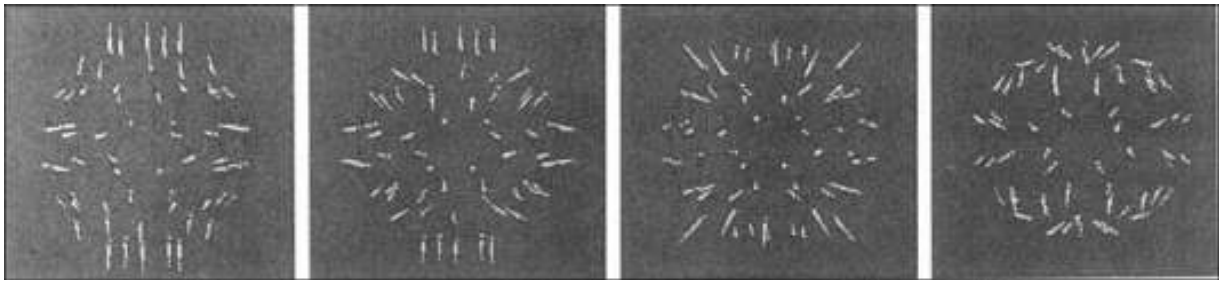

$H_g(1)$ $H_g(2)$ $H_g(3)$ $H_g(4)$

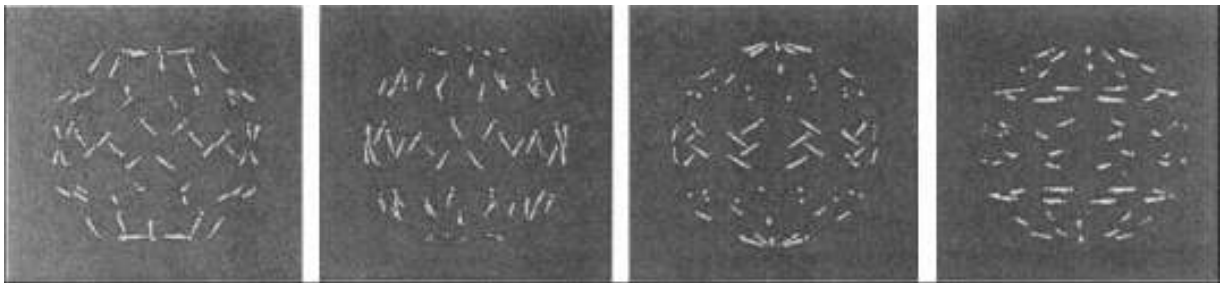

$H_g(5)$ $H_g(6)$ $H_g(7)$ $H_g(8)$

Figure 2.20 Schematic diagram of the normal-mode displacements for representative partners of each of the eight H_g Raman-active modes in C_{60} [152]

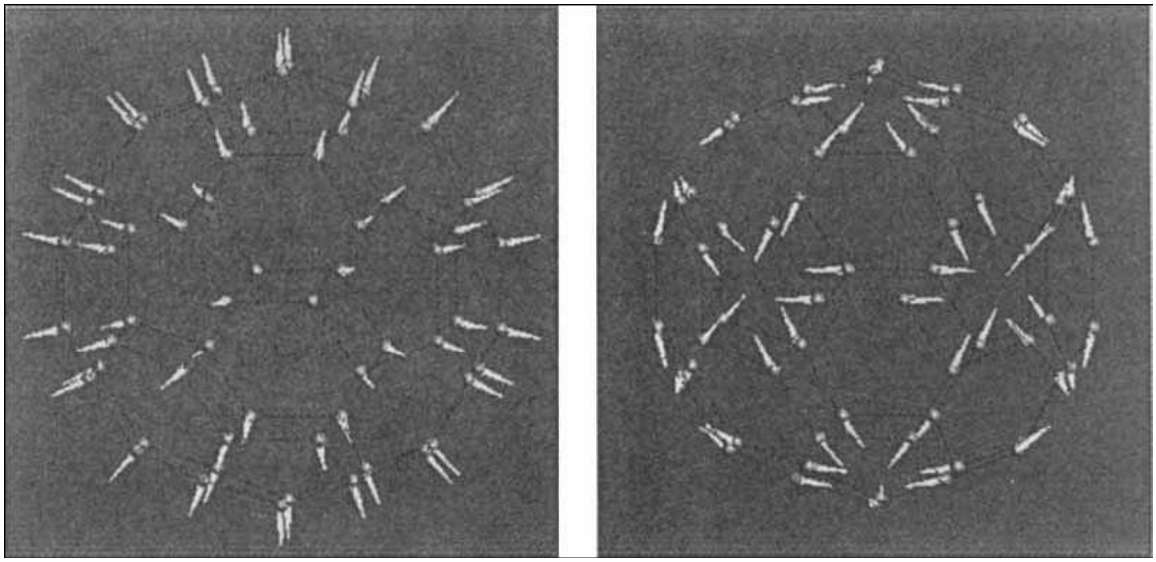

$A_g(1)$ $A_g(2)$

Figure 2.21 Schematic diagram of the displacements corresponding to the displacements for the $A_g(1)$ radial breathing mode are all of equal magnitude and are in the radial direction. (1) The 'pentagonal pinch' mode A_g (2) shows displacements along the fullerene surface [152]

conclude that crystal field effects are weak. Nevertheless they have been observed under higher resolution.

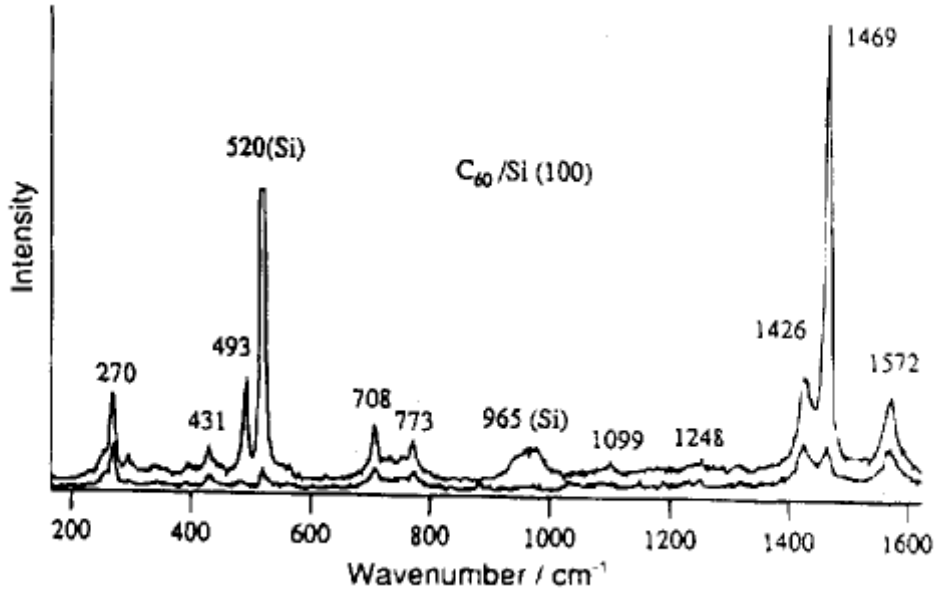

Figure 2.22 Polarized Raman spectra for C_{60}, on a Si (100) substrate. The upper trace is for the (||, ||) polarization and shows both A_g and H_g modes. The lower trace is for the (||, ⊥) polarization and shows only H_g modes [139]

2.5.2 Intermolecular Modes

Because of the molecular nature of solid C_{60} and the large difference in wavenumber between the inter- and intramolecular modes, one expects a decoupling of these two types of vibrational modes. Consistent with this view is the experimental observation of a large wavenumber gap between the lowest wavenumber intramolecular [H_g(l)] mode at 269 cm^{-1} and the highest wavenumber intermolecular or 'phonon' mode at *ca* 60 cm^{-1}. Thus, lattice dynamics models in which molecules are allowed to translate and rotate as rigid units about their equilibrium lattice positions would be expected to be reasonably successful for describing the intermolecular vibrations.

Since the C_{60} molecules rotate rapidly about their equilibrium positions on an fcc lattice above the orientational ordering temperature $T_{01}\approx$ 261 K, [143] an orientational restoring force is ineffective above T_{01} and the rotational intermolecular modes (i.e. librational modes or 'librons') are lost from the phonon spectrum. Above T_{01} solid C_{60} with its rapidly rotating molecules exhibits an fcc lattice which has only one molecule per primitive cell, since all the rotating molecules are viewed as identical. Therefore, only three acoustic branches (T_u symmetry for the cubic group at the Γ-point of the Brillouin zone), involving approximately rigid displacements of the molecules, should be observed. At temperatures well below the orientational ordering temperature $T_{01}\approx$261 K, where, by virtue of their frozen-in orientational order, there are four inequivalent molecules in the simple cubic cell of space group *Pa3* (see figure 2.23), both orientational and translational restoring forces are effective. In this regime, the three rotational and three translational degrees of freedom per molecule lead to 6 *x* 4 = 24 degrees of freedom per primitive unit cell. The symmetries of these 24 modes at the zone center can be obtained by taking the direct product of the molecular site symmetry in the T_6^h space group $(A_g + T_u)$ with those of the rotations (T_g) and translations (T_u).This direct product yields $(A_g + T_u)$ * $(T_u + T_g) = (A_g + E_g + 3T_g) + (A_u + E_u + 3T_u)$ [53] resulting in 10 distinct zone center frequencies, five of which correspond to librations, have even parity and are Raman-active. However, the observation of

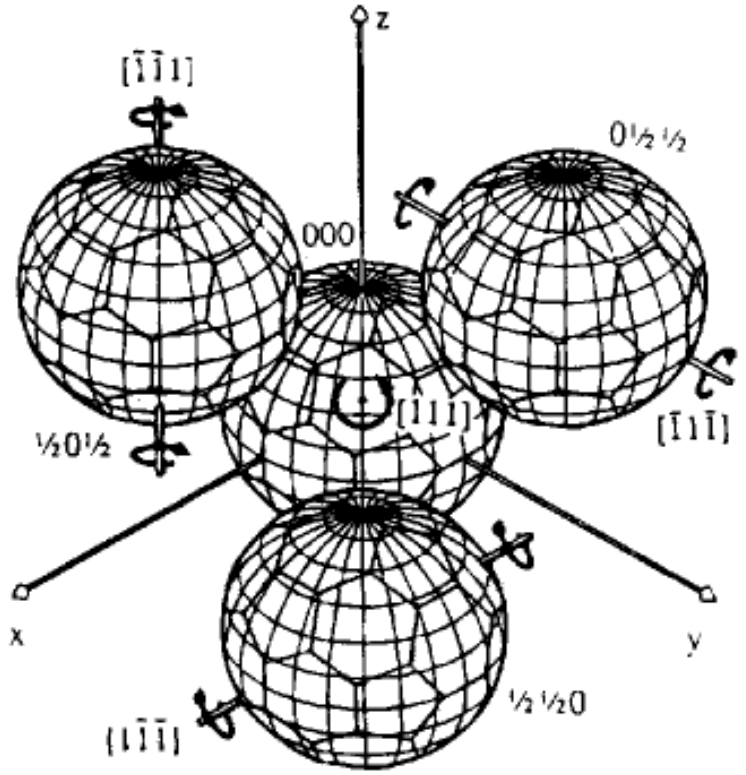

Figure 2.23 The four molecules in the unit cell of C_{60} showing the same standard orientation, with twofold axes aligned parallel to the cube edges. Starting from this orientation, molecules at (0, 0, 0), (½,½,0)**,** (½,0, ½) , and (0, ½,½) are rotated by the same angle about local axes [1,1,1], [l,1,1], [1,1,1] and **[**1,1,1] respectively. The sense of rotation about each [1,1,1] axis is indicated [143].

these modes by Raman spectroscopy is difficult, because of their low wavenumber (< 60 cm^{-1}).The zone center librations *(A_g + E_g + $3T_g$)* are all Raman active, and various Raman studies of the low wavenumber modes have been reported.[144-146] The strongest Raman-active libron has a wavenumber of 17.6 cm^{-1} and upshifts by 0.52 cm^{-1} $kbar^{-1}$, while the next strongest spectral feature is at ca. 20.7 cm^{-1} and upshifts by 0.37 cm^{-1} $kbar^{-1}$, and the corresponding temperature dependent downshifts (below T_{01}*)* are, respectively, -0.0187 and -0.0131 cm^{-1} K^{-1} [142]. A theoretical model for the pressure and temperature dependence of T_{01} shows that the increase in libron amplitude is more important than lattice thermal expansion for inducing pressure and temperature dependence of the mode frequencies [142]. This view is also borne out by theoretical calculation [147].

2.6 Curve Fitting Technique for Raman Spectra Analysis

2.6.1 Noise Elimination

The Raman Spectra contains noise. So noise elimination is needed for the experimental data. We have used the moving average method for getting a smooth curve.
The main purpose of this step is the elimination of small systematic variation in intensity, of instrumental origin.

2.6.2 Background Subtraction

The second step for the analysis of the spectra is background subtraction. The objective of background subtraction is to remove a constant offset from the signal.

There are three backgrounds that are generally used. They are linear, Shirley and Tougaard Background. Of these backgrounds Shirley is most used one. It takes into account both the intrinsic (secondary process) and extrinsic losses (losses in the sample). We have used Shirley background in our work.

2.6.3 Line Shapes Used

Certain line shapes are used for the peaks which are used for curve fitting of the spectrum. The most widely used shape is a combination of Gaussian and lorentzian shapes.

2.6.4 Curve Fitting Technique

To analysis the Raman spectra should be deconvoluted. The Raman spectra are fitted by using the software developed by us. In the fitting routine, intensity, half-width and position of all bands are treated simultaneously as unconstrained

variables. The number of lines in the fitted to a spectrum is also treated statistically by numerical minimization of the squares of the deviations between the observed and the calculated Raman envelopes and by maximizing the randomness of the residuals.

The curve fitting technique, used in our work, is described in details in the section. At first the spectra is smoothed for the elimination of small systematic variation. Signal smoothing is done by using moving average (MA) technique.

Simple working principle of MA system can be expressed as

$$y(n) = \sum_{k=0}^{M} b_k \, x(n-k) \tag{2.2}$$

where y(n) =smoothed data at n

x(n) = Raw data at n

M = order of MA

Then the background is subtracted to get rid of constant offset in the data. At first a constant background is subtracted from the data. The constant background is the minimum value of the Raman data.

$$y1(n) = y(n) - yb \tag{2.3}$$

where y1(n) =data after constant background subtraction at n

yb = minimum (Y)

Y = Data vector

After that Shirley background subtraction method is used.

The Shirley background subtraction principle can be expressed as

$$ys(n) = y1(n) - ys(0) \left[\sum_{n'>n} y1(n') / \sum_{n'>0} y1(n') \right] \tag{2.4}$$

where ys(n) =data after Shirley background subtraction at n

ys(0) is set as zero i.e. ys(0) =0

The curve is then fitted with characteristics peak by using the minimization technique of Powell and Fletcher (1963) [153]. This technique is described in the appendix I.

In our work mean square error is minimized for the fitted curve. The lineshapes used are combination of Gaussian and Lorentzian curves.

So, the equation of the fitted curve will be

$$yf = \sum_{i=1}^{n}\{gp\ fg + (1 - gp)fl\} \tag{2.5}$$

where gp= percentage of Gaussian curve

fg = Gaussian function

fl = lorentzian function

n = Number of Peaks

Gaussian function, $fg = x1\ e^{-\frac{1}{2}\left(\frac{xd-x2}{x3}\right)^2}$ (2.6)

where x1= Amplitude

x2= Peak position

x3= Width

Lorentzian function, $fl = \frac{x1}{1+\left(\frac{xd-x2}{x3}\right)^2}$ (2.7)

where x1= Amplitude

x2= Peak position

x3= Width

So, the equation of the fitted curve becomes

$$yf = \sum_{i=1}^{n}\left\{ gpi\ x1i\ e^{-\frac{1}{2}\left(\frac{xd-x2i}{x3i}\right)^2} + (1 - gpi)\frac{x1i}{1+\left(\frac{xd-x2i}{x3i}\right)^2}\right\} \tag{2.8}$$

The function that must be minimized becomes

$$f = \left[y - \sum_{i=1}^{n}\left\{ gpi\ x1i\ e^{-\frac{1}{2}\left(\frac{xd-x2i}{x3i}\right)^2} + (1 - gpi)\frac{x1i}{1+\left(\frac{xd-x2i}{x3i}\right)^2}\right\}\right]^2 \tag{2.9}$$

Here, Variable are x1i, x2i, x3i and gpi where i=1,2,...n

The basic algorithm of fitting can be described as below:

1. **Choose a step direction s** by acting on the current gradient **g** with the current metric in gradient space. If in this metric, **g** has a sufficiently small magnitude, then go to step 5.
2. **Estimate the location** of an optimum in the direction **s**; e.g., by making a cubic interpolation. Go to this location if a sufficient change in the objective function is expected, else choose a new direction.
3. **Evaluate the objective function f and and its gradient f** at the location **x** chosen in step 2 and estimate the directional derivative of **f** at **x**.
4. **Update the metric** in gradient space, so that it yields **s** when acting on the directional derivative estimated in step 3. Return to step 1.
5. **Test the current metric and minimizer**. If these seem adequate, then quit, else return to step 1.

The gradient of the function with respect to the variable can be expressed as below:

Gradient with respect to gp

$$\frac{\partial f}{\partial gpi} = 2\{-\,x1i\; e^{-\frac{1}{2}\left(\frac{xd-x2i}{x3i}\right)^2} + \frac{x1i}{1+\left(\frac{xd-x2i}{x3i}\right)^2}\}\left[y - \sum_{i=1}^{n}\left\{ gpi\; x1i\; e^{-\frac{1}{2}\left(\frac{xd-x2i}{x3i}\right)^2} + (1 - gpi)\frac{x1i}{1+\left(\frac{xd-x2i}{x3i}\right)^2}\right\}\right] \quad (2.10)$$

Gradient with respect to amplitude of the peaks

$$\frac{\partial f}{\partial x1i} = \quad A\left[y - \sum_{i=1}^{n}\left\{ gpi\, x1i\; e^{-\frac{1}{2}\left(\frac{xd-x2i}{x3i}\right)^2} + (1 - gpi)\frac{x1i}{1+\left(\frac{xd-x2i}{x3i}\right)^2}\right\}\right] \quad (2.11)$$

where, $A = 2\left\{ gpi\; e^{-\frac{1}{2}\left(\frac{xd-x2i}{x3i}\right)^2} + (1 - gpi)\frac{1}{1+\left(\frac{xd-x2i}{x3i}\right)^2}\right\}$

Gradient with respect to position of the peaks

$$\frac{\partial f}{\partial x2i} =$$
$$2\left\{ gpi\; x1i\, e^{-\frac{1}{2}\left(\frac{xd-x2i}{x3i}\right)^2}\left(\frac{xd-x2i}{x3i}\right)\left(\frac{1}{x3i}\right) + \right.$$
$$\left. 2(1 - gpi)\frac{x1i}{\left\{1+\left(\frac{xd-x2i}{x3i}\right)^2\right\}^2}\left(\frac{xd-x2i}{x3i}\right)\left(\frac{1}{x3i}\right)\right\}\left[y - \sum_{i=1}^{n}\left\{ gpi\, x1i\; e^{-\frac{1}{2}\left(\frac{xd-x2i}{x3i}\right)^2} + \right.\right.$$
$$\left.\left.(1 - gpi)\frac{x1i}{1+\left(\frac{xd-x2i}{x3i}\right)^2}\right\}\right] \quad (2.12)$$

Gradient with respect to width of the peaks

$$\frac{\partial f}{\partial x3i} =$$
$$2\left\{ gpi\; x1i\, e^{-\frac{1}{2}\left(\frac{xd-x2i}{x3i}\right)^2}\left(\frac{xd-x2i}{x3i}\right)\left(\frac{xd-x2i}{x3i^2}\right) + \right.$$
$$\left. 2(1 - gpi)\frac{x1i}{\left\{1+\left(\frac{xd-x2i}{x3i}\right)^2\right\}^2}\left(\frac{xd-x2i}{x3i}\right)\left(\frac{xd-x2i}{x3i^2}\right)\right\}\left[y - \sum_{i=1}^{n}\left\{ gpi\, x1i\; e^{-\frac{1}{2}\left(\frac{xd-x2i}{x3i}\right)^2} + \right.\right.$$
$$\left.\left.(1 - gpi)\frac{x1i}{1+\left(\frac{xd-x2i}{x3i}\right)^2}\right\}\right] \quad (2.13)$$

Geometrical Interpretation

Geometric concept is convenient to describe the minimization procedure. In the figure 2.24 we can see a two dimensional space x where the minimum is at the point C. The surfaces shown are equal valued curve i.e. A and B are equal. If we map the function in the gradient space g of the function, then the minimum C will be at the point where the both gradient is zero. In the same way, we have N number of variables then using the gradient of function with respect to the variables we can find the minimum of the function.

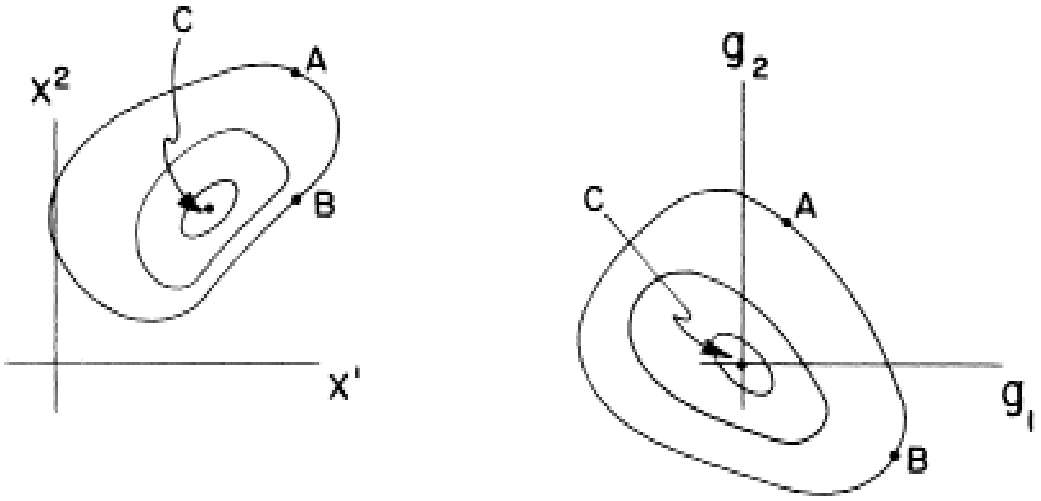

Figure 2.24 Geometric interpretation of x (variable) and g (gradient).

2.7 Theory of Optical Absorption Behavior

2.7.1 Determination of energy band gap

An optical measurement constitutes the most important means of determining the band structures of semiconductors. Photon-induced electronic transitions can occur between different bands, which lead to the determination of the energy bandgap, or within a single band such as the free-carrier absorption. Optical measurements can also be used to study lattice-vibrations.

The optical transmission coefficient or transmittance T and the optical reflection coefficient or reflectance R are the two important quantities generally measured. For normal incidence they are given by

$$\mathrm{T} = \frac{(1-\mathrm{R}^2)\mathrm{e}^{-4\pi\mathrm{d}/\lambda}}{1-\mathrm{R}^2\mathrm{e}^{-8\pi\mathrm{d}/\lambda}} \tag{2.14}$$

$$R = \frac{(1-n)^2+k^2}{(1+n)^2+k^2} \tag{2.15}$$

where λ is the wavelength, n is the refractive index, k is the absorption constant and d is the thickness of the sample. The absorption coefficient per unit length α is given by

$$\alpha = \frac{4\pi k}{\lambda} \tag{2.16}$$

The optical absorption coefficient (α) is calculated from the measurements of optical reflectance and transmittance data using the relation [154]

$$T = (1-R)^2 e^{-\alpha d} \tag{2.17}$$

Near absorption edge the absorption coefficient can be expressed as

$$\alpha h\nu \sim (h\nu - E_g)^{\gamma} \tag{2.18}$$

Where, hν is the photon energy, E_g is the band gap, B is the Tauc parameter and γ is the constant.

In one electron approximation γ equals $\frac{1}{2}$ and $\frac{3}{2}$ for allowed direct transitions and forbidden direct transition, respectively and γ equals 2 for indirect transitions where phonons are involved. In addition, γ equals $\frac{1}{2}$ for allowed indirect transitions to exciton states, where exciton is a bound electron-hole pair with energy levels in the bandgap and moves through the crystals lattice as a unit [155].

Near absorption edge, where the values (hν-E_g) become comparable with the binding energy of the exciton, the coulomb interaction between the free hole and electron must be taken into account. For $h\nu \lesssim E_g$, the absorption merges continuously into the absorption caused by the higher states of the exciton. When $h\nu \gg E_g$, higher energy bands participate in the transition processes, and complicated band structures are reflected in the absorption coefficient.

Carbon films generally are indirect materials. So to calculate the band gap, the value for γ is assumed as 2. So the equation 2.18 becomes

$$(\alpha h\nu)^{1/2} = B(h\nu - E_g) \tag{2.19}$$

$(\alpha h\nu)^{1/2}$ is plotted as a function of photon energy, $h\nu$. The optical gap is then obtained from the extrapolation of the linear part of the curve, $(\alpha h\nu)^{1/2}$ vs $h\nu$ at the absorption coefficient α = 0, using the equation 2.19.

Although in the procedure described above, it is assumed that there are no energy states in the forbidden band, it is not the actual case. In the amorphous material there

is several energy states created in the forbidden band. The electronic states can be divided into three types: extended, band tails (Urbach region) and deep states. Each of these originates from a different physical process: extended states from long range correlation and symmetry, tail states from structural disorder, and deep states by structural defects [156]. In the next section inter band transition is discussed elaborately.

The Tauc parameter, B, is a measure of the steepness of the band tail density of states. The Tauc parameter, B, can be obtained from slope of the straight line fitted for the linear part of the curve $(\alpha h\nu)^{1/2}$ vs $h\nu$.

2.7.2 Optical transitions in amorphous materials

The following sketch of the density of electronic states shows the types of optical transitions that are going to be discussed below:

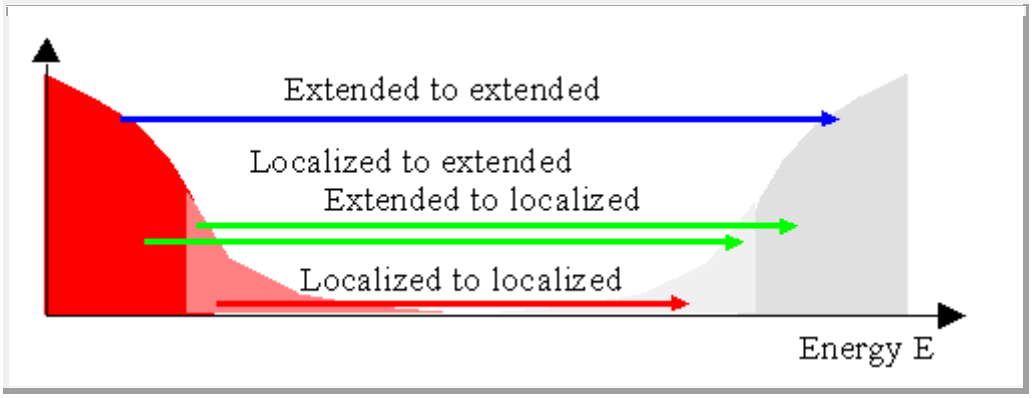

Figure 2.25 Optical transitions in different states

2.7.2.1 Extended to extended states transition

The transitions from extended to extended states are very similar to the ones known from crystalline materials. As can be seen from the sketch they determine the absorption of light at high energies (above the gap energy) or short wavelength. In the case of parabolic bands (without tail states) the shape of the density of states is the following:

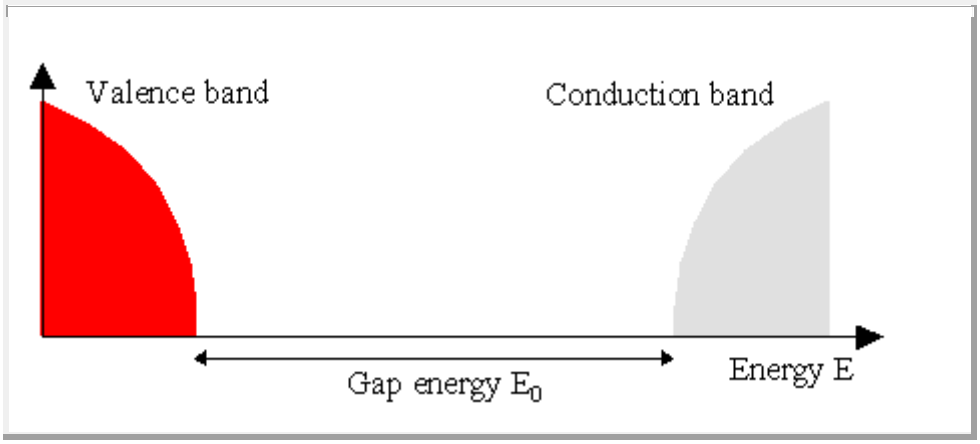

Figure 2.26 Extended to extended states transitions

This leads to an absorption coefficient of the form

$$\alpha(h\nu) \sim \frac{1}{2\pi\nu}(h\nu - E_g)^2$$

Hence a plot of

$$\sqrt{h\nu\alpha(h\nu)} \sim h\nu - E_g$$

versus energy should lead to a straight line whose intersection with the y-axis gives the gap energy E_g, the so-called 'Tauc gap'. The Tauc gap is quite often used to characterize the optical properties of amorphous materials. From the considerations given above it is clear that the Tauc gap gives information on the energy separation of the extended states of valence and conduction bands.

2.7.2.2 Extended to localized and localized to extended states transitions

Below the gap where in ideal crystalline materials no absorption is observed in amorphous materials transitions from occupied extended states of the valence band to empty tail states of the conduction band may occur. In a similar way transitions from occupied valence band tail states to the empty extended states of the conduction band are possible. Both types of transitions should have similar matrix elements.

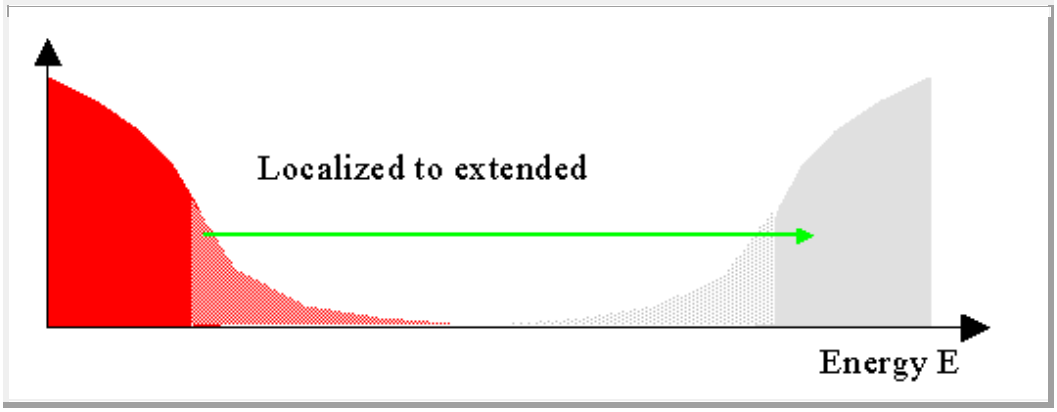

Figure 2.27 Localized to extended states transitions

For the transitions from localized to extended states (and for extended to localized ones) with an exponential decay of the density of states of the localized states into the gap one finds an exponential relation between absorption coefficient and frequency:

$$\alpha(h\nu) \sim \exp\left(\frac{h\nu}{E_U}\right)$$

where, E_U is called 'Urbach energy'. Since

$$\ln \alpha\,(h\nu) = C + \frac{h\nu}{E_U}$$

$$E_U = \frac{1}{\frac{d}{dh\nu}(\ln \alpha(h\nu))}$$

One can determine the Urbach energy by plotting the logarithm of the absorption coefficient and taking the inverse of the slope of the linear part of the graph.

2.7.2.3 Localized to localized states transitions

These transitions usually are not very important since the number of states involved is low and the transition matrix elements are significantly smaller compared to those of the transitions mentioned above. This is due to the fact that the matrix elements are integrals over all space over the product of two functions (the initial and the derivative of the final state) which are separated in space and hence do exhibit almost no overlap. Transitions from localized to localized states would lead to absorption in the low energy regions of the spectrum which in most cases is the near to mid infrared region.

2.8 Review of Current Density versus Voltage Characteristics of p-n Heterojunction

The heterojunction properties depend on both the propertied of the materials constructing the junction. The current versus voltage characteristics in the heterojunction depends on the band discontinuities in the junction. If the barrier to holes is much higher than that of electrons, then the current consists almost all electrons. Both the forward current and reverse current strongly depend on the behaviors of the junction constructing materials. The expression for total current density in the junction is given by [155],

$$J = J_0(e^{\frac{qV}{\eta kT}} - 1) \tag{2.20}$$

and thus

$$\ln J = ln\, J_0 + \, qV/\eta kT \tag{2.21}$$

where,

J is the total junction current density

J_0 is the reverse saturation current density in the junction

q is the charge of electron

V is the applied voltage to the junction

η is the diode quality factor

k is the Boltzmann's constant

T is the temperature given in K

The reverse saturation current density is given by

$$J_0 = q\left(\frac{D_p}{L_p}\frac{{n_{iN}}^2}{N_D} + \frac{D_n}{L_n}\frac{{n_{iP}}^2}{N_A}\right) \tag{2.22}$$

where, q is the charge of electron

A is the cross section area of the junction

D_p is the hole diffusivity in the n-type material

D_n is the electron diffusivity in the p-type material

L_p is the hole diffusion length in the n-type material

L_n is the hole diffusion length in the p-type material

n_{iN} is the intrinsic carrier concentration in the n-type material

n_{iP} is the intrinsic carrier concentration in the p-type material

N_D is the donor concentration

N_A is the acceptor concentration

The diode quality factor η actually indicates how ideally the junction behaves. The value of η for an ideal diode is 1. When the value of the diode quality factor is 2, it indicates that recombination limited current flows through the junction. The value of quality factor in between 1 and 2 indicates that the current flowing in the junction comprises both diffusion limited and recombination limited current. As shown in equation 2.21 from the slope of ln(J) vs V characteristics, the diode quality factor η for our heterojunction can be calculated.

Thus knowing the value of reverse saturation current, it is possible to calculate some of the parameters for the heterojunction using equation 2.22.

Figure 2.28 shows current-voltage characteristics of a practical Si diode. J_0 represents the saturation current density in the junction. In the figure region (a) represents generation-recombination current. Because of the reduction in carrier concentration under the reverse bias, the dominant recombination-generation process is due to emission. The generation current is given by [155]

$$J_{gen} = \frac{qn_iW}{\tau_e} \tag{2.23}$$

where, q is the charge of electron, n_i is the intrinsic carrier concentration, W is the total depletion width and τ_e is the effective carrier life time.

At a given temperature, generation current is proportional to the depletion-layer width, which is dependent on the applied reverse bias voltage. If the effective life time is a slowly varying function of temperature, the generation current will then have same temperature dependence as n_i. For semiconductors with large values of n_i the diffusion component will dominate at room temperature, but if n_i is small the generation current will dominate. At forward bias, the major recombination-generation processes in the depletion region are the capture processes, there exists a recombination current in addition to the different current. The recombination current is given by [155],

$$J_{rec} \sim n_i N_t \tag{2.24}$$

where, N_t is the trap density.

Similar to generation current in the reverse bias, the recombination current in the forward bias is also proportional to n_i.

In the figure 2.28 region (b) represents diffusion current in the bulk of semiconductor.

Region (c) indicates high injection current. At high current densities under the forward bias condition such that the injected minority carrier density is comparable with the majority concentration, both drift and diffusion current components must be considered.

At region (d) series resistance effect is introduced to current voltage characteristics of the diode.

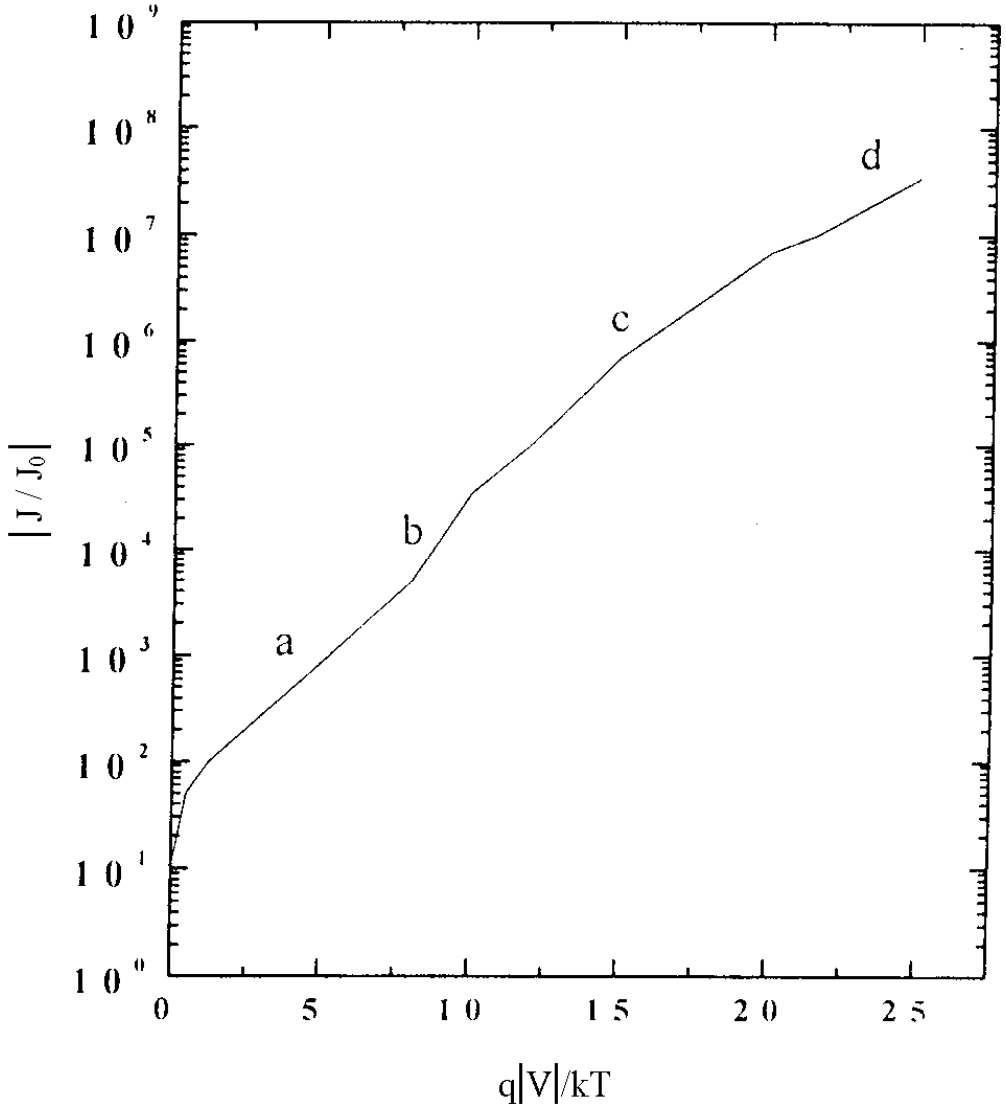

Figure 2.28 Current density versus Voltage characteristics of a practical Si diode[157]

CHAPTER 3

RESULTS AND DISCUSSIONS

Since long, silicon is dominating the market of semiconductor devices. Scientists are always searching for alternative materials for this purpose. They are also looking for element that will give a much more advantage over silicon in device fabrication process and will give a much more flexibility to alter the properties of the fabricated devices with simpler means. Carbon has shown a great potentiality in device fabrication technology. Using excimer pulsed laser deposition carbon films were deposited from C_{60} precursor in nitrogen environment at Soga Laboratory, Nagoya Institute of Technology, Japan. The optical and structural properties of the carboneous films from C_{60} precursor after N_2 incorporation are not investigated before. In order to understand the structural and optoelectronic modification of the carboneous films produced in nitrogen environment using C_{60} as target material, thorough study on the these films is necessary.

Experimented data sets of the Raman spectra (RS), transmittance and reflectance spectra at several nitrogen partial pressure (NPP) have been collected and analyzed in this thesis work. In the next section experimental details are described. In the later section the Raman spectra are analyzed and the results are interpreted. Also the optical absorption behavior of the deposited carbon films is investigated using reflectance and transmittance spectra. Characteristics of the deposited films are compared with those carbon films deposited from camphor and graphite precursor to find the scope of the deposited films in electronic application.

3.1 Experimental Details

Carbon films were deposited on single-crystal silicon (100) and 1737 corning glass substrates by XeCl excimer pulsed laser (NISSIN 10X, XeCl, λ = 308 nm, τ = 20 nsec, repetition rate = 2 Hz, spot size = 5.5 mm^2), which is focused on the target at

an incident angle of 45° to the target normal. The substrate was mounted parallel to the target at a distance of 30 mm. C_{60} powders obtained from Frontier Carbon Corporation (nanom purple N60-S) is pressed into pellets in order to use them as targets in PLD. The laser pulse energy was 140mJ on the window. To investigate the effect of nitrogen, we have introduced N_2 gas in the PLD chamber via leak valve. The pressure of the N_2 was varied between 0.3 to 500 mTorr. Prior to insert of N_2, the chamber was evacuated till about 10^{-6} Torr by a turbomolecular pump. Figure 3.1 shows the pulsed laser deposition (PLD) chamber system.

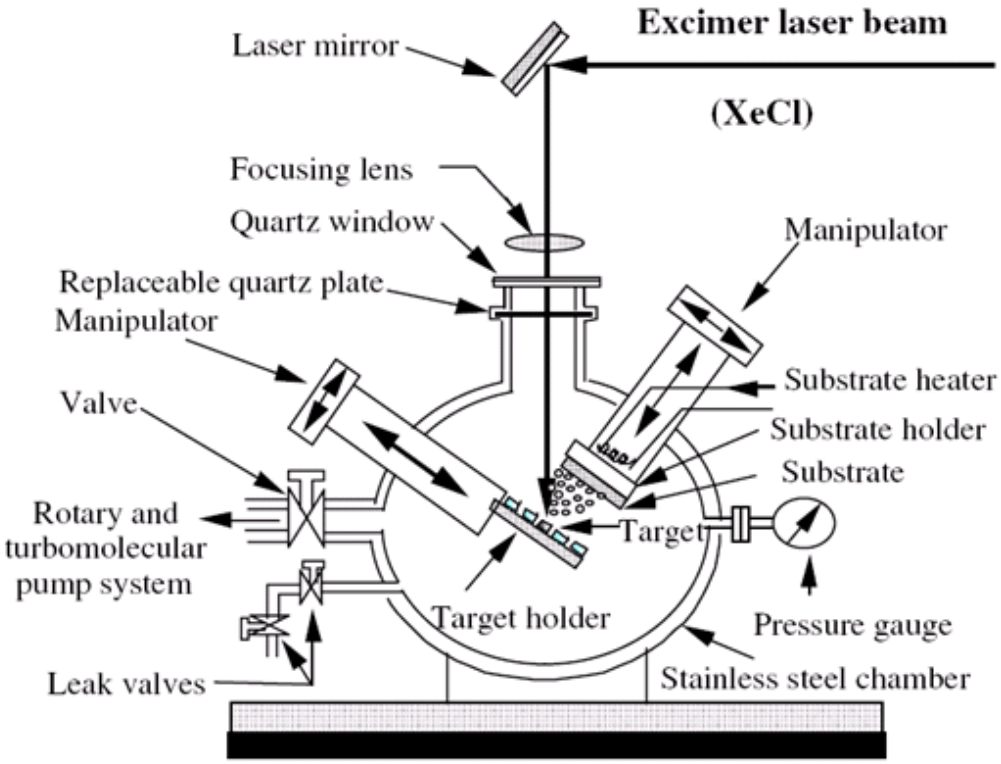

Figure 3.1 Schematic representation of the pulsed laser deposition chamber System [158]

Optical properties of the films were measured by spectral transmittance and reflectance measurements (JASCO V-570 Spectrophotometer), while structural properties were studied by Raman spectroscopy (JASCO, NRS 1500W, green laser).

3.2 Analysis of Raman Spectra of Deposited Carbon Films

3.2.1 Results of Raman Spectra Analysis

The experimental Raman data collected from previously done experiment. Raman data available in the range 1050 cm^{-1} to 1950 cm^{-1} at a step of 1.16 cm^{-1} in all the samples.

Figure 3.2 shows the Raman spectra of the carbon films deposited at without nitrogen, 4 an mTorr NPP, 10 mTorr NPP, 30 mTorr NPP, 60 mTorr NPP, 200 mTorr NPP and 500 mTorr NPP. Apparently it can be seen from the figure that there are two peaks in the Raman spectra. Both the peaks are decreasing with the increase of NPP.

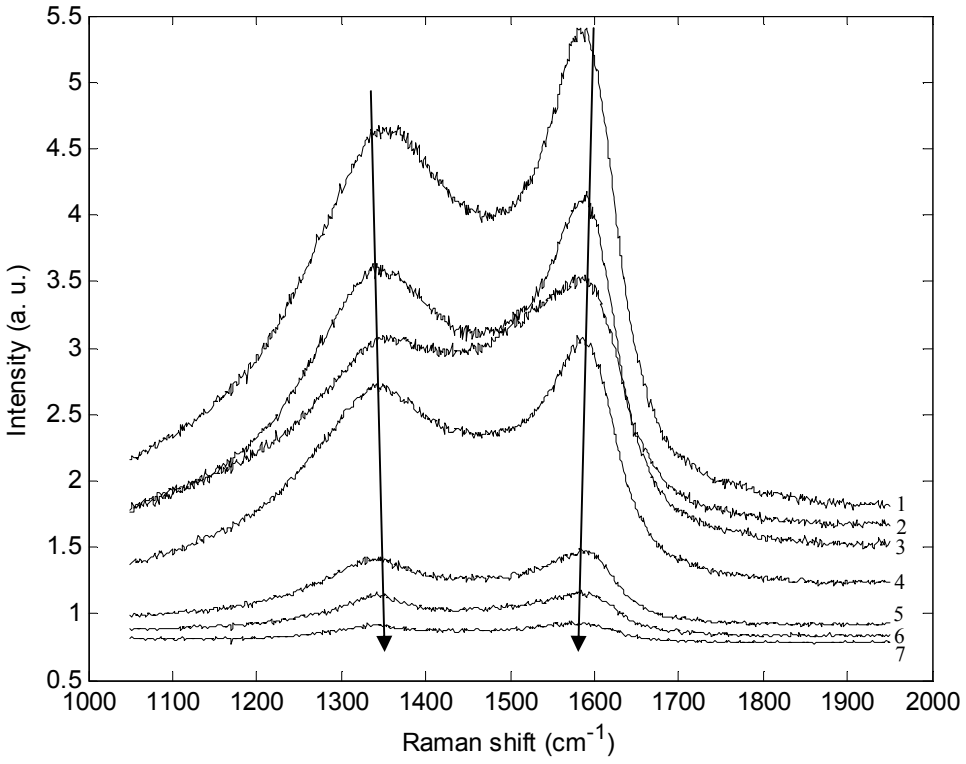

Figure 3.2 Raman Spectra of Deposited carbon film for samples (1) without nitrogen, (2) 4 mTorr NPP, (3) 10 mTorr NPP, (4) 30 mTorr NPP, (5) 60 mTorr NPP, (6) 200 mTorr NPP and (7) 500 mTorr NPP

The experimental data of the Raman of the carbon films for samples (1) without nitrogen, (2) 4 mTorr NPP, (3) 10 mTorr NPP, (4) 30 mTorr NPP, (5) 60 mTorr NPP, (6) 200 mTorr NPP and (7) 500 mTorr NPP are shown in figures 3.3, 3.4, 3.5, 3.6, 3.7, 3.8 and 3.9 respectively.

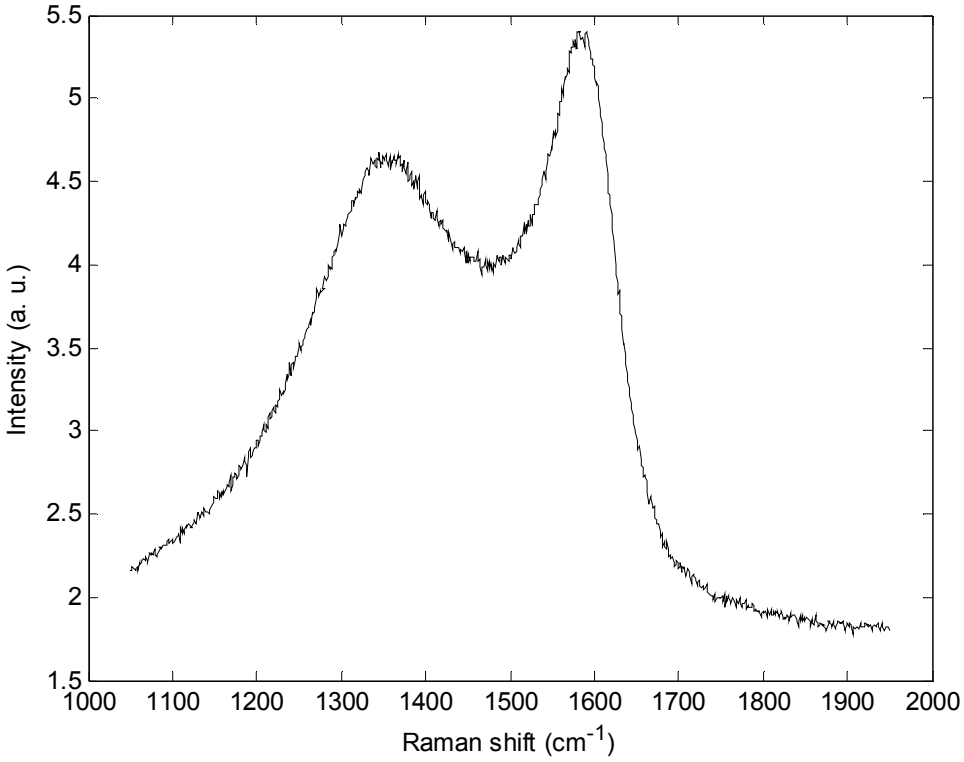

Figure 3.3 Raman spectrum of carbon film without nitrogen

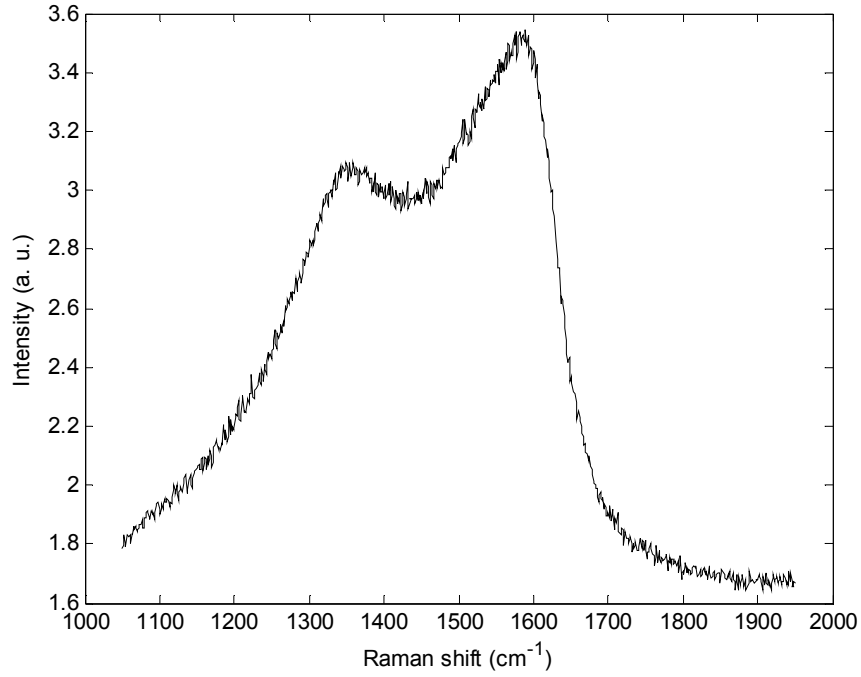

Figure 3.4 Raman spectrum of carbon film at 4 mTorr NPP

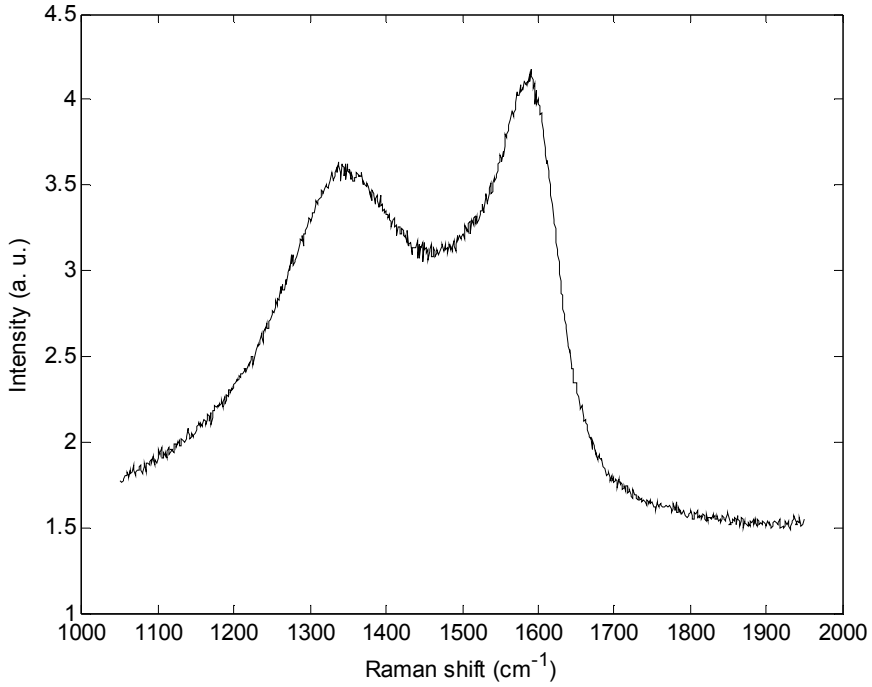

Figure 3.5 Raman spectrum of carbon film at 10 mTorr NPP

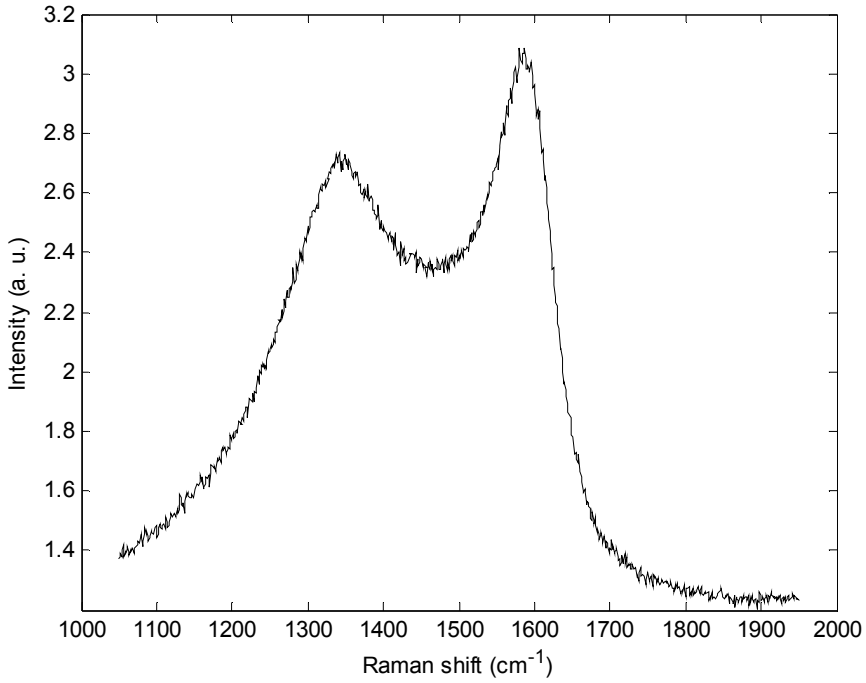

Figure 3.6 Raman spectrum of carbon film at 30 mTorr NPP

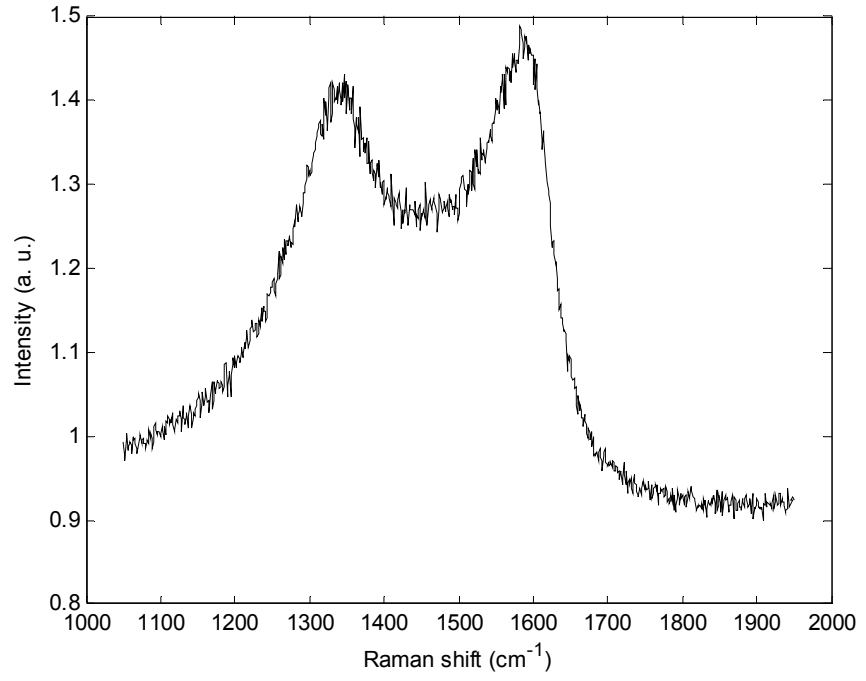

Figure 3.7 Raman spectrum of carbon film at 60 mTorr NPP

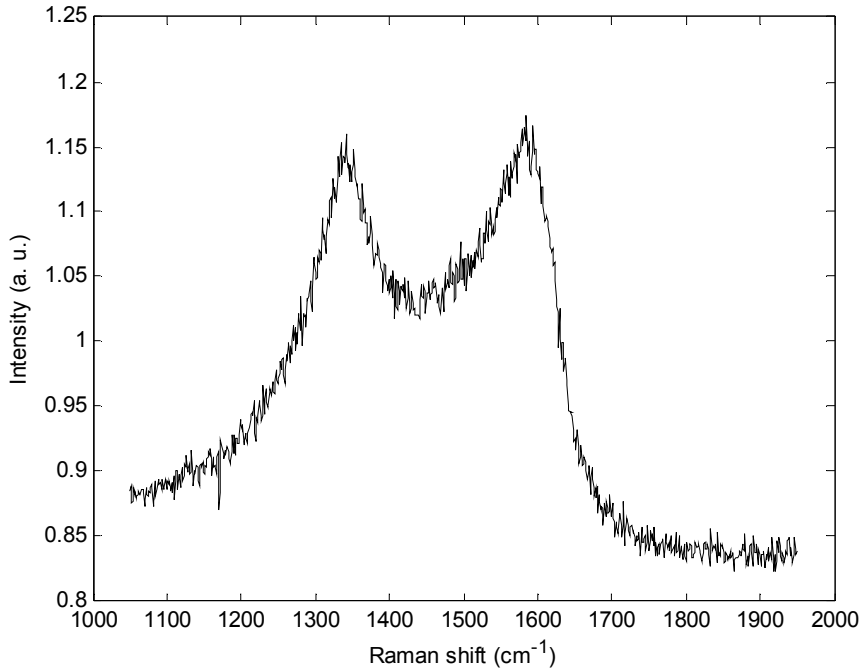

Figure 3.8 Raman spectrum of carbon film at 200 mTorr NPP

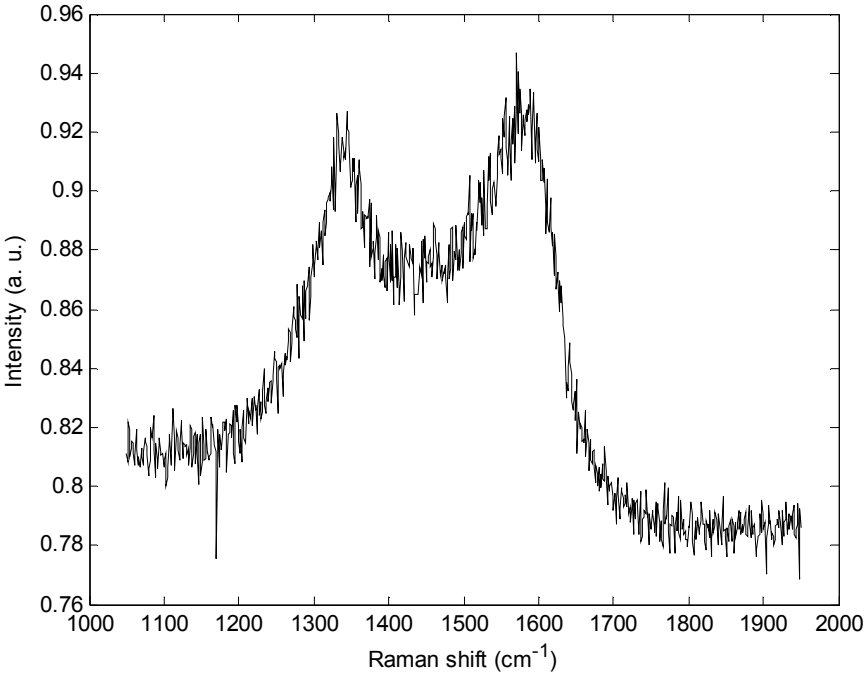

Figure 3.9 Raman spectrum of carbon film at 500 mTorr NPP

The Raman spectra are fitted with several peaks for structural characterization of carbon films. Firstly, the raw data is smoothed several times for the elimination of small systematic variations in intensity.

The second step for the analysis of the spectra is background subtraction. The objective of background subtraction is to remove a constant offset from the signal. We have used Shirley background in our work. The Raman Spectrum with background and after background subtraction for the sample without nitrogen is shown in figures 3.10 and 3.11 respectively. Figures 3.12 and 3.13 respectively show the Raman Spectrum with background and after background subtraction for sample with 30 mTorr NPP.

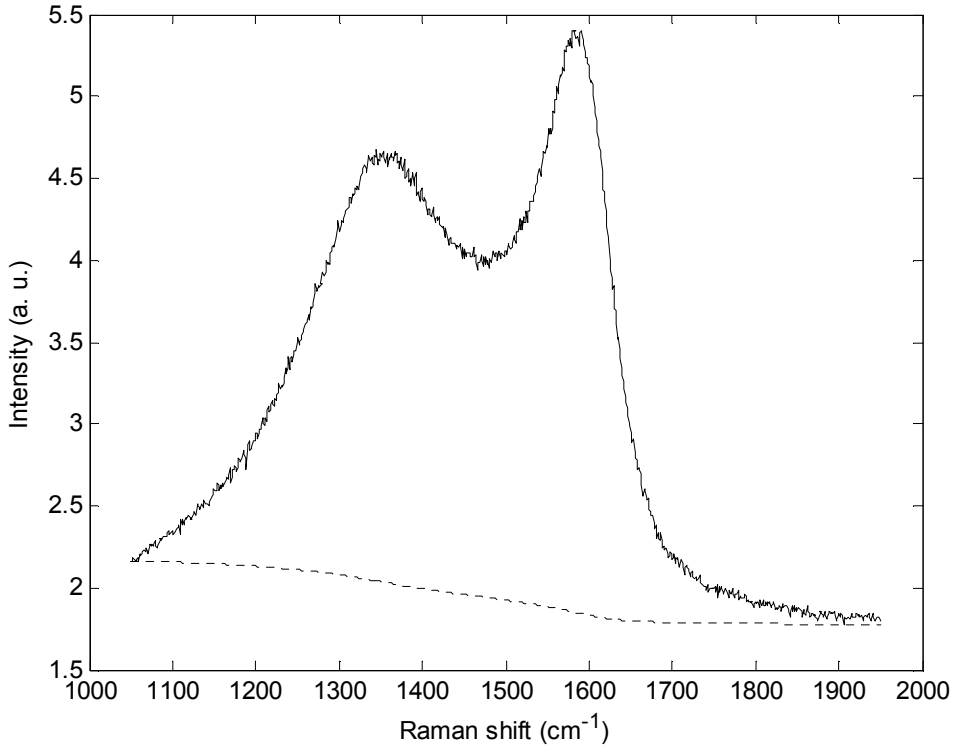

Figure 3.10 Raman spectrum with background of the carbon film deposited in nitrogen free environment

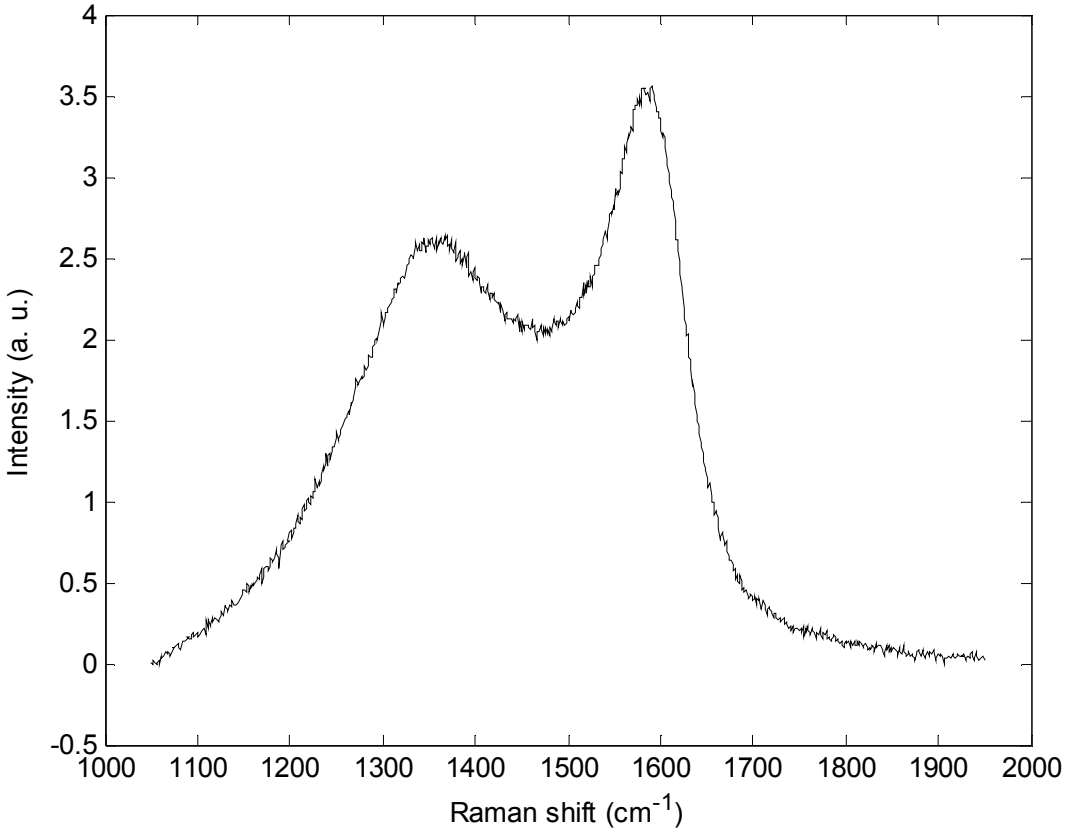

Figure 3.11 Raman spectrum after background subtraction of the carbon film deposited in nitrogen free environment

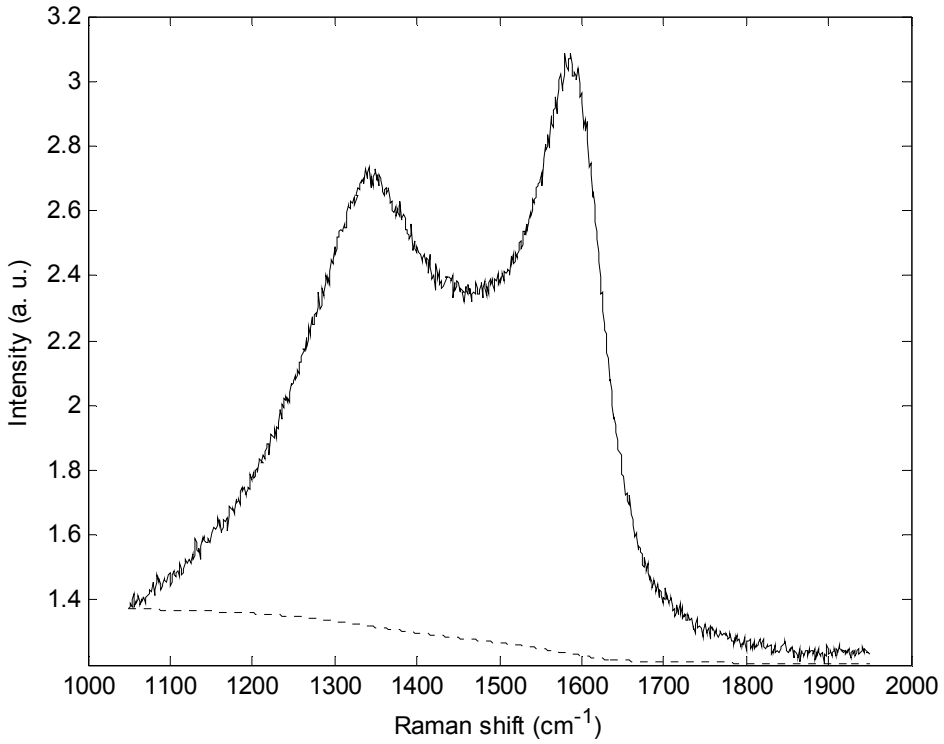

Figure 3.12 Raman spectrum with background of the carbon film deposited in 30 mTorr NPP

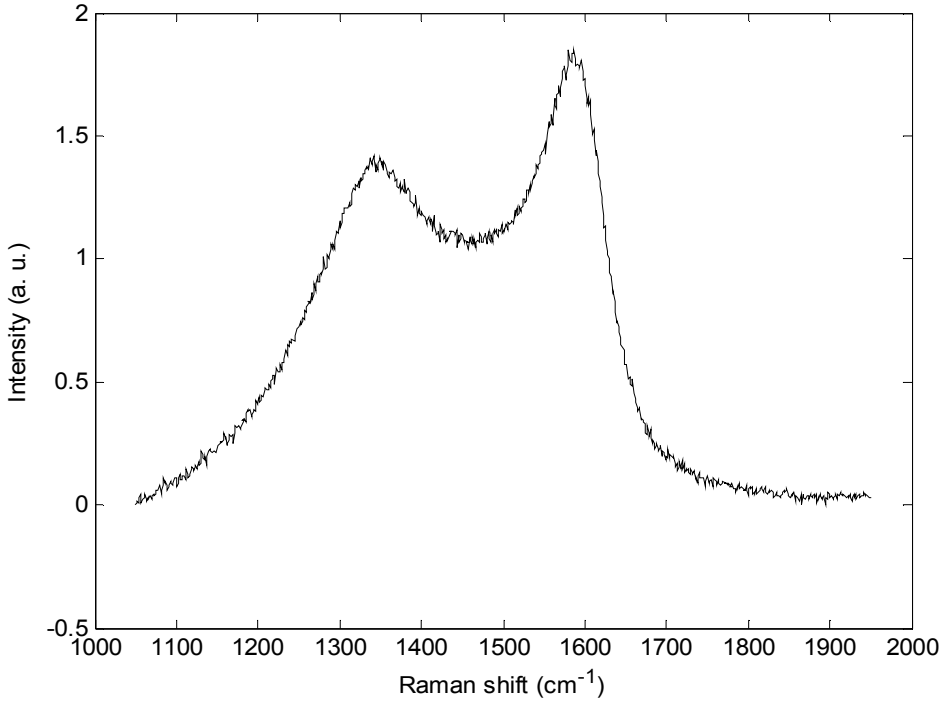

Figure 3.13 Raman spectrum after background subtraction of the carbon film deposited in 30 mTorr NPP

After background subtraction the next step is to fit the Raman Spectra with a number of suitable peaks. Any measured spectrum can be fitted with any number of peaks. So we start fitting the spectra with two peaks as two peaks are apparently visible. Figure 3.14 shows the fitted Raman spectrum for the film deposited in nitrogen free environment.

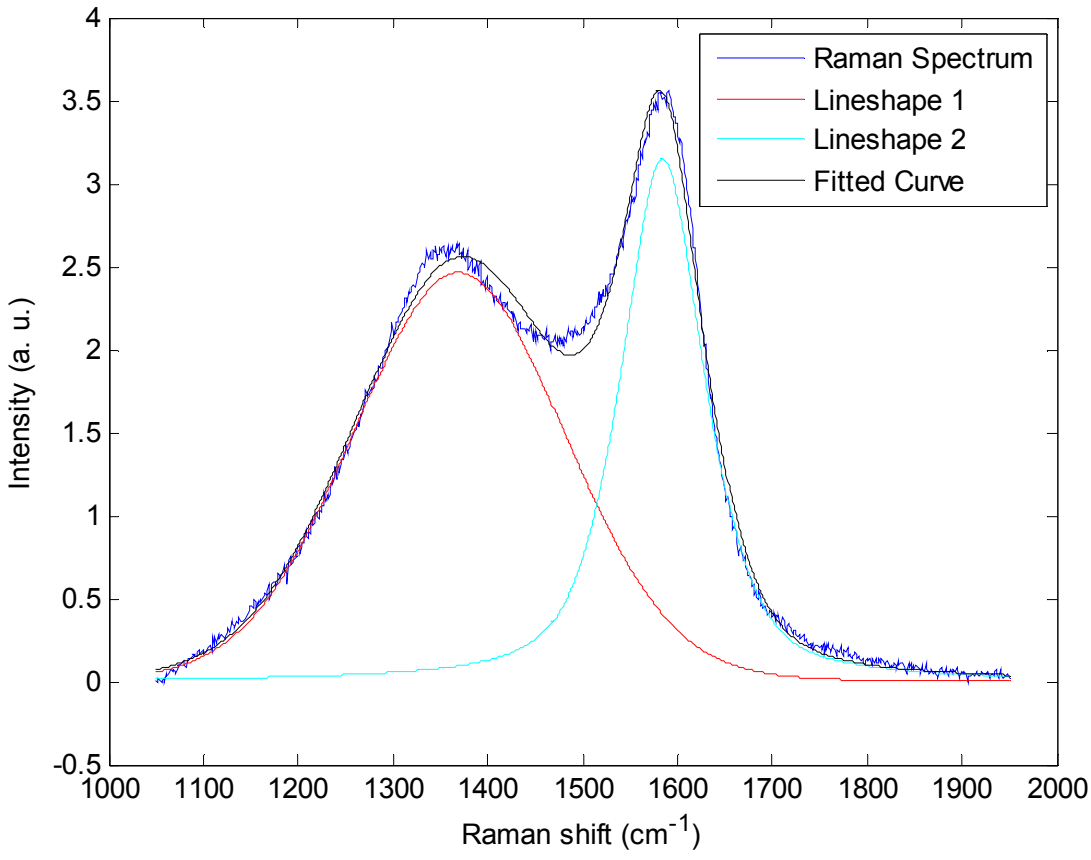

Figure 3.14 Fitted Raman spectrum of the carbon film deposited in nitrogen free environment

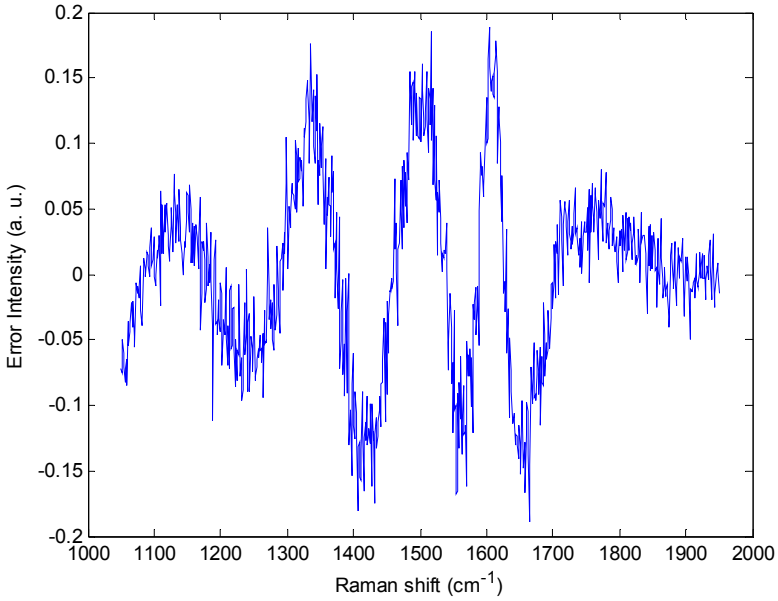

Figure 3.15 Error curve for fitting with two peaks for film deposited without nitrogen

Fitting with two peaks produces a significant error. Difference between actual curve and fitted curve which is called residuals is displayed in figure 3.15. From the figure it can be seen that the residual has quite random characteristics i.e. the residual change its polarity quite frequently. Its chi-square is 4.6231 and sum of squared error is 3.8575.

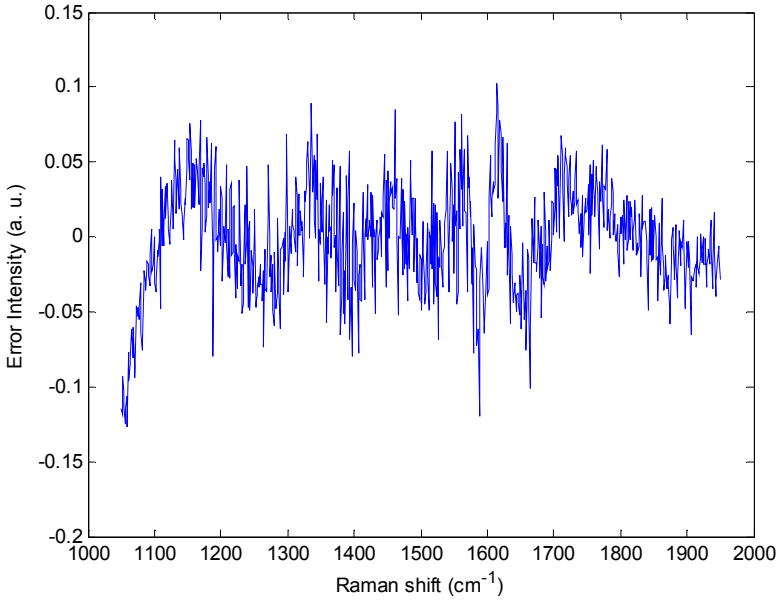

Figure 3.16 Error curve for fitting with three peaks for film deposited without nitrogen

Since the principle of the improvement of the fit is starting with minimum number of bands indicated by the topology of RS (maxima and inflections) and increasing this number of bands until no further improvement in sum of squared error occurs. So we can fit the curve by 3 peaks and error analysis showed that fitted data with 3 peaks matched more with the actual data than with 2 peaks because in the former case error is reduced substantially. Figure 3.16 shows that error is reduced and randomness of the error is increased for curve fitted with three peaks.

The error analysis for all the samples is given in the table 3.1. Moreover the randomness of the residuals for 3 bands is improved than 2 bands. Besides in the actual curve for sample without nitrogen there is an inflection point around 1490 cm^{-1}, so it is reasonable to fit the data with 3 bands rather than 2 bands.

Table 3.1 Error analysis using two and three peaks

	MMSE		**Chi square (χ^2)**	
No. of Peaks	2 peaks	3 peaks	2 peaks	3 peaks
Nitrogen Free	3.8575	1.0011	4.6231	3.4453
4 mTorr NPP	1.5325	0.5767	7.0658	4.2211
10 mTorr NPP	3.6926	0.6428	5.2956	2.6462
30 mTorr NPP	1.9765	0.3891	3.8334	2.1367
60 mTorr NPP	0.4329	0.1334	4.8626	3.0018
200 mTorr NPP	0.2110	0.0748	4.2094	2.7673
500 mTorr NPP	0.0373	0.0092	2.4257	0.9229

The values of table 3.1 are plotted in the figures 3.17 and 3.18. For plotting purpose, we have assumed that nitrogen free condition has NPP of 10^{-4} Torr .

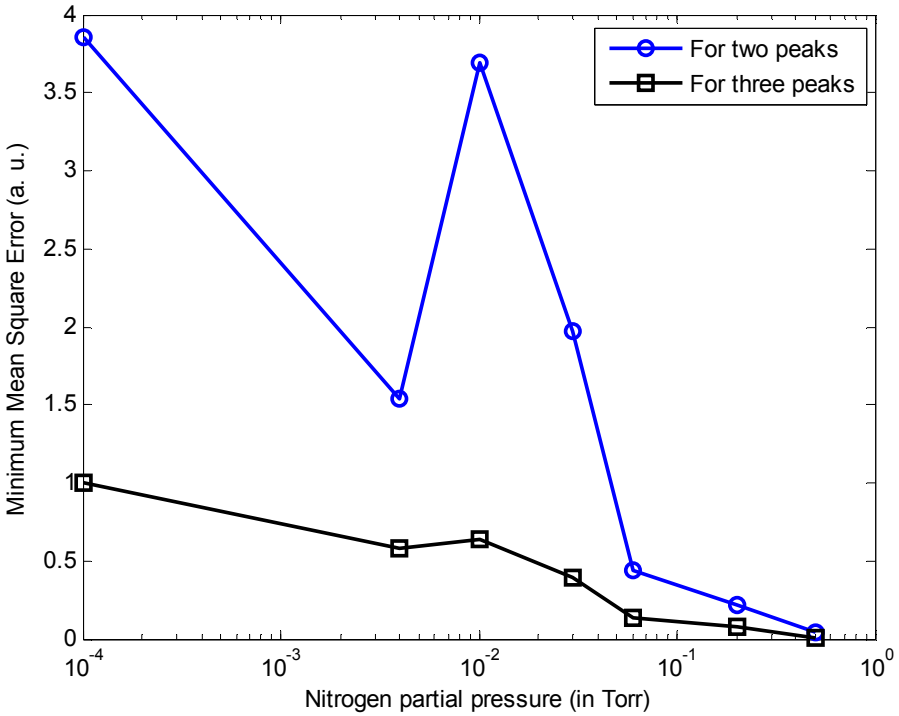

Figure 3.17 MinimumMean Square Error comparison for curve fitted with two and three peaks

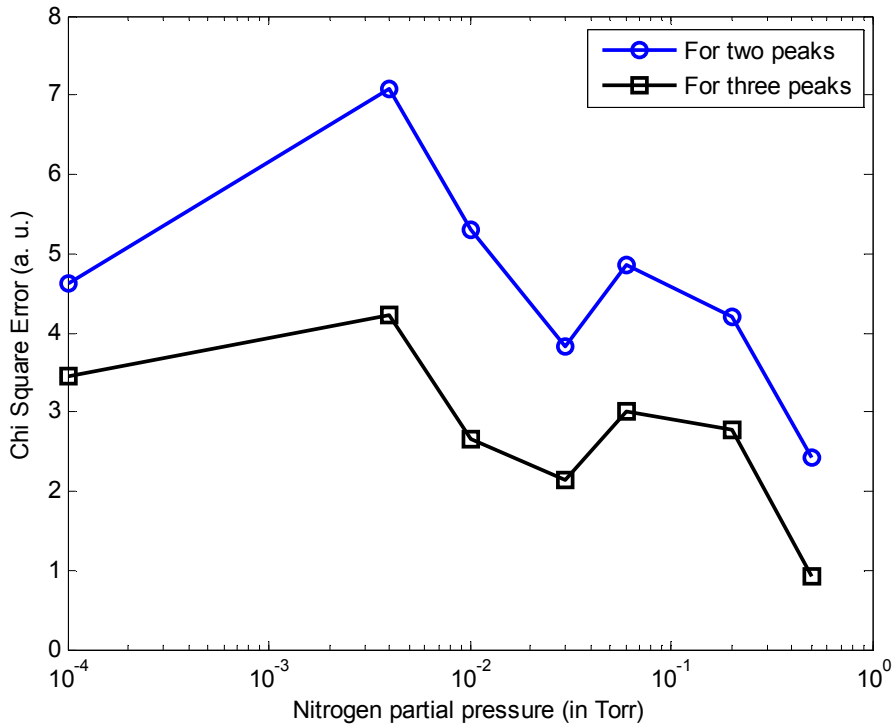

Figure 3.18 Chi Square comparison for curve fitted with two and three peaks

Table 3.2 Error Table for MMSE and Chi square(χ^2) for different percentage of Gaussian line in the line shapes

NPP	Gaussian %	0	10	20	30	40	50	60	70	80	90	100	free
Nitrogen Free	MMSE	1.00	1.00	1.01	1.01	0.89	0.86	0.88	0.95	1.00	1.02	1.04	1.00
	χ^2	3.44	3.47	3.50	3.55	3.62	3.43	3.51	3.83	4.04	4.03	4.04	3.44
4 mTorr NPP	MMSE	0.57	0.57	0.57	0.57	0.57	0.54	0.53	0.52	0.53	0.54	0.55	0.58
	χ^2	4.21	4.22	4.22	4.23	4.25	4.27	3.96	3.80	3.74	3.73	3.74	4.22
10 mTorr NPP	MMSE	0.64	0.64	0.64	0.59	0.55	0.55	0.58	0.61	0.64	0.66	0.69	0.64
	χ^2	2.64	2.66	2.70	2.99	2.65	2.60	2.77	2.99	3.06	3.08	3.11	2.65
30 mTorr NPP	MMSE	0.38	0.39	0.39	0.13	0.36	0.36	0.38	0.40	0.41	0.42	0.44	0.39
	χ^2	2.13	2.15	2.18	2.17	2.04	2.08	2.20	2.31	2.35	2.38	2.41	2.14
60 mTorr NPP	MMSE	0.13	0.13	0.13	0.36	0.13	0.12	0.12	0.12	0.12	0.13	0.13	0.13
	χ^2	3.00	2.98	2.96	2.95	3.05	2.67	2.43	2.30	2.24	2.21	2.20	3.00
200 mTorr NPP	MMSE	0.07	0.07	0.07	0.07	0.07	0.07	0.07	0.07	0.07	0.07	0.07	0.07
	χ^2	2.76	2.75	2.73	2.71	2.89	2.54	2.31	2.17	2.09	2.04	2.04	2.77
500 mTorr NPP	MMSE	0.01	0.01	0.01	0.01	0.01	0.01	0.01	0.01	0.01	0.01	0.01	0.01
	χ^2	1.07	1.05	1.04	1.21	0.99	0.87	0.80	0.78	0.78	0.78	0.78	0.92

Improvement in error can easily be seen in the figure 3.17 and 3.18. For further improvement the data is fitted with 4 bands. But investigation on error analysis proved that 4 bands degrade the fitting quality. And we cannot fit the data without constraints on line parameters (peak position, FWHM, intensity percentage of Gaussian).

Again there are a lot of options in our hand that we can fix or vary any one of the line parameters. The best option is to free all the line parameters and finding these line parameters for minimum value of error which we call minimum mean squared error (MMSE). The software that we have developed has these options to fix any one of the line parameters or to make it free. Let assume that peak position, FWHM and intensity are free and we want to find out for what percentage of Lorentzian (the rest of percentage is for Gaussian) is required for MMSE. This percentage of Lorentzian is varied from 0 percentages to 100 percentages and found out the error. The MMSE and chi square error values are given in the table 3.2.

In the table there is a column named free which indicates the error values when this there are no constraint given on the percentage parameter. For this case error value may be higher than certain percentage. But this is obvious since all the parameters are free here and all of them will try to find a suitable value for MMSE. The final value those we have found for MMSE making all the parameters free are given in the appendix II.

Now we can analyze each fitted curve for different nitrogen Partial Pressure (NPP). The fitter curves for different NPP are shown in figures 3.20 to 3.26. We have said earlier that we have used C_{60} as a precursor to grow semiconducting carbon films. We have discussed previously about intermolecular modes of $C_{60.}$ And C_{60} has 10 Raman active modes. And, we concentrate our attention on the region 1000-1950 cm^{-1}. It is found from the fitted curve that the 3 peaks are located at around 1357.4 cm^{-1}, 1529.3 cm^{-1} and 1592.1 cm^{-1}. The Raman spectrum of pristine C_{60} shows the most intense peak at 1469 cm^{-1} (as shown in figure 2.22) which corresponds to the pentagonal pinch mode (the A_g internal mode of C_{60}). The Raman spectrum of bulk fullerene is shown again in figure 3.19 for better understanding. This is the vibrational mode where tangential stretch occurs indicating that every pentagon is

contracted and every hexagon is expanded. Instead there is a peak around1529.3 cm^{-1}. We can treat this peak as shifted version of fullerene peak. Same phenomena was found by Bajwa *et al.*[17] but that experiment was not N_2 incorporated.

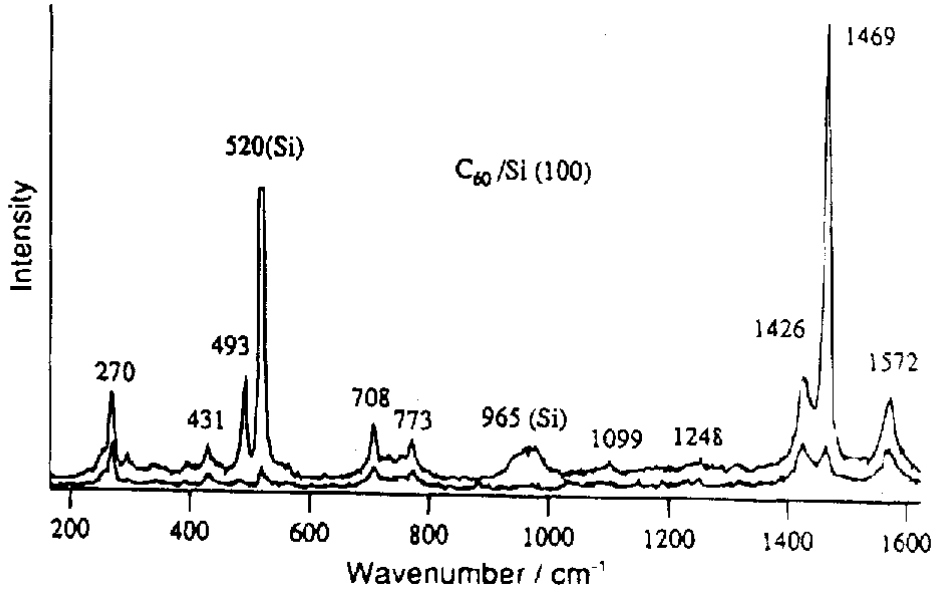

Figure 3.19 Raman spectra for C_{60} on a Si (100) substrate. The upper trace is for the (||, ||) polarization and the lower trace is for the (||, ⊥) polarization [139]

The broad feature around 1350 cm^{-1} can be attributed to first order scattering from zone boundary phonons, where density of states is maximum, activated by disorder/confinement, also referred to as the D peak[162] (D is conventionally for disorder). D peak contribution can be from aromatic clusters of sixfold rings of sp^2 sites, as well as due to amorphous carbon from all sp^2 ring-like structures. In other words, D peak can be due to disorder in nanocrystalline graphitic clusters or due to sp^2 in sp^2-sp^3 *a*-C network in which it is embedded[134, 163]. It is important to note that pristine C_{60} has a sharp H_g symmetry mode at 1570 cm^{-1}. For pristine C_{60}, the H_g symmetry mode has a FWHM of ~12 cm^{-1} whereas the FWHM for the first film that is deposited without N_2 increases to 88 cm^{-1}. Thus the broad peak at 1570 cm^{-1} cannot be the H_g peak, but a new feature. It is attributed that the broad feature

around 1592.1 cm^{-1} as the G peak [163] despite its being upshifted from the characteristic bulk graphite peak (~1575 cm^{-1}). Broadening of this peak indicates deviation from the bulk crystalline graphite. However, this identification is not unique to graphite like, as olefinic molecules are also known to show peaks around this [134]. Since the width of this peak (~88 cm^{-1}), spread on either side of peak maxima, covers the position of characteristic bulk graphite peak as well as the G peak appearing in amorphous carbon (1560 cm^{-1}), we would be tempted to identify it as the G peak. Therefore, the simultaneous appearance of the G peak (1592 cm^{-1}) and the D peak (1357 cm^{-1}) are indication of *a*-C formation. Deviations in the position and relative intensities of D and G peak (I_d /I_g ratio) will be explained later.

For carbon film deposited in 4 mTorr NPP, fitted curve of the Raman spectrum also have 3 peaks but located at slightly different position. The 3 line positions are 1362.2 cm^{-1}, 1537.9 cm^{-1} and 1600.6 cm^{-1}. For the same reason described above we define these 3 peaks as D, F, and G peaks where F denotes fullerene peak. Fitted Raman spectrum of the carbon film is shown in the figure 3.21.

For carbon film deposited in 10 mTorr NPP, fitted curve of the Raman spectrum also have 3 peaks as can be seen in figure 3.22. The 3 line positions are 1349.5cm^{-1}, 1525.6cm^{-1} and 1593.3cm^{-1}. These three peaks are considered as D, F, and G peaks, respectively.

The three line positions of the fitted curve of the Raman spectrum are 1345.7 cm^{-1}, 1516.2 cm^{-1} and 1592.0 cm^{-1} in 30 mTorr NPP. These peaks are denoted as D, F and G peak respectively. The fitter spectrum is shown in figure 3.23.

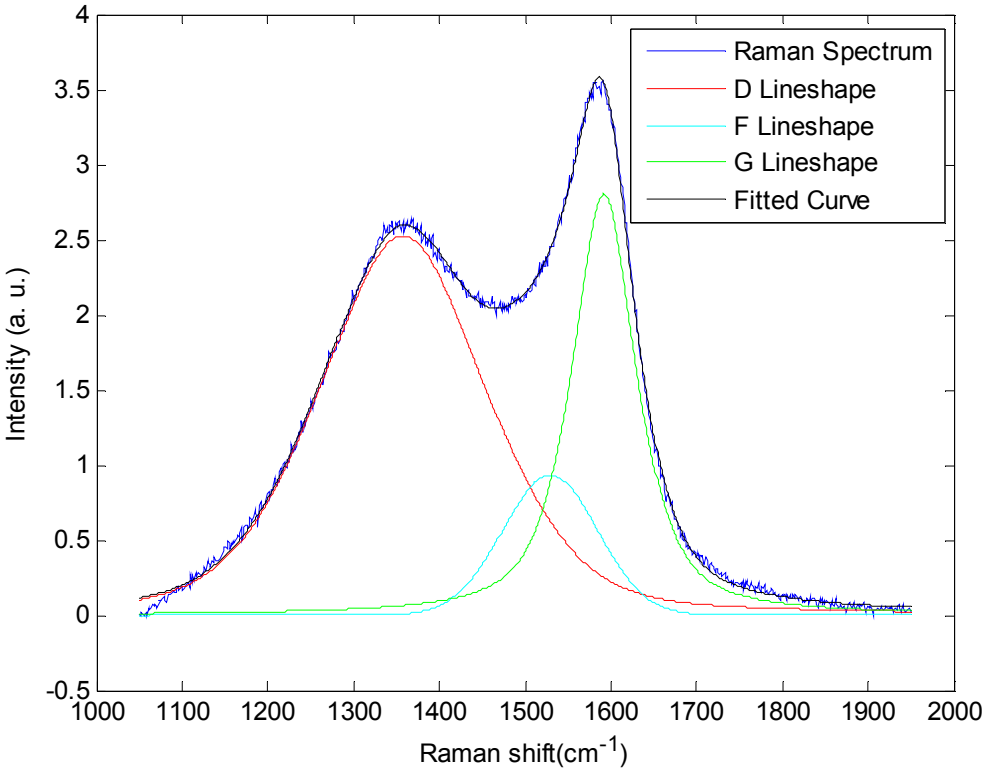

Figure 3.20 Fitted Raman spectrum of the carbon film deposited in nitrogen free environment with three peaks

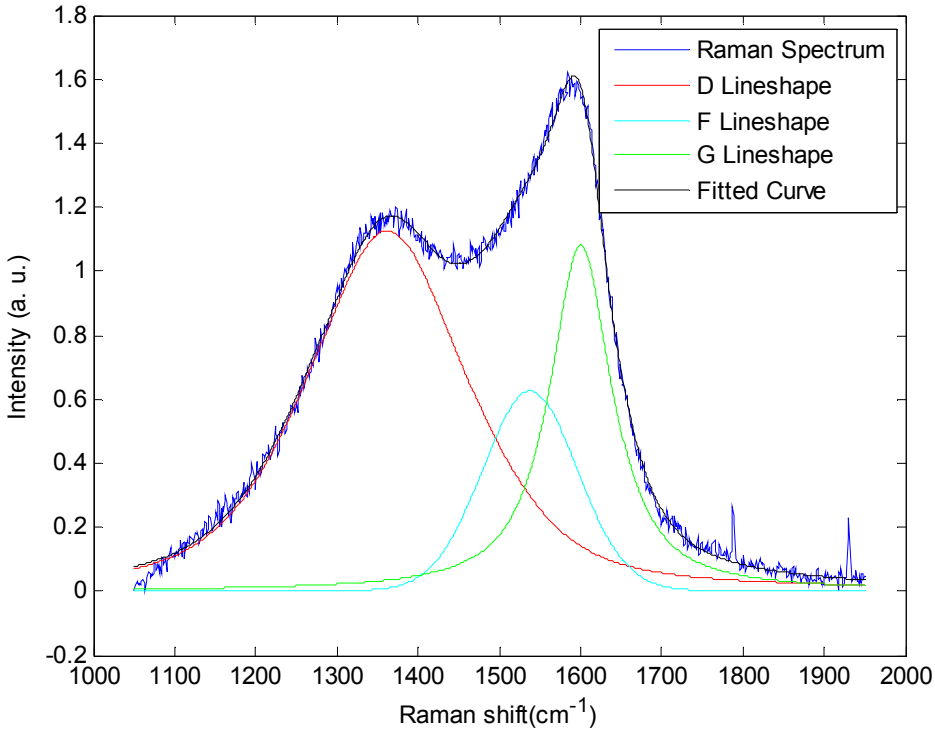

Figure 3.21 Fitted Raman spectrum of the carbon film deposited in 4 mTorr NPP

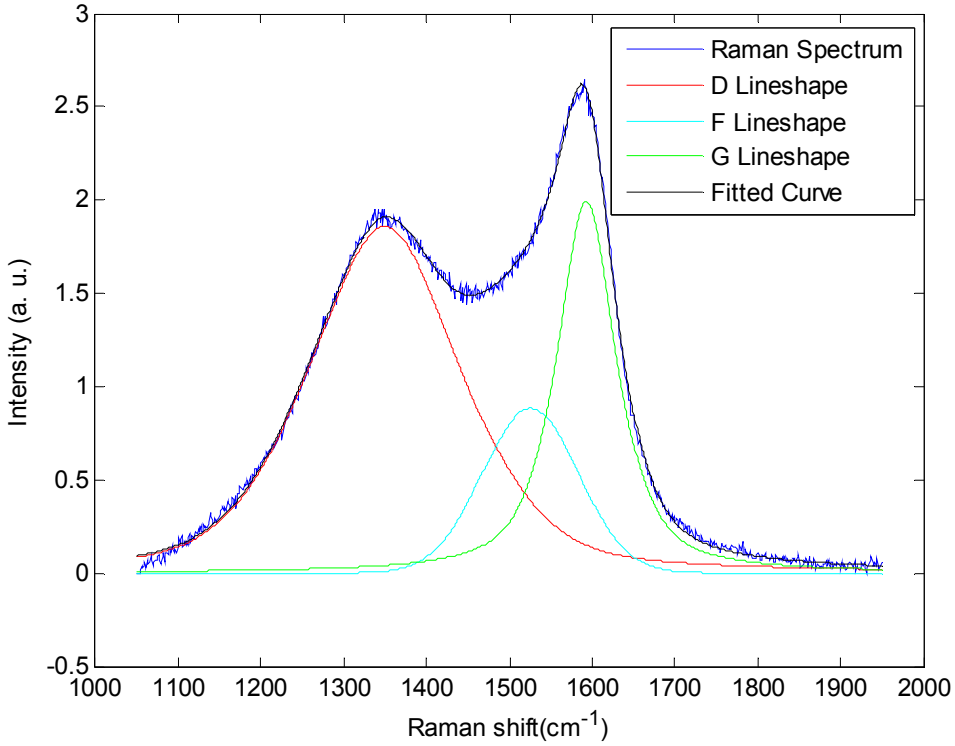

Figure 3.22 Fitted Raman spectrum of the carbon film deposited in 10 mTorr NPP

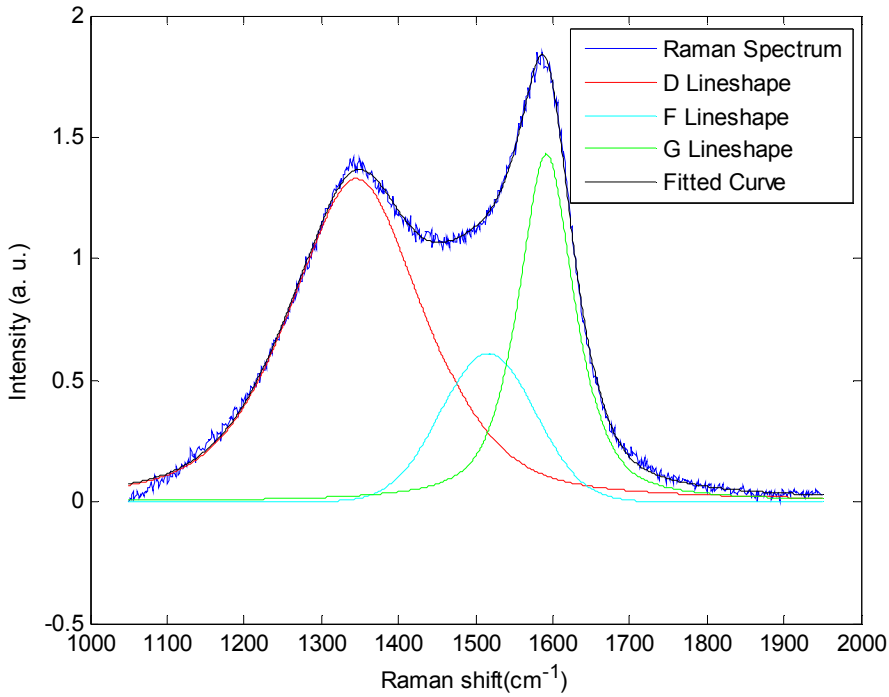

Figure 3.23 Fitted Raman spectrum of the carbon film deposited in 30 mTorr NPP

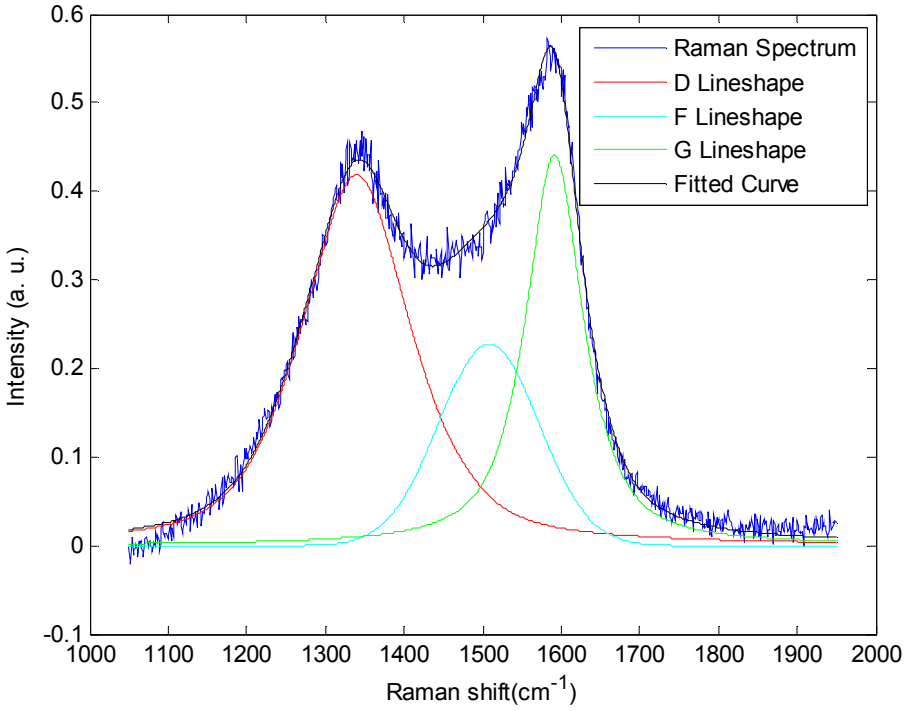

Figure 3.24 Fitted Raman spectrum of the carbon film deposited in 60 mTorr NPP

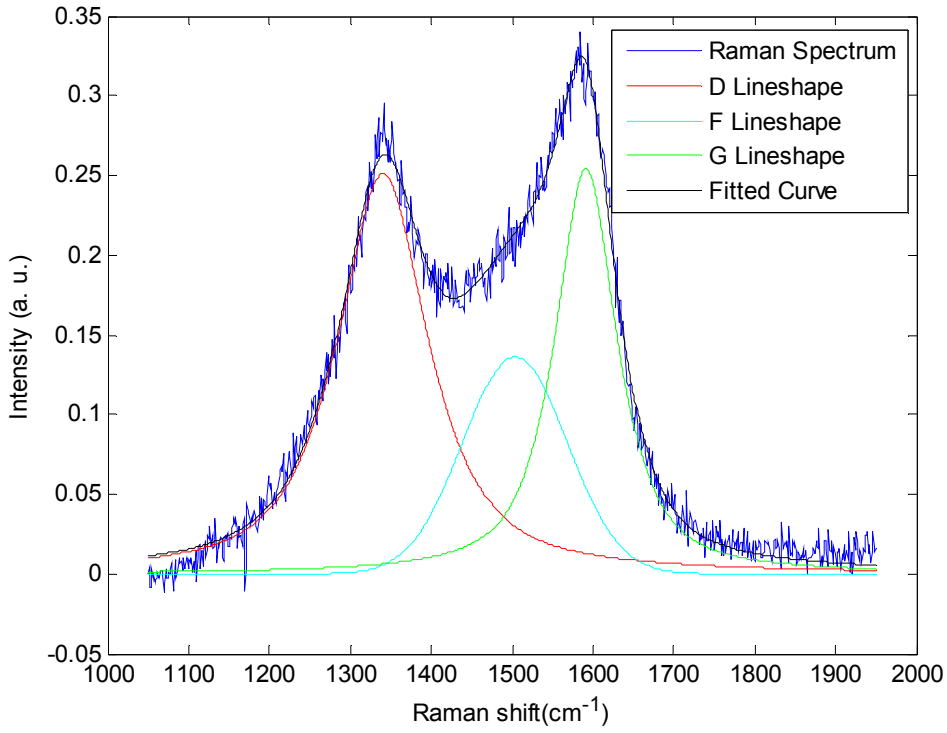

Figure 3.25 Fitted Raman spectrum of the carbon film deposited in 200 mTorr NPP

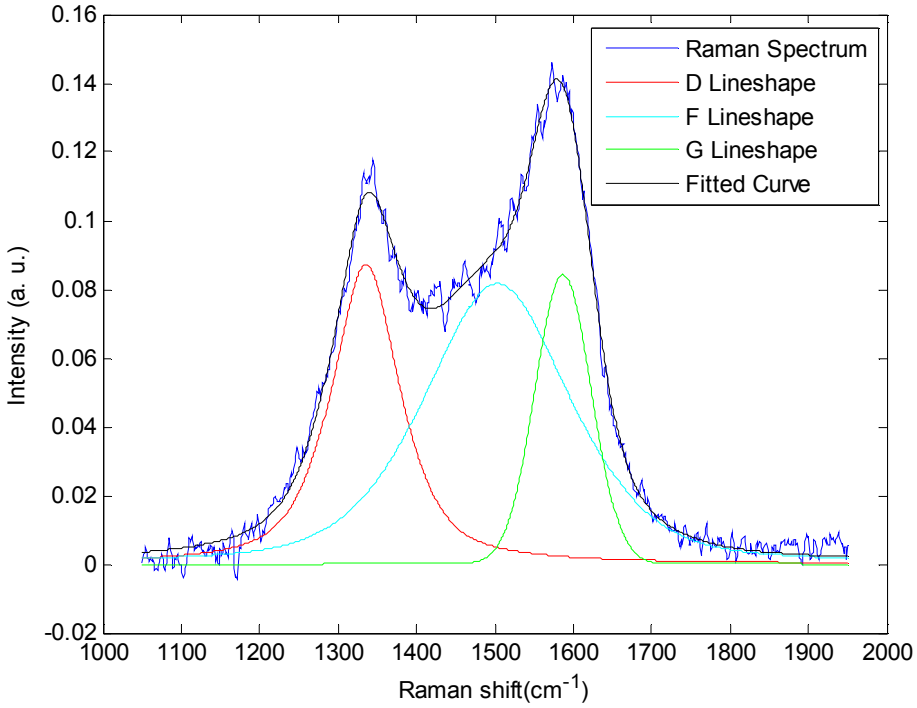

Figure 3.26 Fitted Raman spectrum of carbon film deposited in 500 mTorr NPP

The D, F and G line positions of the fitted curve of the Raman spectrum are 1339.5 cm^{-1}, 1508.1cm^{-1} and 1591.7 cm^{-1} in 60 mTorr NPP as shown in figure 3.24.

For carbon film deposited in 200 mTorr NPP, Fitted curve of the Raman spectrum have 3 peaks as can be seen in figure 3.25. The 3 line positions are 1340.4 cm^{-1}, 1503.7 cm^{-1} and 1591.6 cm^{-1}. For the same reason described above we call these 3 peaks as D, F, and G peaks where F denotes fullerene peak.

For 500 mTorr NPP the Raman Spectrum is fitted with three peaks having positions at 1335.4 cm^{-1}, 1503.1 cm^{-1} and 1587.2 cm^{-1}. As mentioned earlier the peaks are called D, F and G peak respectively.

3.2.2 Interpretation of Raman Spectra Analysis results

The Raman spectra of the carbon film in differnet nitrogen partial pressure is fitted with three peaks as shown in the former section. In this sction, the findings from the fitting of the Raman spectra will be discussed. For plotting purpose, the NPP of the nitrogen free condition is asssumed to be 10^{-4} mTorr.

Figure 3.27 shows the G line or peak position variation with NPP. Here the curve initially up shifted from 1592.1 cm^{-1} to 1600.6 cm^{-1} and then decreases gradually to 1587.2 cm^{-1}. It is almost constant at 1592 cm^{-1} from the 10mTorr to 200 mTorr NPP. All the peak positions are greater than the principal value of graphite placed at 1580 cm^{-1}. G line position varies from its original position more in a-C and variation is proportional to disorder [24]. The G peak does not disperse in graphite itself, nanocrystalline-G (nc-G) or glassy carbon. The G peak only disperses more in disordered carbon, where the dispersion is proportional to the degree of disorder. This is an important finding, by which the physical behavior of the G peak in disordered graphite is radically different from amorphous carbons, even though the G peak positions might accidentally be the same at some excitation energy. The G peak dispersion occurs only in more disordered carbon, because now there is a range of configurations with different local band gaps and different phonon modes. The dispersion arises from a resonant selection of sp^2 configurations or clusters with wider p band gaps, and correspondingly higher vibration frequencies. In materials with only sp^2 rings, the G peak dispersion saturates at a maximum of ~1600 cm^{-1}, the G position in nc-G. Dispersion of the C-C stretching modes occurs in transpolyacetylene [164, 165]. In contrast, the C-C stretching modes have no dispersion in polyparaphenylene (σ bonded chains of benzene rings) [166]. This is because the π electrons are confined to each benzene ring, and do not delocalize along the chain [166]. Only the introduction of a heteroatom (or disorder) allows π delocalization and thus dispersion [166].

The G peak position values indicate a form like graphene like structure with disorder. Ultimately the graph is downshifted to 1587.2 cm^{-1} which is for highest N_2 content. This is due to N_2 incorporation as N_2 incorporation causes a-C's G position

to decrease [167]. Same behavior of decreasing G line position for nitrogen incorporation was found by Ferrari *et al*.[134]. Figure 3.28 shows this behavior. It indicates nitrogen incorporation makes deposited film containing less disorder.

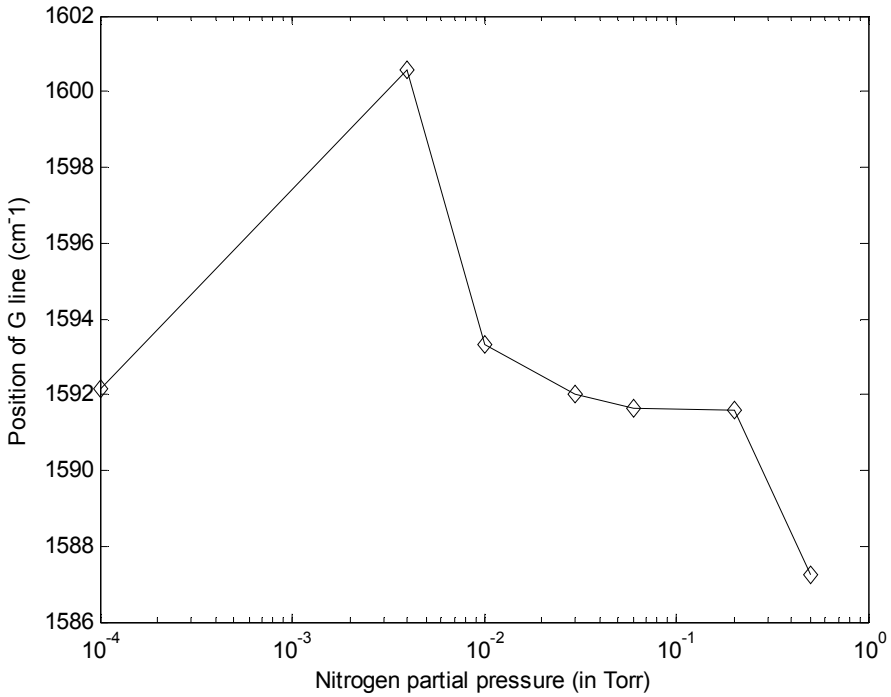

Figure 3.27 G peak position variation with NPP

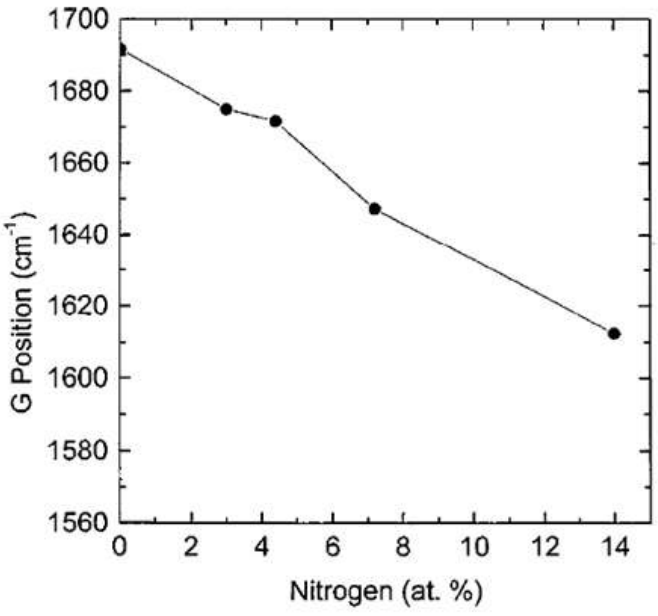

Figure 3.28 The almost linear decreasing of G peak position at 244nm [134]

Variation of the D peak position as function of NPP is shown in figure 3.29. Up to 4 mTorr partial pressure D peak position is upshifted from initial value and then downshifted. Its variation range is 1335.4 ~ 1362.2 cm^{-1}. The actual value of D peak position for crystalline graphite is 1360 cm^{-1}. For lower nitrogen content (up to 4 mTorr) carbon films have higher value than this actual value but rest of the samples has lower value. The increasing value of D line position indicates a decrease in the bond angle disorder. Here, it can be interpreted as the decrease due to the passivation of bond by nitrogen. Afterward, downshifting of D line indicates the presence of sp^3 C [168] may be due to breaking of double bond of sp^2 and incorporation of nitrogen atom. The same conclusion as from the G line position, carbon film attains graphitic sheet like structure [133].

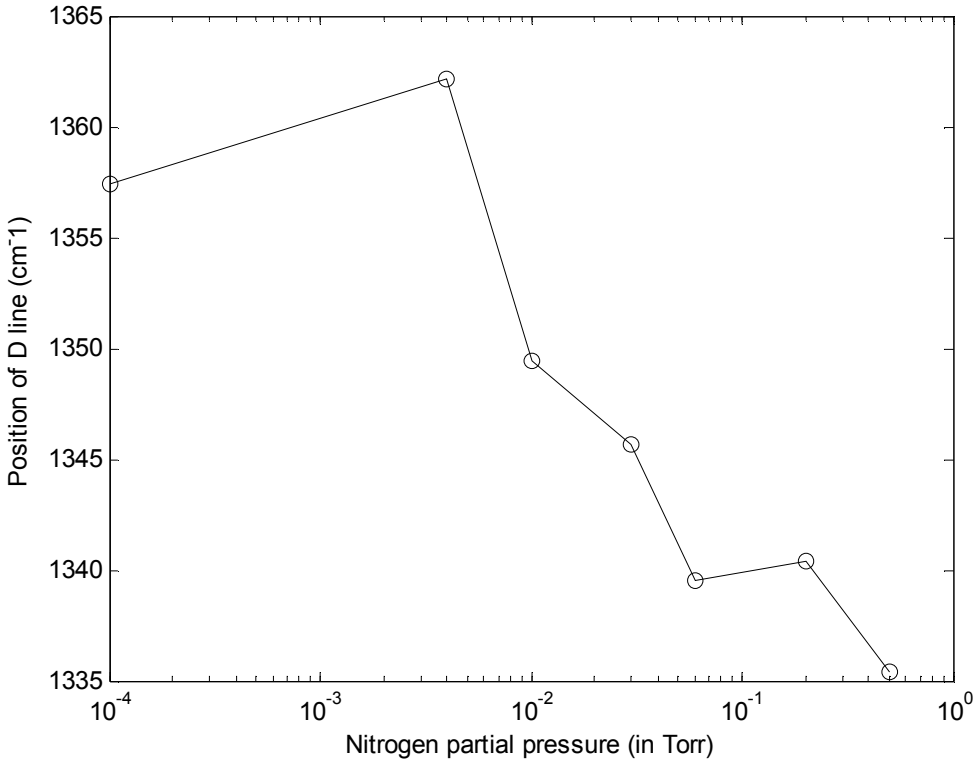

Figure 3.29 D peak position as a function of NPP

The shift of the F (fullerene) line as a function of N_2 content is shown in figure 3.30. The curve decreases continuously after an initial upshifting from with nitrogen condition to 4 mTorr NPP. For 500 mTorr which has the highest N_2 content is located at 1500 cm^{-1}. This is an indication of polymerized C_{60} though peak position of polymerized C_{60} is at 1460 cm^{-1} [17, 19, 169, 170]. The spectrum of peak located at 1500~1530 cm^{-1} is quite broad in nature. We know formation of intermolecular polymeric bonds between C_{60} molecules moves away some of the electrons from the intermolecular double bonds and hence soften the $A_g(2)$ modes and broadens it. In one of the works of Mominuzzaman *at el.* [22] on same experiment with the variation of substrate temperature and there was no N_2 incorporation, he reported that fullerene is polymerized due to high energetic particle evolution of C_{60}.

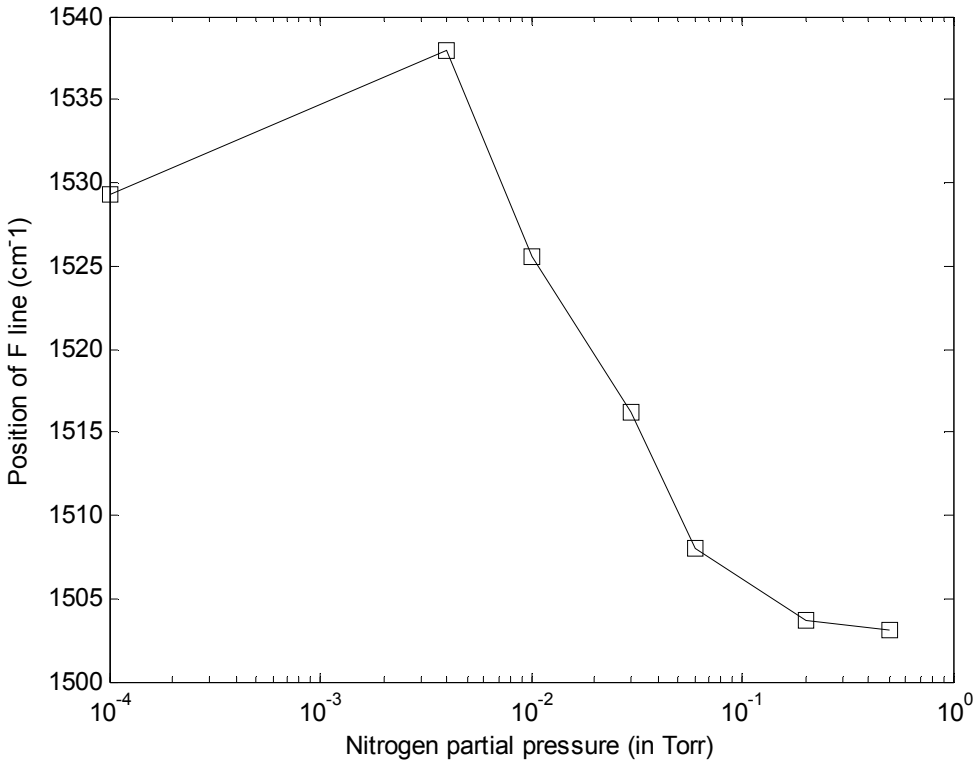

Figure 3.28 F peak position as a function of NPP

I_d/ I_g ratio is one of the important parameter and together with G peak position we can explain the bond arrangement. I_d and I_g are integrated areas of D peak and G peak respectively and I_d/ I_g ratio are presented in figure 3.31.

Since I_d/ I_g ratio is the ratio of momentum of nonconserving to conserving phonons it will decrease for more crystallites because in large crystal momentum is conserved [172].

I_d/ I_g ratio increases initially and then decreases from 2.17 to 1.563. The decrease in the I_d/ I_g ratio is an indication of crystallinity and decrease of disorder. Same phenomena were found by Voveidin *et al.* [24] He concluded that such decrease in I_d/ I_g is the development of the graphite fragment or cluster inside the films. But for both a-C and graphite I_d/ I_g ratio is around zero indicating that there is a very little disorder in this two form of carbon [134]. Tuinstra and Koenig [171] did not find a D peak in ideal graphite. If this ideal graphite is now assumed to be more and more disturbed by sp^3 bonded carbon, the D peak will develop and rise in magnitude in the Raman spectrum. When the material is composed entirely of sp^3 bonded carbon (and/or olefinic chains connected by sp^3 bonded carbon) the D peak should not be detected in this model because there exist no benzene clusters that gave rise to the disordered regions which are responsible for the D peak, i.e., in a completely sp^3 network the I_d/ I_g ratio will tend to zero.

Figures 3.32 and 3.33 show I_d/ I_f and I_f/ I_g ratios. High N_2 pressure causes C_{60} content to increase as I_d/ I_f is decreasing. And I_f/ I_g is increasing with N_2 incorporation. This phenomena indicates when N_2 content is low we get more damaged C_{60} and so graphene sheet like structure is attained. Because D, G peaks predominates over the fullerene peak.

But with N_2 incorporation more polymerized C_{60} is formed. Mominuzzaman *et al.* [22] observed the same phenomena by heat treatment of the carbon films using C_{60} as a precursor in PLD process. He observed that the film thickness which was initially around 50 nm, with the increase of temperature height of the micro crystallites increases and roughness of the film increases thereby. And grain sizes increase too from 50 nm to 150 nm with the increase of temperature. So the

modification which is suggested to be some form of polymerization in fullerene films is obtained during growth process that utilizes the ability of pulsed laser deposition method to generate highly energetic particles/species from fullerene C_{60} target in combination with the energy evolved during heating of the substrate. The suggested basic mechanism behind the formation of polymeric C_{60} structures is that intramolecular sp^2 (double) bonds are activated by light exposure and that two such activated bonds on neighboring C_{60} molecules form a chemical connection via two intermolecular sp^3 (single) bonds [170] is very much realizable when the C_{60} targets are ablated by such photons of high energetic excimer pulsed lasers.

So with the increase of N_2 content the carbon films are like the graphene sheet with decreasing disorder. But at high NPP the nitrogen incorporated polymerized C_{60} structure dominates retaining curved graphene structure.

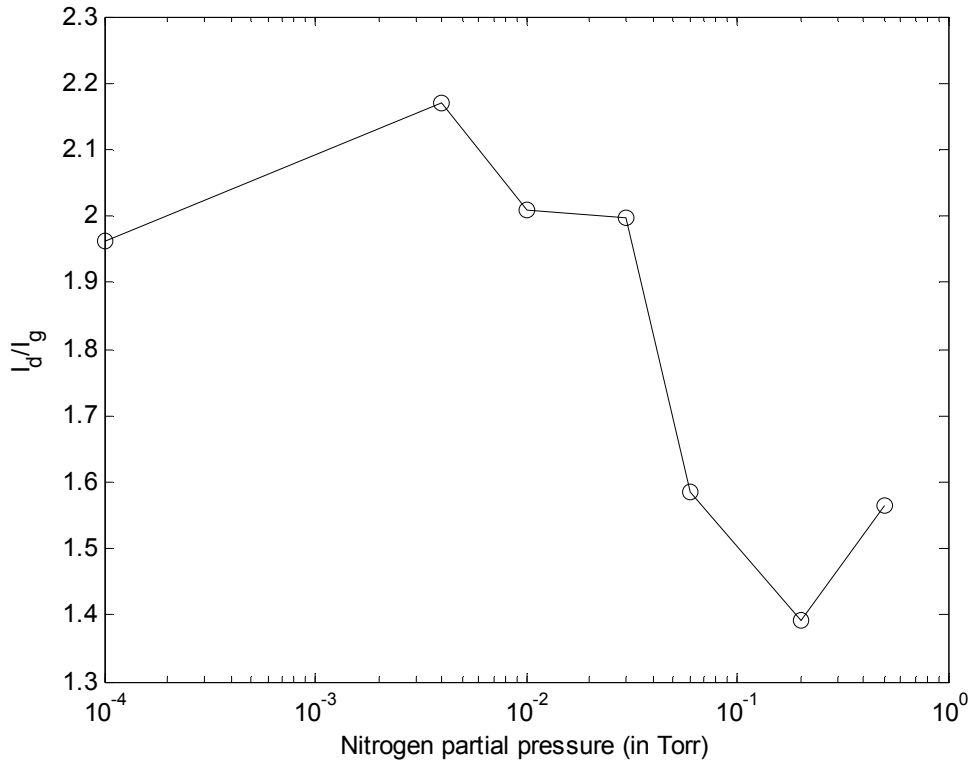

Figure 3.31 Variation of I_d/I_g with different NPP

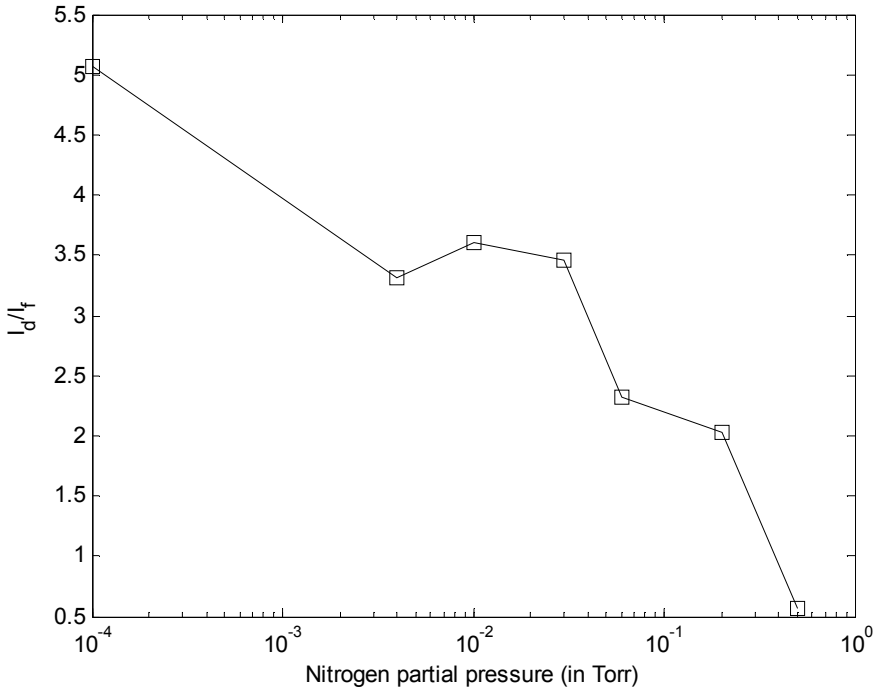

Figure 3.32 I_d/I_f as a function of nitrogen partial pressure

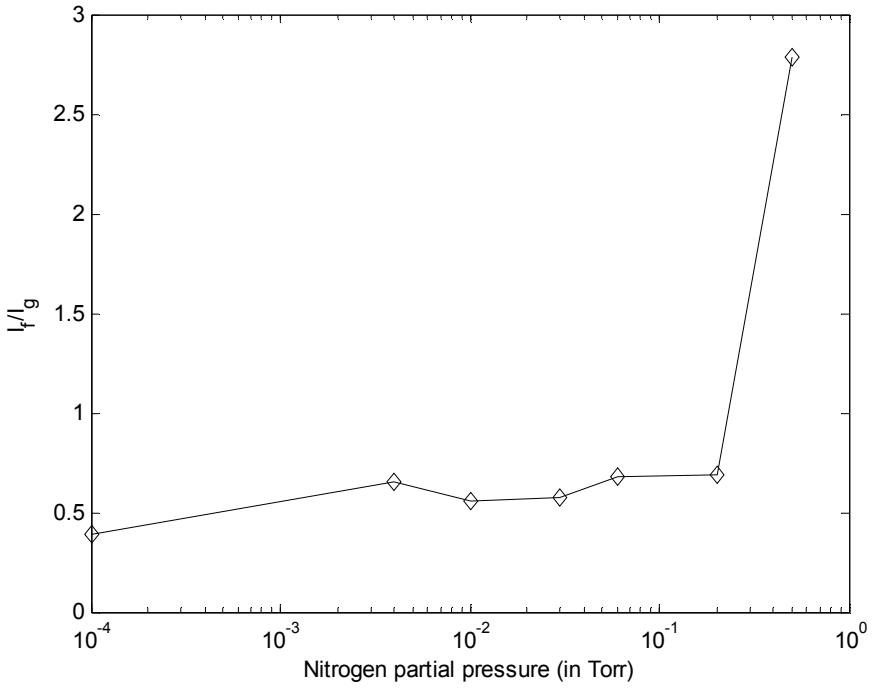

Figure 3.33 I_f/I_g as a function of nitrogen partial pressure

The FWHM variations of the D, F and G peaks as a function of N_2 content are shown in figures 3.34, 3.35 and 3.36 respectively. FWHM denotes full width half maximum point. From the figures we can see that D- FWHM is decreasing, F-FWHM increases and G- FWHM is quite irregular. For G- FWHM we can say that it increase from 88^{-1} to 91 cm^{-1} then attains a saturating value of 84 cm^{-1} and again increases to 90 cm^{-1} and finally decreases to 83 cm^{-1}. According to Ferrari *et al.* [134] G- FWHM is proportional to disorder. This is acceptable with our previous discussion that N_2 incorporation decreases bond angle disorder and increases crystallinity [168].

The same theory is applicable for D- FWHM which is decreasing. But F- FWHM increases continuously from 129.84 cm^{-1} to 219.1 cm^{-1}, which is an indication of polymerization. Polymerization of C_{60} softens the $A_g(2)$ mode and increase the linewidth.

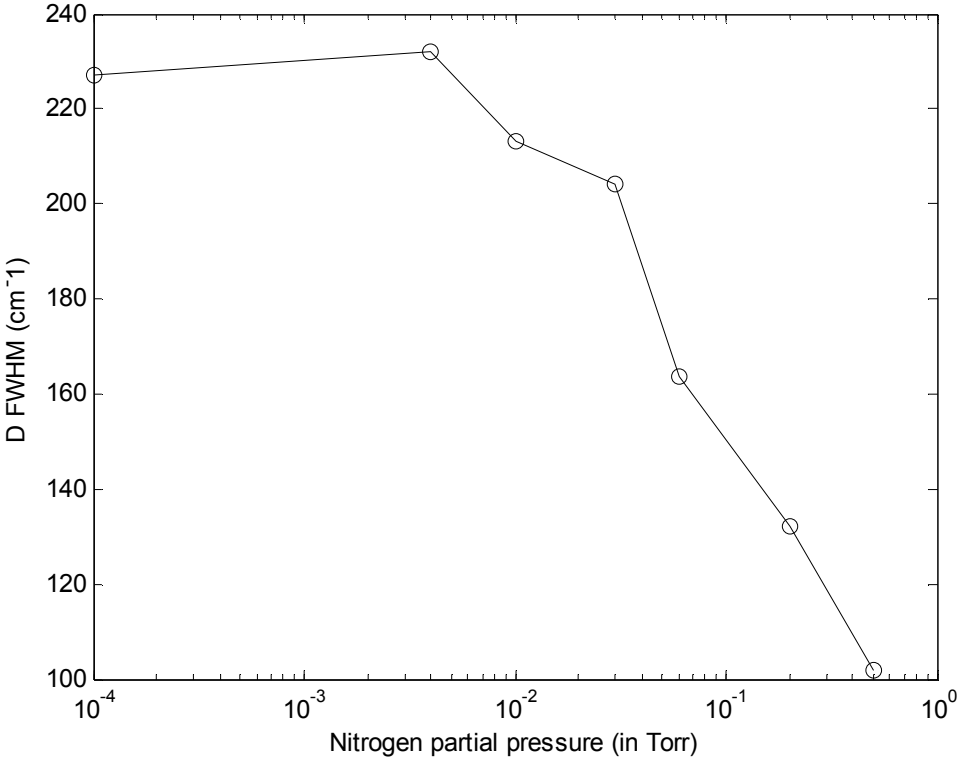

Figure 3.34 FWHM variation of D peak as a function of N_2 content

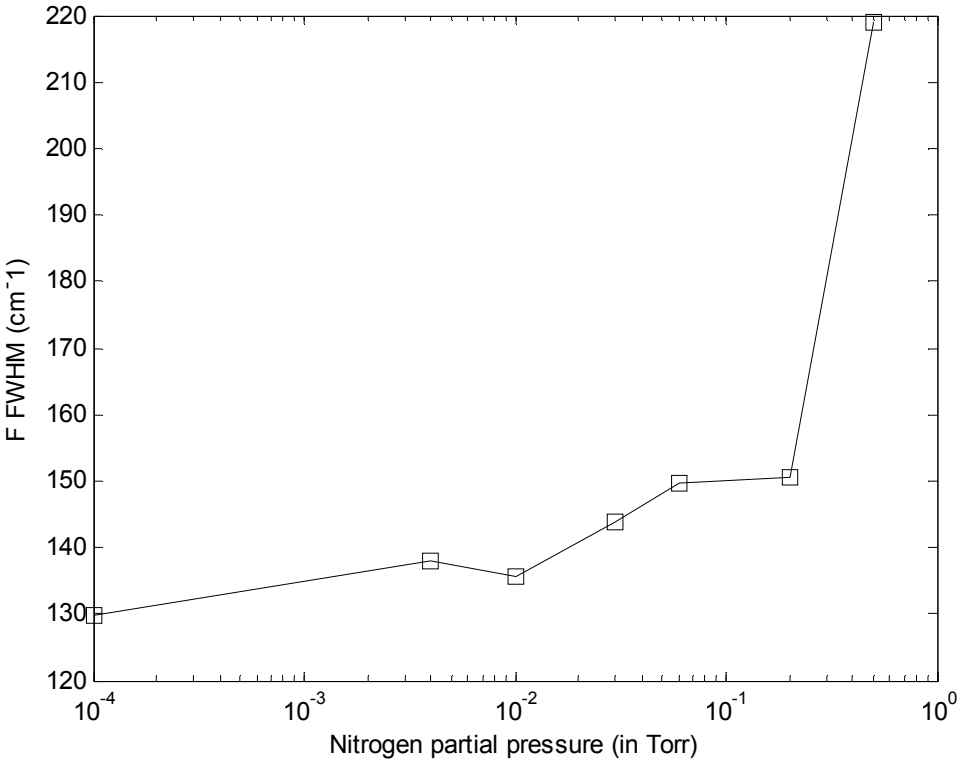

Figure 3.35 FWHM variation of F peak as a function of N_2 content

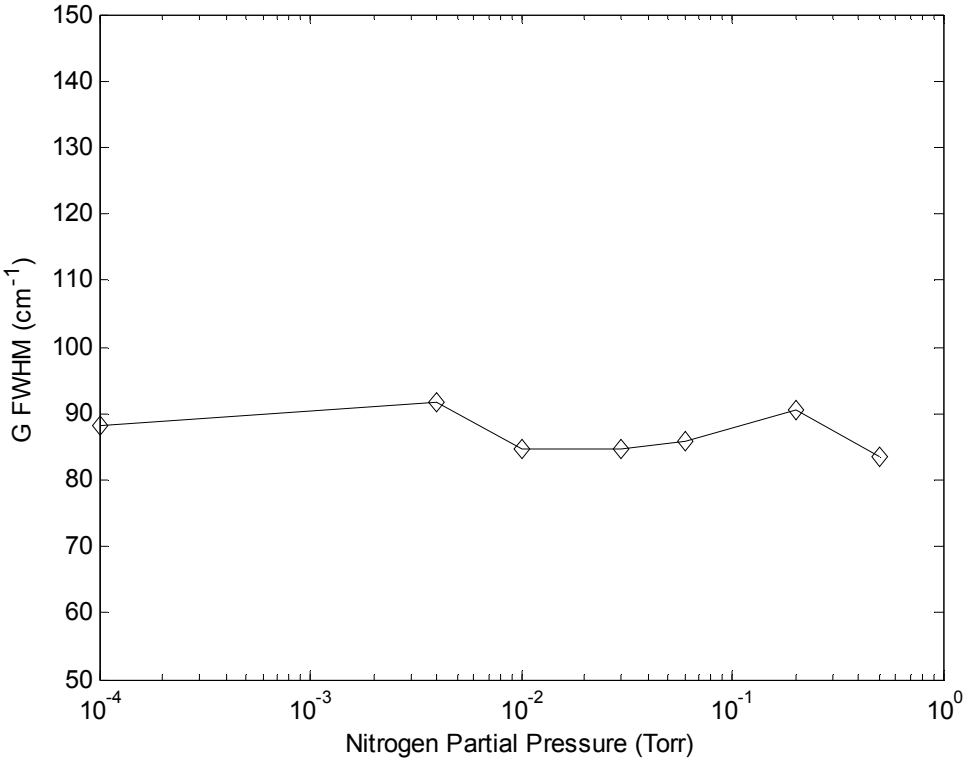

Figure 3.36 FWHM variation of G peak as a function of N_2 content

From the above discussion we can conclude some theoretical aspects. Incident laser energy is 140 mJ and the spot size is 5.5 mm^2. So from this two data we can calculate the fluence rate of 2.55 J/cm^2. Initially when the film is virgin there is no possibility of collision between N_2 and high energetic particles emitted from C_{60} precursor and high energetic pulsed laser. So full energy is used and obviously fluence rate is not disturbed. Therefore complete destruction occurs in the C_{60} which is called damage zone [17]. Disordered carbon films are created due to this high temperature and pressure zone caused by the high energetic excimer laser. This process is equivalent to a transient thermal process. There is a radial profile of temperature surrounding the laser beam path. The maximum damaged part is a cylindrical zone of radius R, where the temperature exceeds the melting temperature of the material for duration of the order of picoseconds. This high temperature is also believed to be sufficient to break the molecular bonds resulting in fragmentation of the bucky balls. The extent of damage and the cross section of this damaged zone depend on the electronic energy loss S_e.

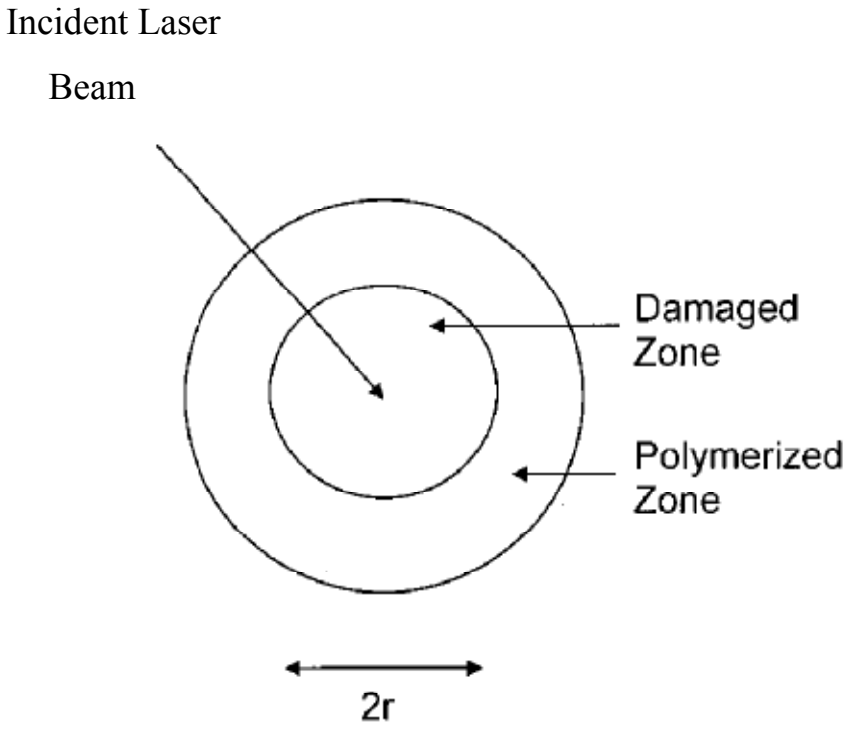

Figure 3.37 Model for the explanation of the experimental results obtained [17].

Initially D, G peaks dominates over the fullerene peak (shifted version). As N_2 pressure is increased there will be some atomic collision and some of the laser pulse may be halted and swiftness or velocity of the laser may be reduced. Consequently incident laser energy is reduced and fluence rate is decreased also. Such low fluence cannot cause overall destruction and localized damage zone occurs. Heat flow around the damaged zone results in structural phase transformations (defects in the crystal structure as well as polymerization, i.e., joining by chemical bond, of two or more bucky balls) around the damaged zone, such as dimerization or polymerization. Moreover particles from C_{60} target will lose energy due to increasing N_2 pressure. This will lessen the film thickness and may help the polymerization process. The principle behind this polymerization is reported by Bajwa *et al.* [17] dimer or polymer created by joining the two or more C_{60} where double bond breaks due to irradiation and hence $A_g(2)$ softens. If N_2 content is more increased then fragmentation decreases and polymerization increases. Zauco *et al.* [21] reported that optimal fluence rate is 25 mJ/cm^2 and optimal irradiation time is about 5 s for irradiation of C_{60} films with UV laser which helps to reduce the formation of other (amorphous) carbon phases during the phototransformation. In his experiment the irradiation process occurs after depositing C_{60} films. But in our works fluence rate is 2.55 J/cm^2. Such high energy is required to irradiate and to deposit the emitted particle due to irradiation. Voevodin *et al.* [24] used graphite precursor in his PLD process and used laser fluence in the range of 5-10 J/cm^2 though he used graphite as a target material to produce fullerene like films.

Zauco *et al.* [21] reported film deposition by sublimation and photopolymerization by irradiation with a pulsed Kr-F laser. This 2 step process i.e. film deposition and then polymerization is a long process and may take 12 h for high quality film conversion [20, 23]. The advantage of depositing carbon films from C_{60} precursor in nitrogen environment by the PLD is that the process is one step and structural modification is performed in the growth process. Here 3 steps are performed at a time i.e. irradiation, film deposition and N_2 incorporation.

3.3 Analysis of Optical Absorption Behavior of Deposited Carbon

Optical absorption behavior is very important for understanding the eligibility of the deposited in electronic device application. The optical absorption behavior is analyzed using the previously experimented reflectance and transmittance data. The reflectance and transmittance spectra of pulsed laser deposited carbon films from C_{60} target are collected for nitrogen partial pressure varied from 0.0001 to 500 mTorr.

Figure 3.38 shows the reflectance spectra and figure 3.39 shows the transmittance spectra of the carbon films for various NPP.

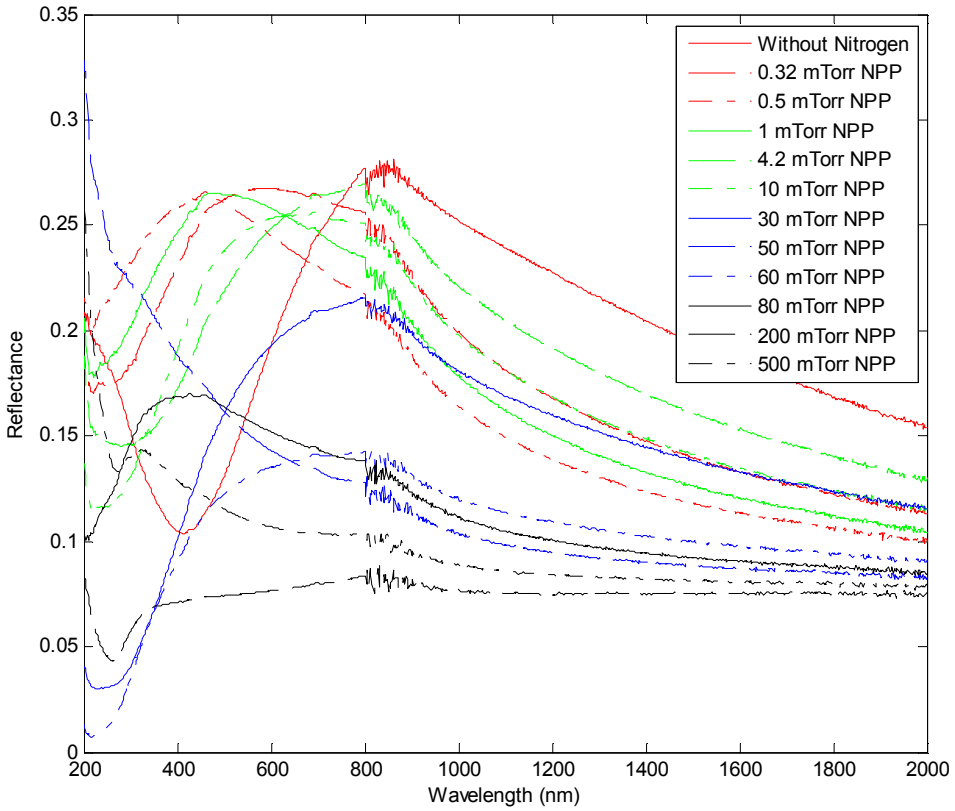

Figure 3.38 Reflectance versus wavelength of incident photon for various NPP

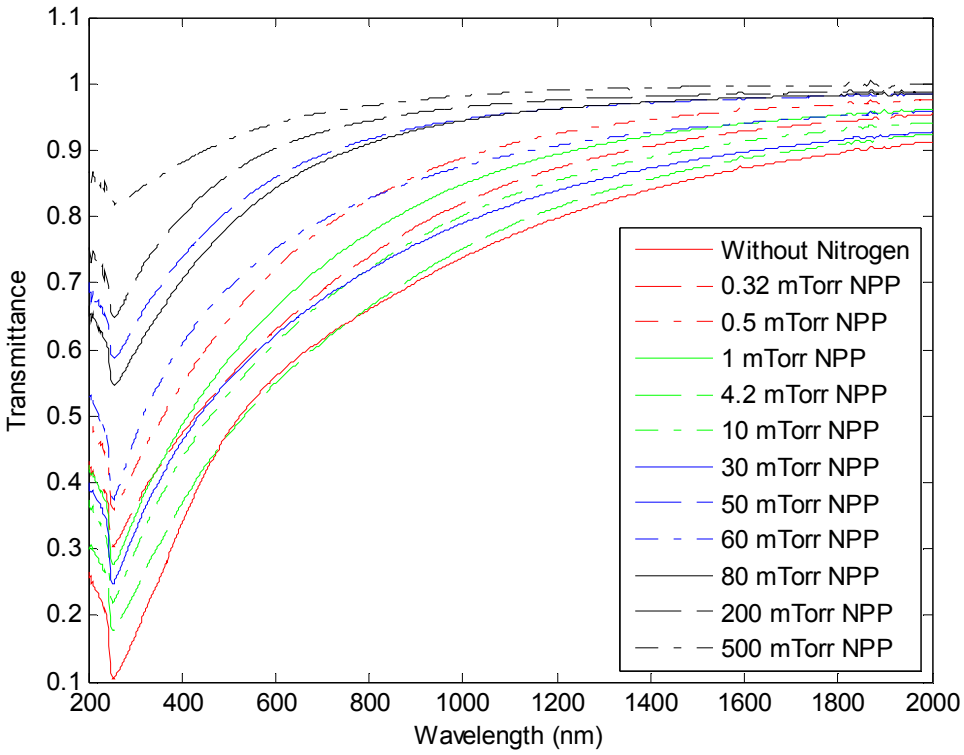

Figure 3.39 Transmittance versus wavelength of incident photon as function of NPP

The absorption coefficient α is determined by using relation given in equation 3.1

$$\alpha = \frac{1}{d} \, ln \frac{(1-R)^2}{T} \tag{3.1}$$

where, T is the optical transmittance , R is the optical reflectance and d is the thickness of the film.

Form the calculated α, the absorption constant or extinction coefficient k is determined by using the equation 2.16. The variation of extinction coefficient (k) with photon energy (hν) is shown in figure 3.38. Here ν is the frequency of the incident light. It is seen from the plot that with the increase in photon energy, the value of k increases. This happens as for a fixed mobility gap, with the increase in photon energy, the probability of electron transfer across the mobility gap rises with photon energy. At high photon energies, extinction coefficient becomes increasingly independent of photon energy.

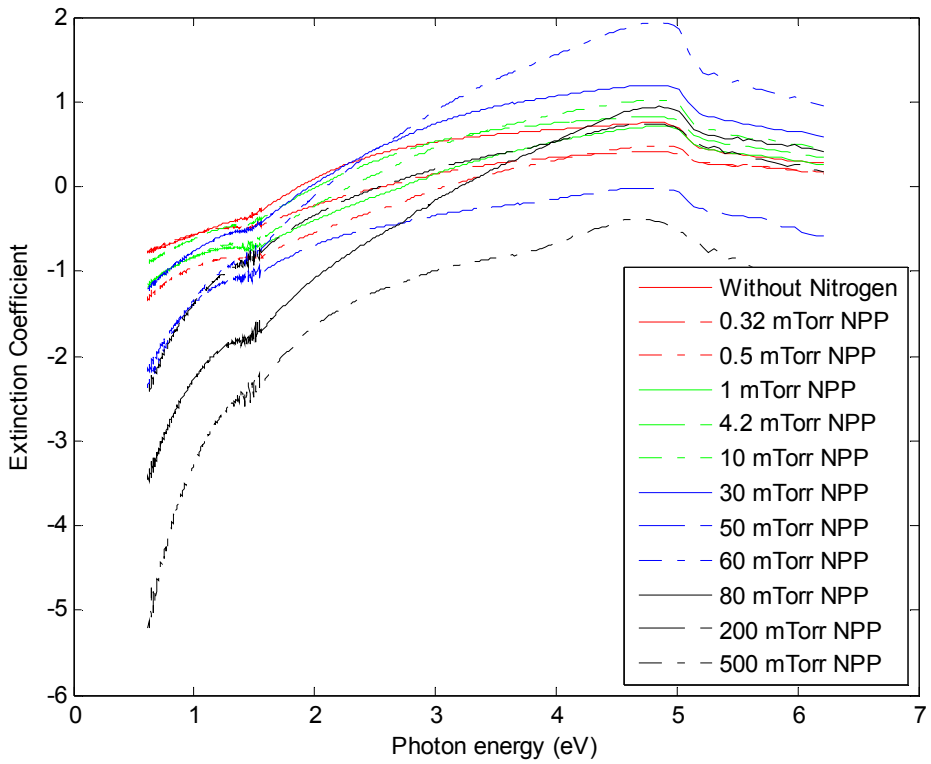

Figure 3.40 Variation of extinction coefficient with photon energy for different NPP

Then using the values of calculated absorption coefficient, α and the frequency of the incident light, $(\alpha h\nu)^{1/2}$ is plotted as a function of photon energy hν. The optical gap of the deposited carboneous films is obtained from the extrapolation of linear part of the curve, $(\alpha h\nu)^{1/2}$ vs $h\nu$ at the absorption coefficient α = 0, using the equation 3.2 below.

$$(\alpha h\nu)^{1/2} = B(h\nu - E_g) \tag{3.2}$$

Where, B is the Tauc parameter.

The figure 3.41 shows the plots of the $(\alpha h\nu)^{1/2}$ vs $h\nu$ of the carbon films in nitrogen free environment, 0.32 mTorr, 0.5 mTorr, 1mTorr, 4.2 mTorr, 10 mTorr, 30 mTorr, 50 mTorr, 60 mTorr, 80 mTorr, 200 mTorr, 500 mTorr NPP.

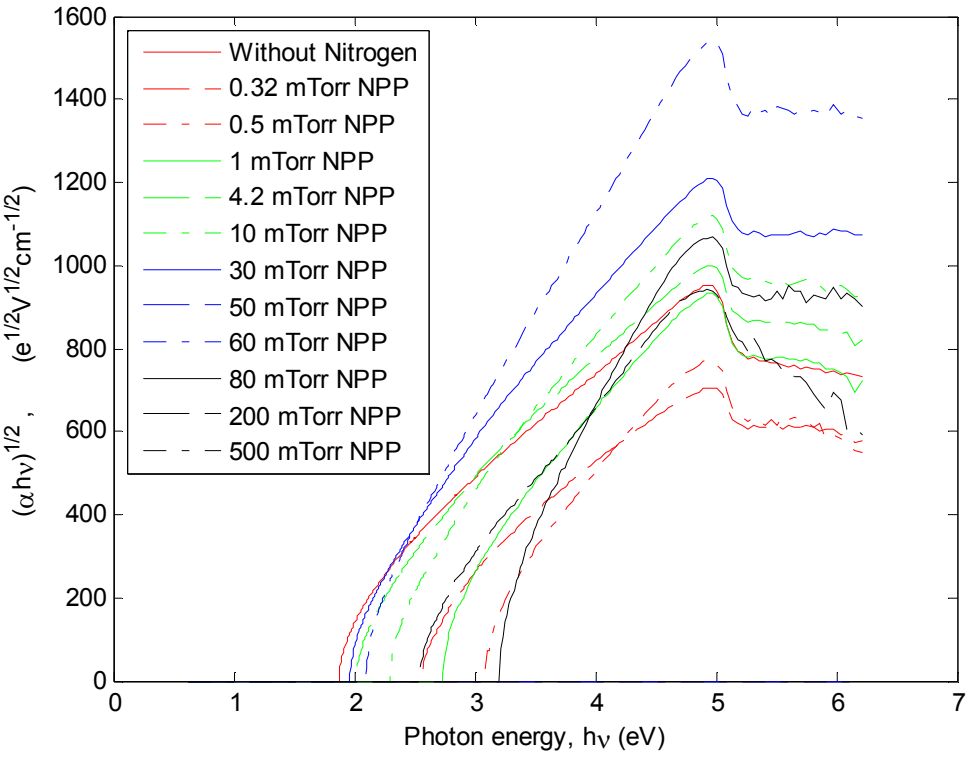

Figure 3.41 $(\alpha h\nu)^{1/2}$ versus photon energy for different NPP

The values of the optical gap of carboneous films that are calculated form the $(\alpha h\nu)^{1/2}$ vs $h\nu$ for different NPP with extrapolation of the linear part of the curve is shown in the table 3.3. Figure 3.42 shows the optical gap of deposited carbon films for different nitrogen partial pressure (NPP).

It is found from the calculated value of the optical gap for deposited film in nitrogen free environment is 0.9833. From the optical absorption behavior analyses results it is obtained that the optical gap initially increases with NPP up to .5 mTorr. After that optical gap for the deposited films decline for NPP of 4.2 mTorr. Then again, optical gap is increases upto 80 mTorr. And after that it decreases with increase in NPP.

Table 3.3 Values of the optical gap for different NPP

NPP	**Optical Gap, Eg (eV)**
Nitrogen Free	0.9833
0.32 mTorr	1.592
0.5 mTorr	2.528
1 mTorr	2.06
10 mTorr	1.545
30 mTorr	1.171
50 mTorr	1.5
60 mTorr	1.662
80 mTorr	2.786
200 mTorr	2.201
500 mTorr	2.1

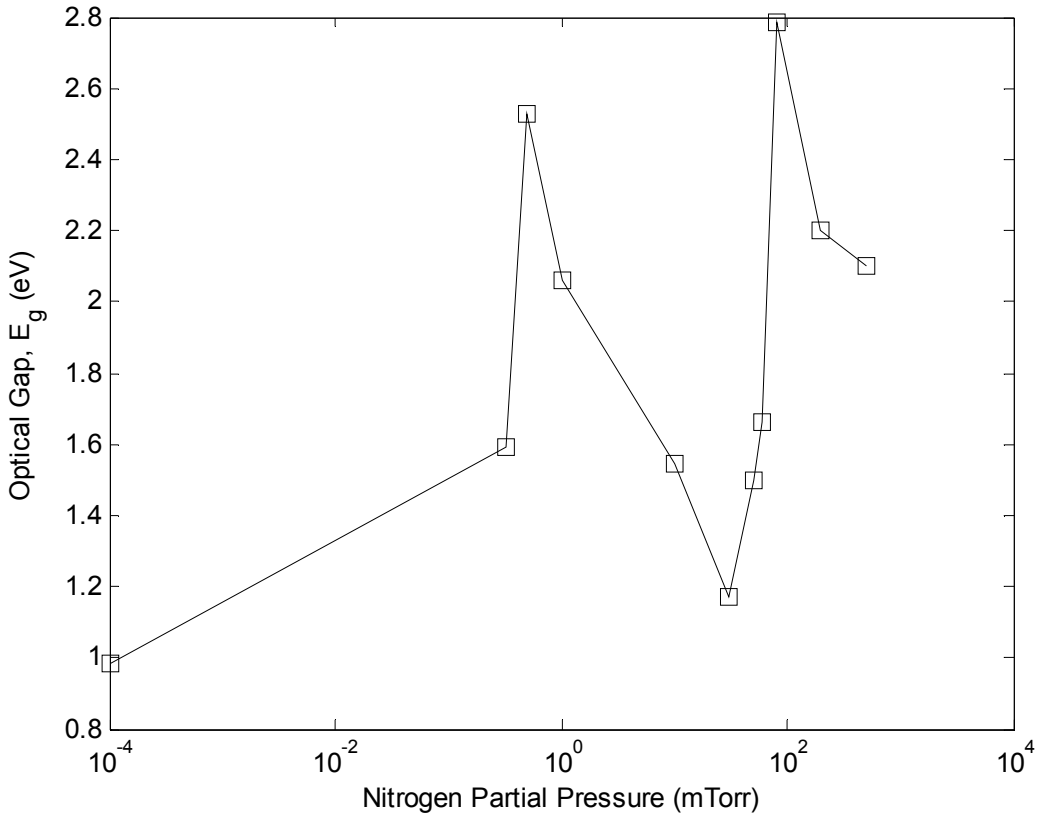

Figure 3.42 Variation of optical gap as a function of NPP in the PLD chamber

The processes that control the behavior of the gap states in non-crystalline semiconductors are structural disorder responsible for the tail states and structural defects in deep states. The Tauc parameter, B, is a measure of the steepness of the band tail (Urbach region) density of states is calculated from the optical absorption behavior of different NPP. The Tauc parameter, B, can be obtained from slope of the straight line fitted for the linear part of the curve $(\alpha h\nu)^{1/2}$ vs $h\nu$. The measured values of the B are shown in the table 3.4 for different NPP.

Table 3.4 Values of Tauc Parameter, B for different NPP

NPP	Tauc Parameter, B ($cm^{-1/2}e^{1/2}V^{1/2}$)
Nitrogen Free	240
0.32 mTorr	220
0.5 mTorr	330
1 mTorr	330
10 mTorr	340
30 mTorr	330
50 mTorr	400
60 mTorr	480
80 mTorr	540
200 mTorr	360
500 mTorr	330

The Tauc parameter increases with increasing NPP up to 80 mTorr. Then it decreases as the NPP increases. The higher value of Tauc parameter indicates less disorder. So it can be concluded that with increase of NPP disorder in the deposited carboneous films have less disorder. In high NPP decline in Tauc parameter may be due to the structural change of the deposited films. Figure 3.43 shows the Tauc parameter versus NPP of the deposited films.

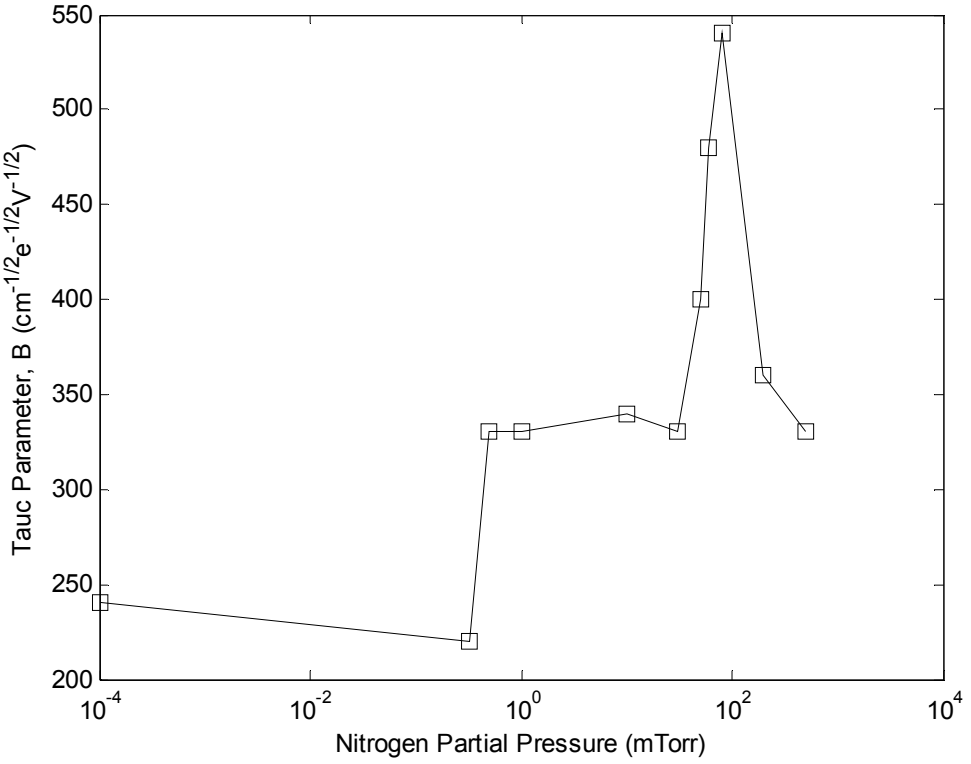

Figure 3.43 Variation of Tauc Parameter as a function of NPP of the deposited films

The width of the optical absorption edge, the Urbach energy E_U, declines with increasing NPP up to 80 mTorr. Then E_U increases with increasing NPP. The Urbach energy is a measure of the disorder of the atomic network. The decrease E_U suggests that the disorder of a: C:N may reduce with addition of N_2 up to certain NPP.

The thesis entitled **"Raman Spectra and Optical Absorption Analyses of Carboneous Films Deposited from C_{60} in Nitrogen Environment by Pulsed Laser Deposition"** submitted by Ahmed Zubair, Roll on: 0409062226P has been accepted as satisfactory in partial fulfillment of the requirement for the degree of MASTER OF SCIENCE IN ELECTRICAL AND ELECTRONIC ENGINEERING on October 18, 2011.

BOARD OF EXAMINERS

1. _____

Dr. Sharif Mohammad Mominuzzaman — **Chairman**
Professor — (Supervisor)
Department of Electrical and Electronic Engineering
Bangladesh University of Engineering and Technology,
Dhaka-1000, Bangladesh

2. _____

Dr. Md. Saifur Rahman — **Member**
Professor — (Ex-Officio)
Department of Electrical and Electronic Engineering
Bangladesh University of Engineering and Technology,
Dhaka-1000, Bangladesh

3. _____

Dr. Mohammad Jahangir Alam — **Member**
Professor
Department of Electrical and Electronic Engineering
Bangladesh University of Engineering and Technology,
Dhaka-1000, Bangladesh

4. _____

Dr. Md. Anwarul Abedin — **Member**
Associate Professor — (External)
Department of Electrical and Electronic Engineering
Dhaka University of Engineering and Technology,
Gazipur-1700, Bangladesh

3.4 Correlation between the Raman Spectra and Optical Absorption Behavior of the Deposited Carbon Films

The Raman spectra are deconvoluted here with the help of curve fitting technique. The deconvolution outcome is 3 different bands named D peak, F peak and G peak. A detail analysis of these deconvoluted peaks is presented in this work. G peak variation is proportional to disorder and is increases with amorphousness of Carbon. G peak (1580 ± 5 cm^{-1}) is the characteristic peak of single crystalline graphite. The actual position of D peak for graphite is 1360 cm^{-1}. The down shifting of D peak indicates the presence of sp^3 C. The second peak, which is named F peak, evolutes due to presence of C_{60} structure. This peak shifts from the original position and its spectrum is quite broad in nature maybe because the breaking of the sp^2 bond in the pentagonal and hexagonal rings of the C_{60} and hence softening of the $A_g(2)$ mode of the C_{60} .

FWHM of the D and G peak is decreasing with increasing NPP, which is an indication of less disorder. In the higher NPP, the decrease in the F line position and increasing nature of F- FWHM indicate the nature of the film has changed. I_d/ I_g ratio finally decreases for highest N_2 content and has a value of 1.5634. The decreasing nature indicates the development of the graphite sheet like films. The other two ratios I_d/ I_f and I_f/ I_g represents the increasing feature of the structural change in the semiconducting carbon. Where initially D and G peaks dominate over the fullerene peak later with the incorporation of N_2 these two peaks decreases with respect to fullerene peak. That's why I_d/ I_g ratio is decreasing and I_d/ I_f is decreasing and I_f/ I_g is increasing.

At lower NPP the nitrogen is passivating the disorders in the carbon network and thus band tail states are filled by nitrogen. So, initially the optical gap decreases as the NPP increases. Raman spectra analyses also agree with this incident. Then as NPP increases more nitrogen than act as a doping atom in the carbon network creates donor states in the forbidden gap of the carbon films. And hence decrease in the optical gap. As the decrease of D peak position in the Raman Spectra indicates the presence of sp^3 bond, it can be concluded that the nitrogen breaks the sp^2 bond of the graphitic structure and from sp^3 bond with carbon.

From optical absorption behavior it is found that Tauc parameter, B is increasing with NPP which indicates that steep band edge resulting from less disorder which agrees with the results from Raman spectra analyses. At the higher NPP, B decreases with NPP, which may be due to a structural change in the carbon films at NPP greater than 80 mTorr. Again, at higher NPP from Raman spectra it is found that that I_d/ I_f become very large compared to lower NPP that maybe due to drastic change in the films. And all three peaks are present in the fitted Raman spectra at high NPP. From optical gap, E_g found from optical absorption analysis also shows that at higher NPP E_g different from lower NPP. So, it can be concluded that the structure of the film is like graphitic sheet that retains the behavior of C_{60} at high NPP.

The figure 3.43 shows the variation of Tauc parameter, B, FWHM of D peak and I_d/I_g as a function of NPP. The increasing value of B indicates the decrease of disorder in the films. I_d/I_g is decreasing with increasing NPP, which is an indication of decrease in disorder. So the results found from Raman spectra analysis agree with the outcome of the absorption behavior study.

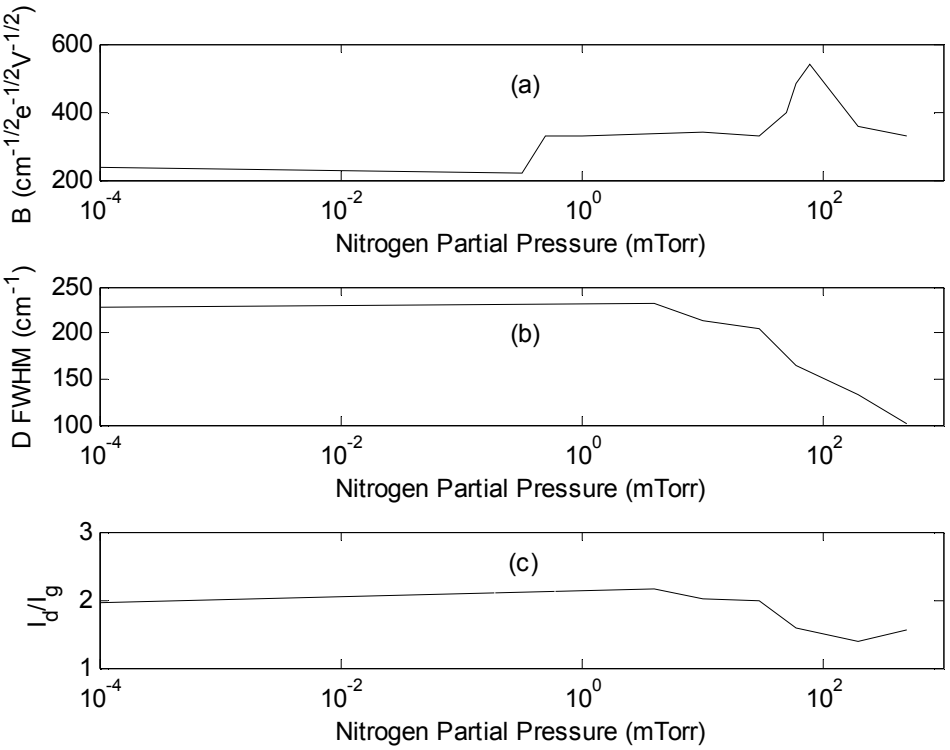

Figure 3.44 (a) Variation of Tauc parameter, B, (b) Variation of FWHM of D peak and (c) Variation of I_d/I_g as a function of N_2 content

The carbon films deposited at high NPP shows the presence of more C_{60} structure. This actuality can be understood from the drastic increase of I_f/I_g and decrease of I_d/I_f. Figure 3.45 shows the as function of NPP. If the Tauc parameter, B is correlated with I_f/I_g , it is apparent that at high NPP, B decreases which is a sign of disorder. So this can be concluded that at high NPP polymerized C_{60} is present though quality of film decreases.

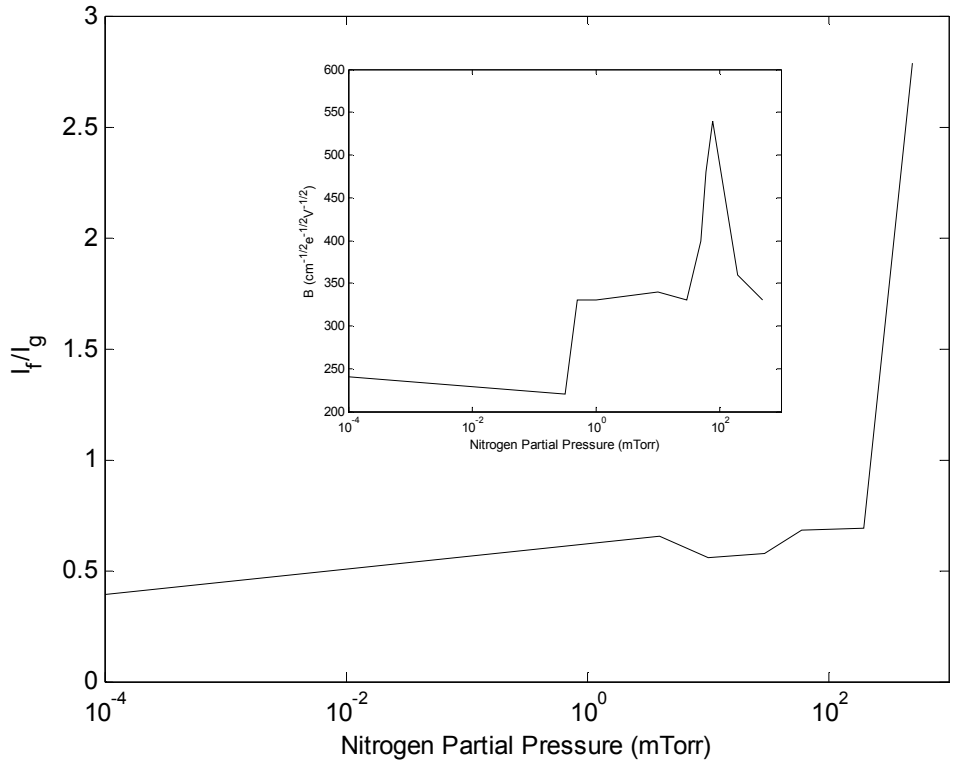

Figure 3.45 I_f/I_g plotted as a function of NPP. The inset shows the B as a function of NPP

It can be obtained from the correlation of analyses of optical absorption and Raman spectra, at lower NPP the carbon films are like graphene sheet like structure with disorder decreasing with increasing NPP. And at higher NPP, sp^2 bonds of pentagonal and hexagonal rings breaks and bonds with nitrogen and other C_{60} to form a graphite sheet that have the behavior of C_{60} but quality degrades.

3.5 Current Density versus Voltage (J-V) Characteristics

The current density(J) versus voltage(V) for heterojunction that is consisted of the carboneous films from the C_{60} target deposited on the p-Si is analyzed for different important parameterof the heterojunction device.

The figure 3.46 shows the current density versus voltage (J-V) characteristics for the n-C/p-Si heterojunction, where carbon film is deposited from the target C_{60} in varying nitrogen partial pressure environment. The J-V characteristics for the heterojunction shows typical diode J-V characteristics.

The diode quality factor calculated from the plot of ln(J) vs V is shown in table 3. 5. It can be seen from the table that the heterostructure have quality factor between 1 and 2, which indicates that the current in the junction is diffusion and recombination

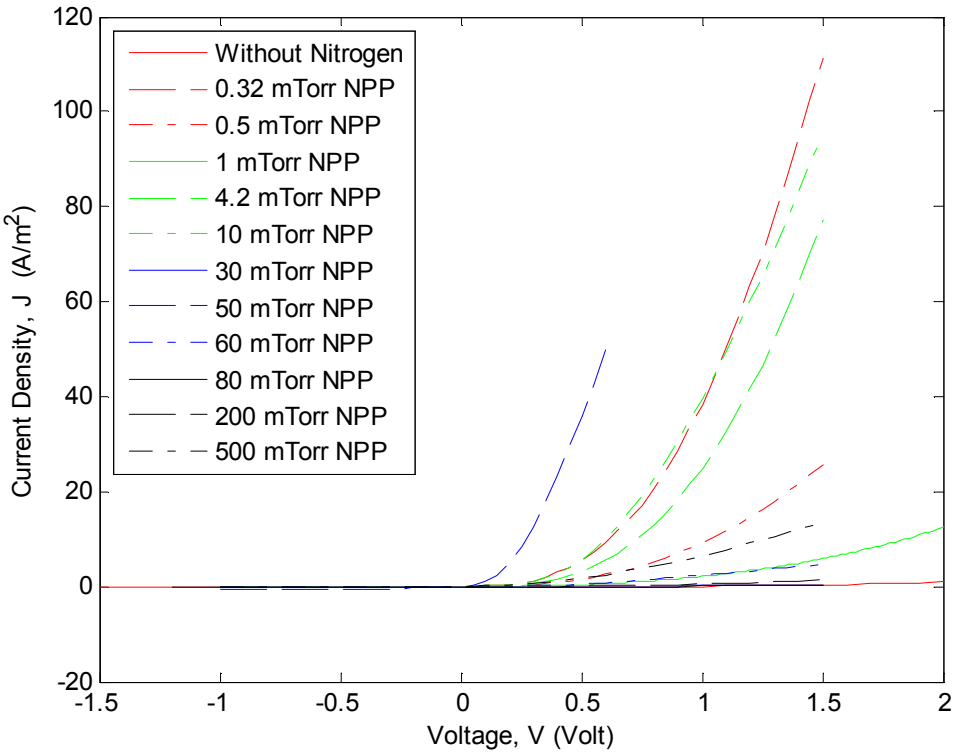

Figure 3.46 Current Density-Voltage characteristics for the heterojunction for the films deposited from C_{60} precursor for different NPP

limited. At higher voltage quality factor of the diode increases due to the series resistance effect of the junction. The nature of the current flowing in different region of current-voltage characteristics for a practical Si diode is described in chapter 2.

Table 3.5 Calculated diode quality factor from ln(J) vs V characteristics

NPP	Quality Factor, η
Nitrogen Free	2.76
0.32 mTorr	1.75
0.5 mTorr	1.65
1 mTorr	1.41
10 mTorr	1.52
30 mTorr	2.00
50 mTorr	2.00
60 mTorr	2.11
80 mTorr	2.24
200 mTorr	2.50
500 mTorr	2.53

It has been seen that the value of the electron mobility in the carbon thin film is always less than 1 cm^2/V-sec. Due to amorphous nature of the carbon thin films the value of the electron mobility is found to be very small. The reverse saturation current densities of the deposited films are obtained from the J-V characteristics.

From the table 3.5 it can be seen that the doping concentration is increasing with the increasing NPP. Then doping concentration decreases with increasing NPP. At higher NPP doping concentration again increases. From the figure 3.54 J-V characteristics improves up to 10mTorr NPP. The best performance J-V is found in the 10mTorr NPP. Then the J-V characteristics decline for increasing NPP. The reverse saturation current also shows similar behavior. So it can be concluded that up to certain NPP the characteristics of the films improves and then the quality of the film for device application decreases. From the Raman spectra and the optical absorption behavior similar results are found i.e. with NPP increase disorder decreases and at high NPP drastic structural modification occurs.

3.6 Comparison of Deposited Carbon Films Deposited with those from Graphite and Camphor Precursor

In this chapter Raman analysis as well as optical absorption behavior of the carbon films from C_{60} precursor is compared with those of the films produced from graphite and camphor ($C_{10}H_{16}O$) targets deposited in the similar conditions. This study is necessary to understand whether the characteristics of the carbon films are improved and to outline the scope of electronic device application of the deposited thin films.

Figure 3.47 shows the Raman spectra of the carbon films from fullerene, graphite and camphor precursor. Figure 3.48, 3.49, 3.50 shows the fitted Raman spectra of the carboneous films deposited using graphite, camphor and fullerene (C_{60}) as target materials.

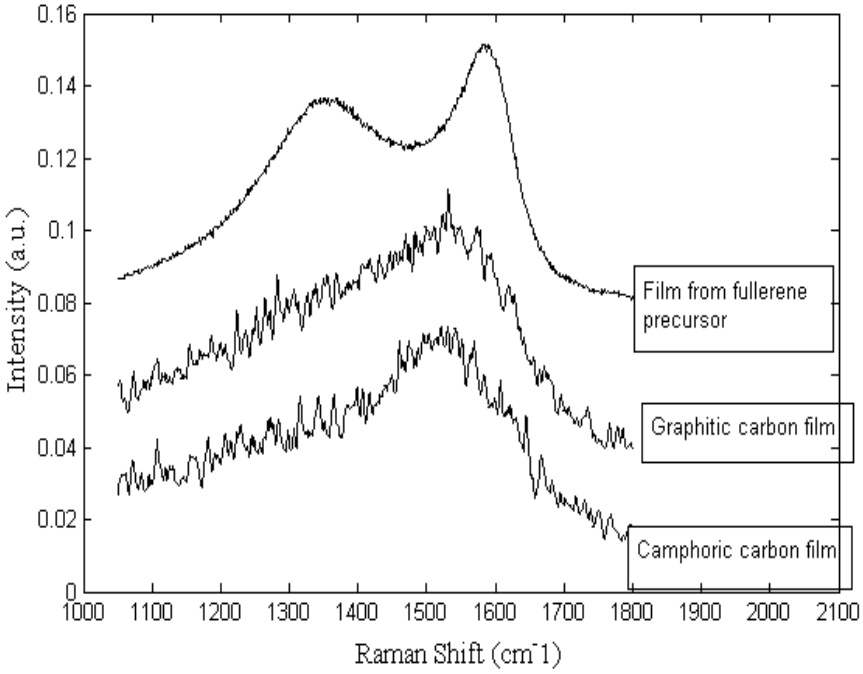

Figure 3.47 Raman spectra of deposited carbon films

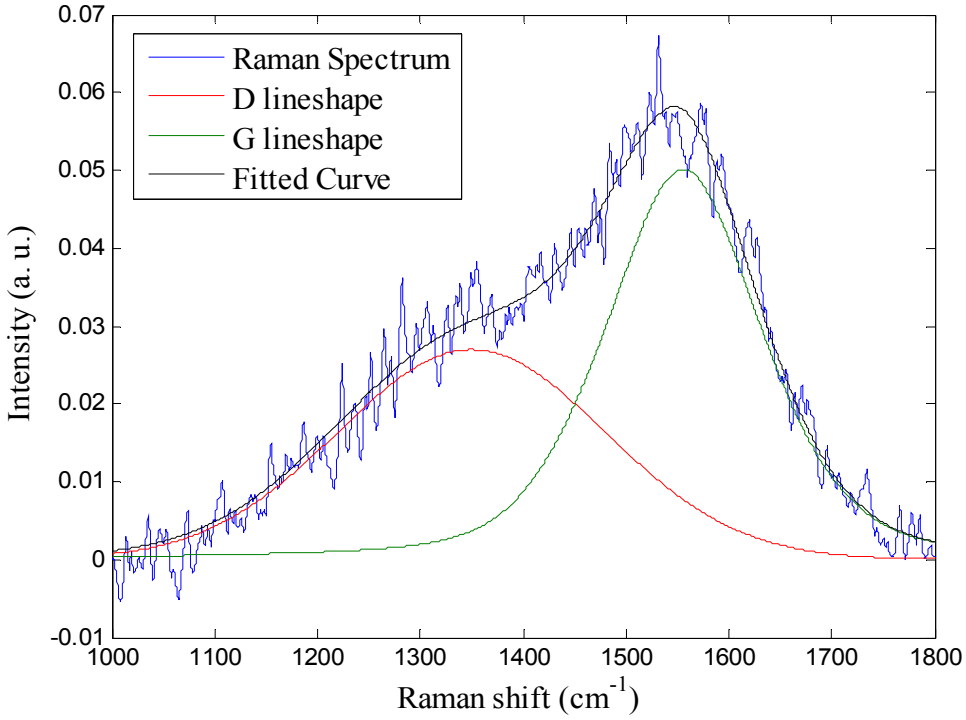

Figure 3.48 Fitted Raman spectrum of the carbon film deposited using graphite as target materials

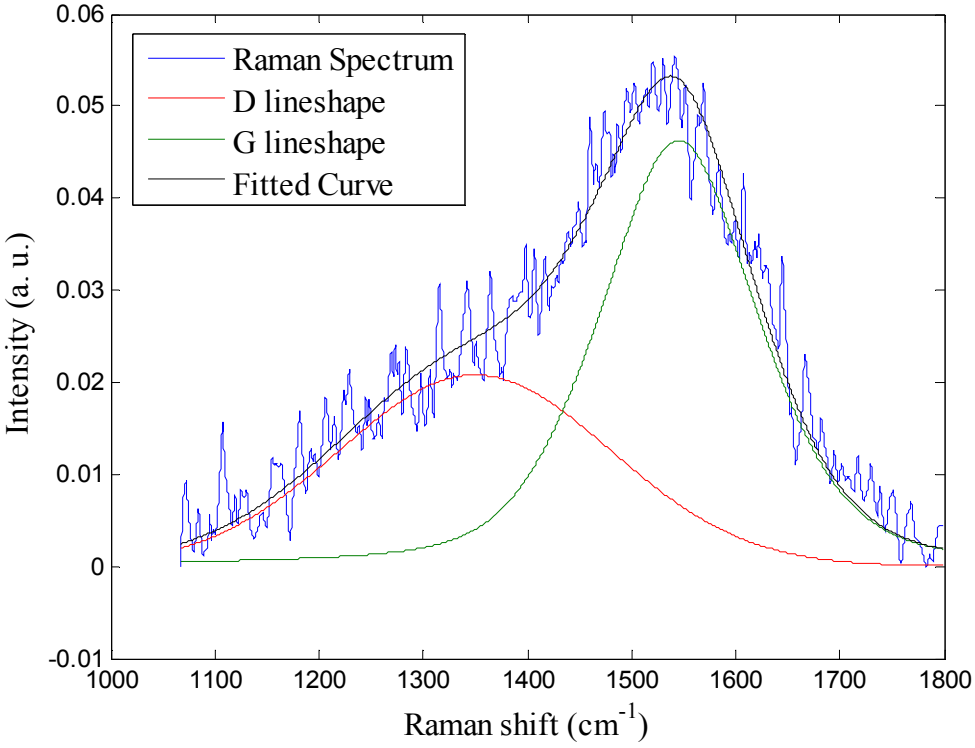

Figure 3.49 Fitted Raman spectrum of the carbon film deposited using camphor as target materials

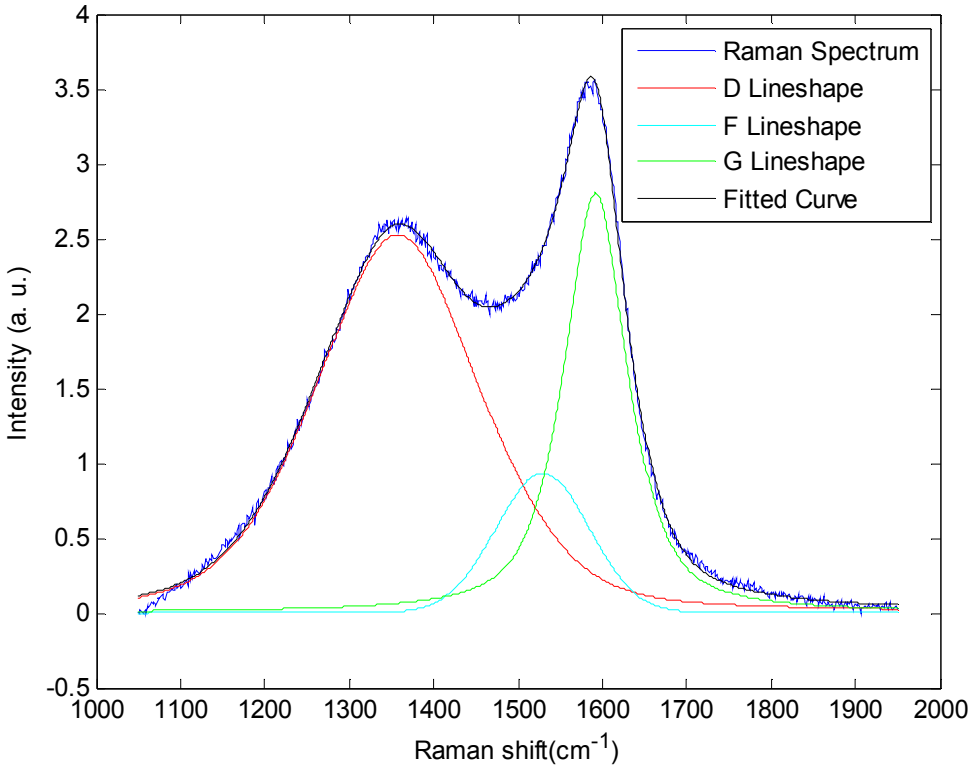

Figure 3.50 Raman spectrum of the carbon film deposited using C_{60} as precursor fitted with three peaks

Table 3.6 shows the different parameters obtained by fitting Raman spectra of the carbon films. G line deviation from its original position is proportional to disorder and increases with amorphousness of carbon. G line position of Camphoric carbon (CC), Graphitic carbon (GC) and Fullerene film are 1545, 1550, 1592.1 cm^{-1}. G line deviation which is proportional to disorder is much greater for CC film and GC film compared to fullerene film. This indicates that there is little disorder in fullerene film than CC or GC film. The D line positions for the 3 films are close to each other and also close to the original D line position. Less FWHM is an indication of better crystallinity. D-FWHM is lower in CC film indicating that it has lesser disorder than GC film. D FWHM of fullerene film is very low compared to that for CC or GC film and this indicates that quality of the film is improved substantially. G FWHM proves this statement more strongly because its value for fullerene film is almost halved. This low value of G-FWHM also proves that the film produced from C_{60} precursor retains more graphene sheet like structure. Figure 3.51 and 3.52 shows the comparison of D peak position, G peak position, D FWHM and G FWHM for the carbon films.

So it can be concluded from the Raman spectra analysis that C_{60} can be used as a better target material to obtain semiconducting carbon films for electronics applications by physical vapor deposition techniques instead of graphite or camphor for semiconducting/optoelectronic applications.

Table 3.6 Raman Fitting Parameters of graphitic, camphoric and C_{60} carbon films

Samples	**Graphitic Carbon Film**	**Camphoric Carbon Film**	**C_{60} carbon film**
D position (cm^{-1})	1364	1356	1357.4
G position (cm^{-1})	1550	1545	1592.1
F position (cm^{-1})			1529.3
D FWHM (cm^{-1})	444	388	227.2
G FWHM (cm^{-1})	225	175	88.1
F FWHM (cm^{-1})			129.8
I_D/I_G	2.1	1.2	1.96

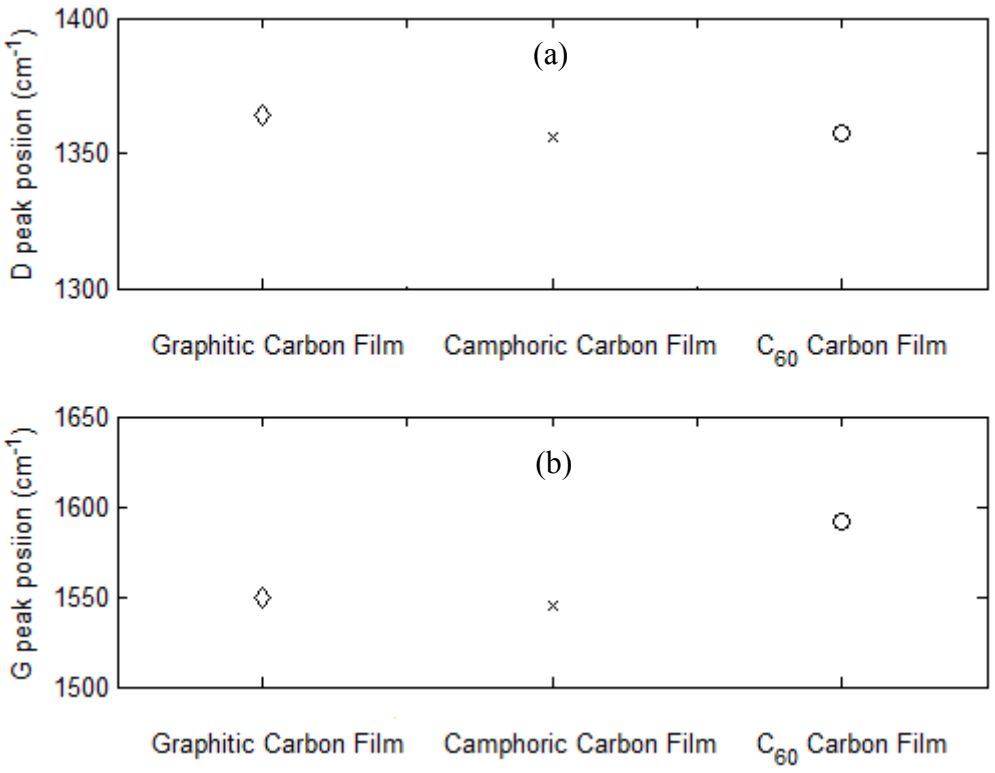

Figure 3.51 Comparisons of (a) D and (b) G peak position of graphitic, camphoric and C_{60} carbon films

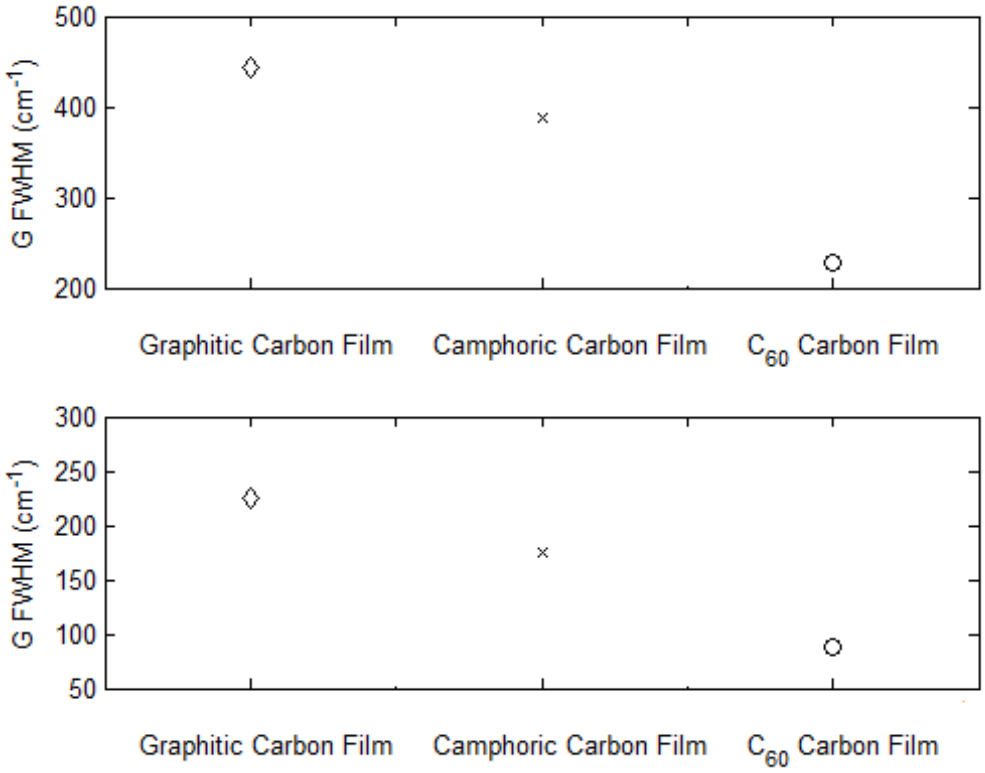

Figure 3.52 Comparisons of (a) D and (b) G FWHM of graphitic, camphoric and C_{60} carbon films

Nitrogen doped n-type amorphous carbon (n-C:N) films were deposited by a pulsed laser deposition technique at room temperature using a camphoric carbon target with different nitrogen partial pressures (NP) in the range from 0.1 to 800 mTorr by Mominuzzaman *at el*. The Tauc relationship [173] was used to evaluate the optical band gap (E_g). The Tauc optical gap was plotted as a function of NP, as shown in figure 3.53(a). The optical gap of the films is within the range of 0.70 to 0.95 eV. This optical gap range is not suitable for optoelectronic application.

The optical gap of the carbon films from C_{60} precursor are greater and in the range of 1~2.5 eV which is suitable for optoelectronic application. Again Tauc parameter of these films is better than the films of camphoric carbon.

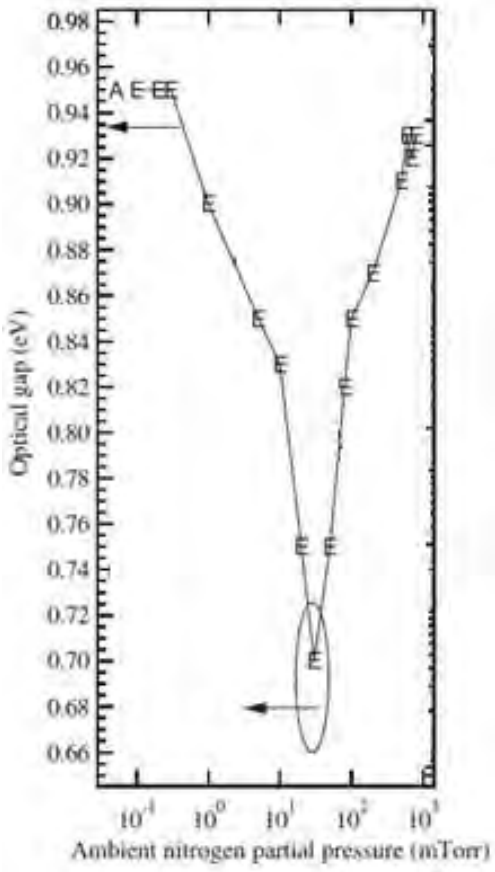

Figure 3.53 (a) Optical gap (Eg) for n-C:N films deposited in various ambient nitrogen partial pressures

The current density(J) versus voltage(V) characteristics for heterojunction that is consisted of the carboneous films from the C_{60} target deposited on the p-Si are illustrated in figure 3.46. From the J-V characteristics of the carbon films from camphoric target it is obtained that the current density is maximum ~9 mA/cm^{-2} at 0.4V. But from figure 3.46 the current density is maximum ~ 35 mA/cm^{-2} at 0.4 V. So there is fourfold improvement in the J-V characteristics.

High energetic pulsed laser causes semiconducting film from C_{60} target which retains crystalline graphene like structure. From the comparison between the carbon films it can be concluded that such improved quality of film proves that C_{60} can be used as a better target material instead of graphite or camphor for semiconducting or optoelectronic applications.

3.7 Modeling of Raman Peaks with Gaussian and Lorentzian Line Shape

The Raman Spectra of the carboneous films are analyzed in chapter 3.2. The Raman spectra are fitted with three peaks. The line shape of the peaks is combination of Gaussian and Lorentzian line shape. In this chapter the analyzed data is used to model the line shape of each three peaks as a function of NPP.

The G and D peaks are fitted quadratic equation as the function of the NPP. From the appendix II's Gaussian percentage table it can be seen that the F peak is almost 100% Gaussian.

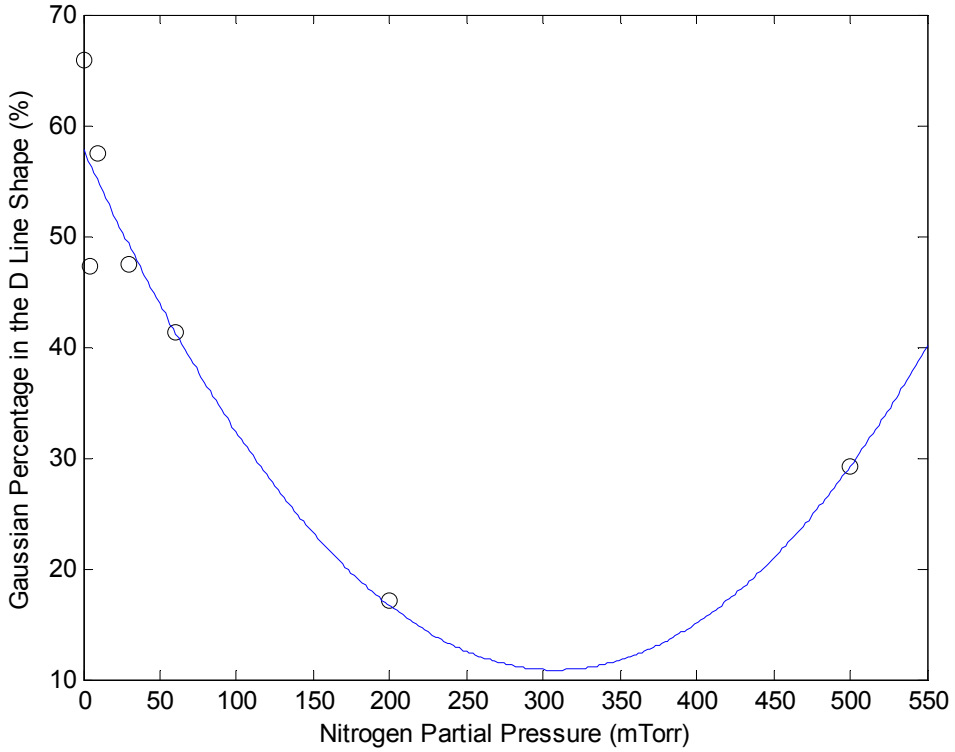

Figure 3.54 Quadratic fit of Gaussian line shape in the D peak

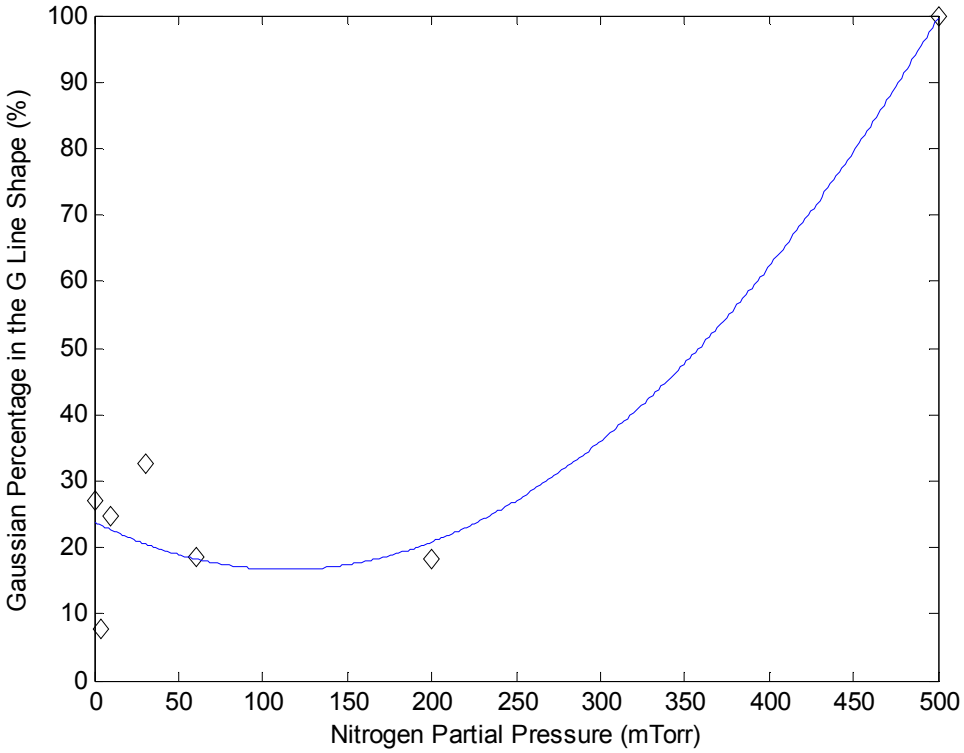

Figure 3.55 Quadratic fit of Gaussian line shape in the D peak

From the quadratic fit of the Gaussian percentage data, the following relation can be found:

$$G_D = 0.58 - 0.0031\, x_{NPP} + 5 \times 10^{-6}\, x_{NPP}$$

$$G_G = 0.24 - 0.0013\, x_{NPP} + 5.6 \times 10^{-6}\, x_{NPP}$$

where,

G_D = Gaussian percentage in the D line shape

G_G = Gaussian percentage in the G line shape

x_{NPP} = Nitrogen Partial Pressure (NPP)

From the modeling of the both D and G peak it can be found that in the higher NPP the peaks have more Gaussian percentage.

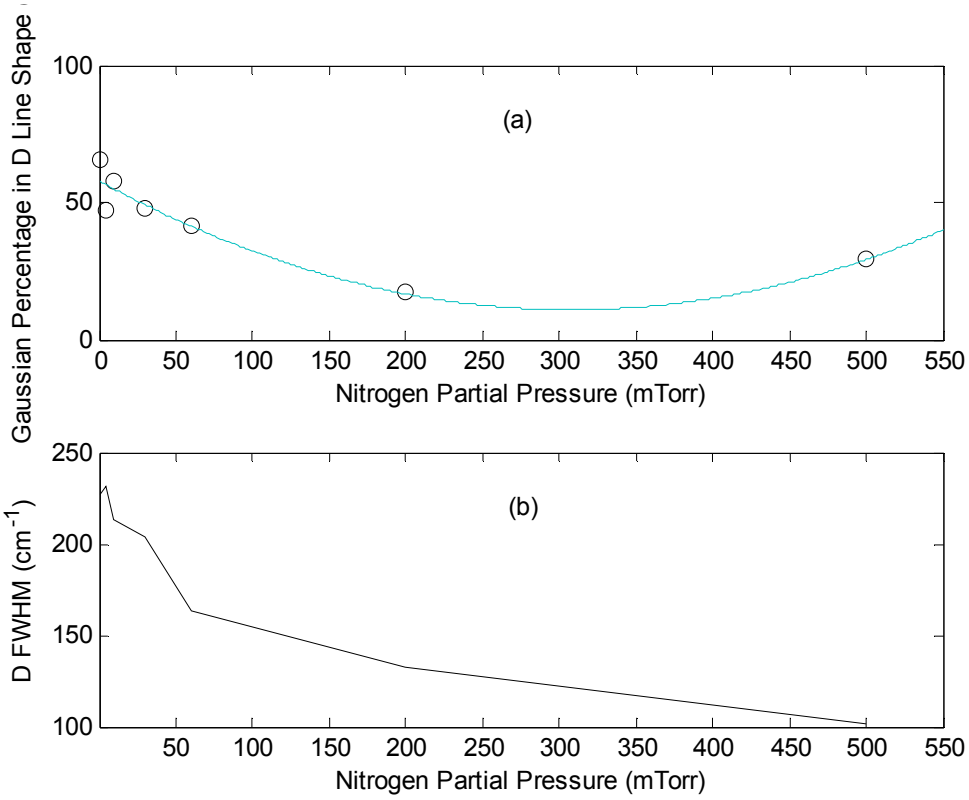

Figure 3.56 (a) Gaussian percentage in D line shape and (b) FWHM of D line as a function of NPP

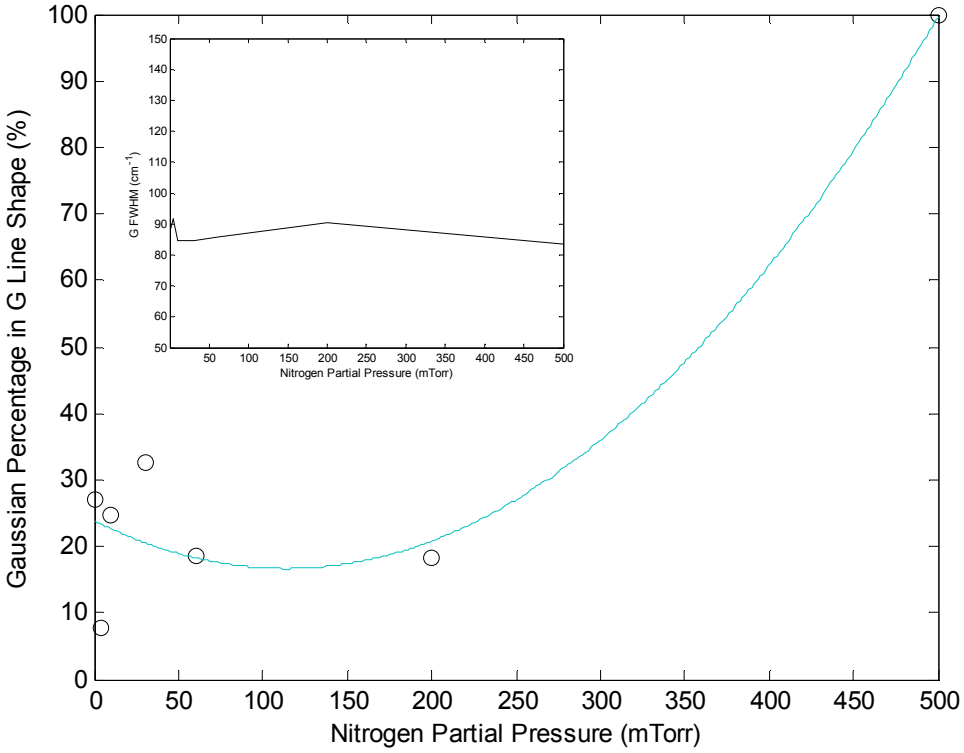

Figure 3.57 Gaussian percentage in G line shape. The inset shows the FWHM of G line as a function of NPP

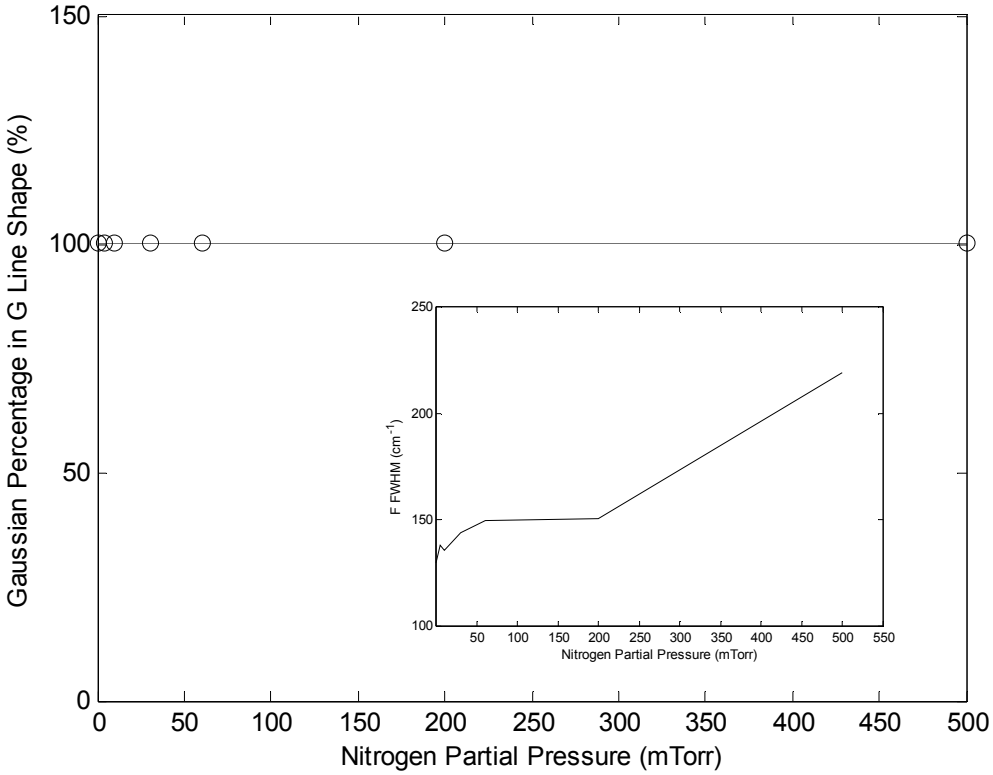

Figure 3.58 Gaussian percentage in F line shape. The inset shows the FWHM of F line as a function of NPP

Raman characteristics peak with Gaussian line shape represents less crystallinity as Gaussian line shape is broad in nature. Raman characteristics peak with Lorentzian line shape represents better crystallinity as Lorentzian line shape is steep. Each of the peaks is fitted by a line shape which is combination of Gaussian and Lorentzian line shape. The combination percentage is determined for least and random error.

Decrease in Gaussian percentage indicates the improvement in crystal quality. It is found and shown in figure 3.56 that Gaussian percentage in D line shape decreases with NPP and after certain NPP Gaussian percentage increases with NPP. Again the G line shape is best fitted with Gaussian percentage as shown in figure 3.57. G line shape also follows the pattern as D line shape. F line shape is always Gaussian which indicating less crystallinity of C_{60}.

The D FWHM is decreasing with increase in N_2 content. G FWHM ranges around 83-91 cm^{-1}. And F FWHM is always increasing with NPP.

Correlating the Gaussian percentage in line shapes and FWHM of the line shapes, it can be concluded that the improvement in crystal occurs up to certain NPP and then at high NPP quality decreases. It may be interpreted like that the graphene sheet has initially disorder. With nitrogen incorporation disorders are passivated and better films are deposited. But as NPP increases considerably the laser energy is dissipated in nitrogen atoms and less disintegration of C_{60} occurs and breaking the bonds in C_{60} nitrogen helps the polymerization of C_{60}.

3.8 Discussions

Analyzing the RS of the carboneous films, three peaks are found. G line position varies more in a-C and variation is proportional to disorder. The decreasing behavior is due to N_2 incorporation because N_2 incorporation causes G position to decrease which indicates more crystalline structure. The less dispersion for the condition of 500 mTorr is 7 (+7 cm^{-1}) indicates N_2 incorporation makes deposited film more disorder less. D peak position is upshifted from initial value and then downshifted. Its variation range is 1335.4~1362.2 cm^{-1}. The actual value of D line in polycrystalline graphite is 1355 cm^{-1}. D line position for the first 2 NPP conditions has higher value than this actual value but for rest of the conditions has lower value. The upshifting and downshifting value of D line position indicate decrease in the bond angle disorder and change in the bonding respectively. This is true because polymerization increases with the increase of N_2 pressure means sp^3 content is increasing and more sp^2 bond is breaking to form the bond among fullerene molecule with single bond. The F (fullerene) line position is also decreasing and decreases finally for the highest NPP condition which is located at 1500 cm^{-1}. Since $A_g(2)$ mode of C_{60} is located at 1469 cm^{-1}. Decreasing of F line position is indication of more fullerenes like structure with nitrogen. I_d/I_g ratio is one of the important parameter and together with G peak position we can explain the bond arrangement. Since I_d/I_g ratio is the ratio of momentum of nonconserving to conserving phonons it

will decrease for more crystallites because in large crystal momentum is conserved. High N_2 pressure causes C_{60} content to increase as I_d/I_f is decreasing and I_f/I_g is increasing with N_2 incorporation. This indicates when N_2 content is low we get more damaged C_{60} so graphene like structure. Because D, G peaks predominates over the fullerene peak. But with more N_2 incorporation more presence of C_{60} is found maintaining its graphitic form (as D and G peaks are still there). FWHM variation of individual peak as a function of NPP reveals that D- FWHM decreases, F- FWHM increases and G- FWHM is quite irregular. According to Ferrari et al. FWHM is proportional to disorder. The decreasing nature of D-FWHM reveals that N_2 incorporation decreases bond angle disorder and increases crystallites. But F-FWHM increases continuously from 129.84 cm^{-1} to 219.1 cm^{-1}, which is an indication of bonds like C_{60}-N-C_{60} as $A_g(2)$ mode softens. Formation of intermolecular polymeric bonds between C_{60} molecules with nitrogen incorporation moves away some of the electrons from the intermolecular double bonds and hence soften the $A_g(2)$ modes and broadens it.

Analyzing the optical behavior of the carbon films it is found that the Tauc parameter increases with the increase of NPP which is an indication of less disorder in the films as the Tauc parameter, B, is a measure of the steepness of the band tail (Urbach region) density of states. But in higher NPP, Tauc parameter decreases due to the structural modification of the films.

It is found from the calculated value of the optical gap for deposited film in nitrogen free environment is 0.9833. From the optical absorption behavior analyses results it is obtained that the optical gap initially increases with NPP up to .5 mTorr due to passivation of the dangling in the carbon film. After that, optical gap of the deposited films decline for NPP of 4.2 mTorr due to donor states created in the forbidden energy gap. Then again, optical gap is increases upto 80 mTorr. And after that it decreases with increase in NPP. At higher NPP the structure of the carbon film drastically changed so the optical gap increases and then again nitrogen incorporation in the carbon films decreases band gap.

From the J-V characteristics of the carbon films from camphoric target it is obtained that the current density is maximum ~9 mA/cm^{-2} at 0.4 V. But from figure 3.54 the

current density is maximum ~ 35 mA/cm^{-2} at 0.4 V. So there is fourfold improvement in the J-V characteristics. High energetic pulsed laser causes semiconducting film from C_{60} target which retains crystalline graphite structure. From the comparison between the carbon films it can be concluded that such improved quality of film proves that C_{60} can be used as a better target material instead of graphite or camphor for semiconducting/optoelectronic applications.

Since the eye is only sensitive to light energy $h\nu \geq 1.8$ eV (~ 0.7 μm), the semiconductors of interest for optoelectronic application must have energy band gaps larger than this limit. The films here have band gap in the range of optical device application in low NPP and high NPP. Again, optical and Raman spectra analyses shows that the films have less disorder. Carbon films are inexpensive. So, semiconducting films from C_{60} target can be used as low cost and improved alternative materials for optoelectronic devices. As J-V characteristics shows good performance, the films is can be used for electronic application. The films can also be used for solar cell application.

CHAPTER 4

CONCLUSIONS AND SUGGESTIONS FOR FUTURE WORKS

4.1 Conclusions

In this work Raman Spectra of nanostructured semiconducting polymeric carbonaceous films deposited from fullerene C_{60} precursor by pulsed laser deposition technique at various nitrogen partial pressures are investigated. The disappearance of some characteristic C_{60} peaks along with existence of few peaks are observed in the Raman spectra indicate structural modification. However, the deposited film retains the crystalline form of graphene sheet therefore, possibly suitable for electronics applications compared to that of the typical amorphous carbon.

The Raman spectra are deconvoluted here with the help of curve fitting technique. The deconvolution outcome is 3 different bands located at 1357.4 cm^{-1}, 1529.3 cm-^{1} and 1592.1 cm^{-1} for the sample that has no N_2 content. The investigation shows that the band located at 1357.4 cm^{-1} is nothing but the peak named D peak. Where D denotes disorder and it is the characteristic peak of graphite. The second peak evolutes due to the polymerized C_{60} but it shifts from the original position of C_{60} (at 1469 cm^{-1}) and its spectrum is quite broad in nature. The third deconvoluted peak placed at 1592.1 cm^{-1} is G (Graphite) peak. G peak (1580 cm^{-1}) is the characteristic peak of single crystalline graphite. The upshifting from this peak position to1592.1 cm^{-1} indicates a form like graphene like structure. The downshifting of D peak (from its actual value) indicates the presence of sp^3 C. The D, G and F line position all decrease for the final sample where nitrogen content is highest. The decrease in the F line position and increasing nature of F- FWHM indicate the presence of C_{60}

nature of the film. The decreasing nature of I_d/ I_g with NPP indicates the decrease in disorder. At higher NPP increase of I_d/ I_g indicates disorder increase. The other two ratios I_d/ I_f (decreasing with NPP) and I_f/ I_g (decreasing with NPP) represents the increasing feature of the polymeric C_{60} carbon. Where initially D and G peaks dominate over the fullerene peak later with the incorporation of N_2 these two peaks decreases with respect to fullerene peak. That's why I_d/ I_g ratio is decreasing and I_d/ I_f is decreasing and I_f/ I_g is increasing. The D- FWHM decreases, F- FWHM increases. Raman characteristics peak with Lorentzian line shape represents better crystallinity as Lorentzian line shape is steep. Lorentzian percentage in D line shape increases with NPP and after certain NPP Lorentzian percentage increases with NPP. G line shape has the same pattern.

Optical gap initially increases with NPP from 0.9833 to 2.528 eV as nitrogen atoms pacify the open bond and dangling bonds due to which band tail states are created. Then with increasing NPP nitrogen create the donor states in the forbidden gap resulting in optical decrease to 1.171 eV. At higher NPP optical gap shows increase up to 2.786 eV and then decreases to 2.1 eV. Tauc parameter increases up to 540 $cm^{-1/2}e^{1/2}V^{1/2}$ at 80 mTorr which is an indication of decreasing disorder. At higher NPP Tauc parameter decreases due to structural modification from films in lower NPP. The optical gap of the films rests in the optoelectronic application range. The performance i.e. the dark J-V characteristics of C_{60}/p-silicon heterostructured solar cell improves due to N_2 incorporation. The current density versus voltage characteristics of the carbon films deposited from C_{60} target shows improvement than those from carbon films from graphite and camphor target. The diode quality factor shows better characteristics in the conduction region than those produced from camphoric and graphitic films.

Optimal N_2 incorporation makes the film doped with nitrogen though retains some graphite form. Improved structure, optical behavior and dark J-V characteristics make the carbon films suitable for optoelectronic and other electronic device application.

4.2 Suggestions for Future Works

A more detail analysis to prove that nitrogen incorporation in the pulsed laser deposition process causes the carboneous film to structurally modify can be done with the help of AFM image. The C-V characteristics of the carboneous can be studied to understand the doping by nitrogen in the films. Illuminated J-V characteristics can be studied for finding scope in solar application. A detailed study of HEMT structure using the carbon films can be done to find application in high speed devices.

References

[1] Robertson, J., "Diamond-like amorphous carbon", *Materials Science and Engineering Reports*, Vol-37, pp 129-281, 2002.

[2] Kwok, S.C.H., Wang, J. and Chu, P.K., "Surface energy, wettability, and blood compatibility phosphorus doped diamond-like carbon films", *Diamond Related Materials*, Vol-14, pp 78-85, 2005.

[3] Rusop, M., Tian, X.M., Mominuzzaman, S.M., Soga, T., Jimbo, T. and Umeno, M., "Photoelectrical properties of pulsed laser deposited boron doped p-carbon/n-silicon and phosphorus doped n-carbon/p-silicon heterojunction solar cells", *Solar Energy*, Vol-78, pp 406-415, 2005.

[4] Kroto, H.W., Heath, J., O'Brien, S.C. Curl, R.F. and Smalley, R.E., "C_{60}: Buckminsterfullerene", *Nature*, Vol-318, pp 162-163, 1985.

[5] Kratschmer, W., Lamb, L.D., Fostiropoulos, K. and Huffman, D.R., "Solid C_{60}: a new form of carbon", *Nature*, Vol-347, pp 354-358, 1990.

[6] Milne, W.I., "Electronic devices from diamond-like carbon", *Semiconductor Science and Technology*, Vol-18, No. 3, pp 81-86, 2003.

[7] Nagano, T., Kusai, H., Ochi, K., Ohta, T., Imai, K., Kubozono, Y. and Fujiwara, A., "Fabrication of field-effect transistor devices with fullerene related materials", *Physica Status Solidi (B)*, Vol-243, No. 13, pp 3021-3024, 2006.

[8] Kojima, N., Sugiura, Y. and Yamaguchi, M., "Optical properties of C_{60}/a-C superlattice structures for solar cell applications", *Solar Energy Materials and Solar Cells*, Vol-90, No. 18-19, pp 3394-3398, 2006.

[9] Narayanan, K.L., Yamaguchi, M., "Phosphorous ion implantation in C_{60} for the photovoltaic applications", *Journal of Applied Physics*, Vol-89, No.12, pp 8331-8335, 2001.

[10] Cheyns, D., Gommans, H., Odijk, M., Poortmans, J. and Heremans, P., "Stacked organic solar cells based on pentacene and C_{60}", *Solar Energy Materials Solar Cells*, Vol-91, No. 5, pp 399-404, 2007.

[11] Janssen, A.G.F., Riedl, T., Hamwi, S. Johannes, H.-H. and Kowalsky, W., "Highly efficient organic tandem solar cells using an improved connecting architecture", *Applied Physics Letter*, Vol-91, No. 073519, 2007.

[12] Jimbo, T., Soga, T. and Hayashi, Y., "Development of new materials for solar cells in Nagoya Institute of Technology", *Science and Technology of advanced Materials*, Vol-6, No. 1, pp 27-33, 2005.

[13] Marques, L., Mezouar, M., Hodeau, J.-L., Nunez-Regueiro, M., Serebryanaya N.R. and Ivdenko V.A., *et al.*, "Debye-Scherrer Ellipses" from 3D Fullerene Polymers: An Anisotropic Pressure Memory Signature", *Science*, Vol-283, pp 1720-1723, 1999.

[14] Chernozatonskii, L.A., Serebryanaya, N.R. and Mavrin B.N., "The superhard crystalline three-dimensional polymerized C_{60} phase", *Chemical Physics Letters*, Vol-316, No. 3-4, pp 199-204, 2000.

[15] Makarova, T.L., Sundqvist, B., Hohne, R., Esquinazl, P., Kopelevich, Y. and Scharff, P. *et al.*, "Magnetic carbon", *Nature*, Vol-413, pp 716-718, 2001.

[16] Karachevtsev, V.A., Mateichenko, P.V., Nedbailo, N.Yu, Peschanskii, A.V., Plokhotnichenko, A.M., Vovk, O.M., Zubarev, E. N. and Rao, A.M., "Effective photopolymerization of C_{60} films under simultaneous deposition and UV light irradiation: Spectroscopy and morphology study", *Carbon*, Vol-42, No. 10, pp 2091-2098, 2004.

[17] Bejwa, N., Dharamvir, K., Jindal, V.K., Ingale, A., Avasthi, D.K., Kumar, R. and Tripathi, A., "Swift heavy ion induced modification of C_{60} thin films", Journal of Applied Physics, Vol-94, No. 1, pp 326-333, 2003 and references therein.

[18] Khan, A., Kojima, N., Yamaguchi, M., Narayanan, K.L. and Goetzberger, O., "High-energy electron irradiation effects in C_{60} films", *Journal of Applied Physics*, Vol-87, No. 9, pp 4620-4622, 2000.

[19] Lotha, S., Ingale, A., Avasthi, D.K., Mittal, V.K., Mishra, S., Rustagi, K.C., Gupta, A., Kulkarni, V.N. and Khathing, D.T., "Effect of heavy ion irradiation on C_{60}", *Solid State Communications*, Vol-111, No. 1, pp 55-60, 1999.

[20] Narayanan, K.L., Yamaguchi, M., Dharmarasu, N., Kojima, N. and Kanjilal, D., "Low energy ion implantation and high energy heavy ion irradiation in C_{60} films", *Nuclear Instruments and Methods in Physics Research B*, Vol-178, No. 1-4, pp 301-304, 2001.

[21] Alvarez-Zauco, E., Sobral, H., Basiuk, E.V., Saniger-Blesa, J.M. and Villagran-Muniz, M., "Polymerization of C_{60} fullerene thin films by UV pulsed laser irradiation", *Applied Surface Science*, Vol-248, pp 243-247, 2005.

[22] Mominuzzaman, S.M., Chandrasekaran, N., Soga, T. and Jimbo, T., "Polymeric semiconducting carbon from fullerene by pulsed laser ablation", *Diamond and Related Materials*, Vol-17, No. 4-5, pp 641-645, 2008.

[23] Dmitruk, N.L., Borkovskaya, O. Yu, Mamontova, I.B., Kondratenko, O.S., Naumenko, D.O., Basiuk, E.V. and Alvarez-Zauco, E., "Optical and electrical characterization of chemically and photopolymerized C_{60} thin films on silicon substrates", *Thin Solid Films*, Vol-515, No. 19, pp 7716-7720, 2007.

[24] Voevodin, A.A., Jones, J.G., Zabinski, J.S., Czigány, Zs. and Hultman, L., "Growth and structure of fullerene-like CN_x thin films produced by pulsed laser ablation of graphite in nitrogen", *Journal of Applied Physics*, Vol-92, No. 9, pp 4890-4898, 2002.

[25] Stimpel, T., Schraufstetter, M., Baumgartner, H. and Eisele, I., "STM studies of C_{60} on a Si(111):B surface phase", *Materials Science and Engineering B*, Vol-89, pp 394-398, 2002.

[26] Dharmarasu, N., Sakai, T., Kojima, N., Yamaguchi, M., Ohshita, Y. and Narayanan K. L., "Electrical and optical properties of the B^+ and P^+ implanted C_{60} thin films", *Journal of Applied Physics*, Vol-89, No. 1, pp 318-322, 2001.

[27] Abrasonis, G., Gago, R., Vinnichenko, M., Kreissig, U., Kolitsch, A. and Moller, W., "Sixfold ring clustering in sp^2-dominated carbon and carbon nitride thin films: A Raman spectroscopy study", *Physics Review B*, Vol-73, No. 125427, 2006.

[28] Roy, D., Chhowalla, M., Hellgren, N., Clyne, T.W. and Amaratunga, G. A. J., "Probing carbon nanoparticles in CN_x thin films using Raman spectroscopy", *Physics Review B*, Vol-70, No. 035406, 2004.

[29] Kleinsorge, B., Ferrari, A. C., Robertson, J. and Mline, W. I., "Influence of nitrogen and temperature on the deposition of tetrahedrally bonded amorphous carbon", *Journal of Applied Physics*, Vol-88, No. 2, pp 1149-1157, 2000.

[30] Koidl, P., Wagner, C., Discheler, B., Wagner, J. and Ramsteiner, M., "Plasma deposition, properties and structure of amorphous hydrogenated carbon films", *Material Science Forum*, Vol-52, pp 41-70, 1990.

[31] Ferrari, A.C., Libassi, A., Tanner, B.K., Stolojan, V., Yuan, J., Brown, L.M., Rodil, S.E., Kleinsorge, B. and Robertson, J., "Density, sp^3 fraction, and cross-sectional structure of amorphous carbon films determined by x-ray reflectivity and electron energy-loss spectroscopy", *Physics Review B*, Vol-62, No. 16, pp 11089-11103, 2000.

[32] Morrison, N.A., Rodil, S.E., Ferrari, A.C., Robertson, J. and Milne, W.I., "High rate deposition of ta-C:H using an electron cyclotron wave resonance plasma source", *Thin Solid Films*, Vol-337, No. 1-2, pp 71-73, 1999.

[33] Jacob W. and Moller, W., "On the structure of thin hydrocarbon films", *Applied Physics Letter*, Vol-63, No. 13, pp 1771-73, 1993.

[34] Fuller R. B., 1984, "The Artifacts of R. Buckminster Fuller: A Comprehensive Collection of His Designs and Drawings", ed. W Marlin. New York: Garland.

[35] Curl R.F. and Smalley R.E., "Probing C_{60}", *Science*, Vol-242, No. 4881, pp 1017-1022, 1988.

[36] Haddon R.C., Hebard A.F., Rosseinsky M.J., Murphy D.W. and Duclos S.J., *et al.*, "Conducting films of C_{60} and C_{70} by alkali-metal doping", *Nature*, Vol-350, pp 320-322, 1991.

[37] Hebard A.F., Rosseinsky M. J., Haddon R.C., Murphy D.W. and Glarum S.H. *et al.*, "Superconductivity at 18 K in potassium-doped C_{60}", *Nature*, Vol-350, pp 600-601, 1991.

[38] Hebard A.F., "Superconductivity in Doped Fullerenes", *Physics Today*, Vol-45, No. 11, pp 26-32, 1992.

[39] Palstra, T.T.M., Zhou, O., lwasa, Y., Sulewski, P., Fleming, R.M. and Zegarski, B., "Superconductivity at 40K in cesium doped C_{60}", *Solid Stste Communications*, Vol-93, No. 4, pp 327-330, 1995.

[40] Hebard A.F., "Buckminsterfullerene", *Annual Review of Materials Science*, Vol-23, pp 159-191, 1993.

[41] Tomanek, D., Schluter, M.A., "Growth regimes of carbon clusters", *Physics Review Letters*, Vol-67, No. 17, pp 2331-2334, 1991.

[42] Lenosky, T., Gonze, X., Teter, M. and Elser, V., "Energetics of negatively curved graphitic carbon", *Nature*, Vol-355, No. 6358, pp 333-335, 1992.

[43] Regueiro, M. N., Monceau, P. and Hodeau, J.-L., "Crushing C_{60} to diamond at room temperature", *Nature*, Vol-355, No. 6357, pp 237-239, 1992.

[44] Kratchmer, W., Lamb, L.D., Fostiropoulos, K. and Huffman, D.R., "Solid C_{60}: a new form of carbon", *Nature*, Vol-347, No. 6291, pp 354-358, 1990.

[45] Hebard, A.F., Haddon, R.C., Fleming, R.M. and Kortan, A.R., "Deposition and characterization of fullerene films", *Applied Physics Letters*, Vol-59, No. 17, pp 2109-2111, 199l.

[46] Fleming, R.M., Siegrist, T., Marsh, P.M., Hessen, B. and Kortan, A.R. *et al.*, *Material Research Society Sympozium*, Vol-206, pp 691-696, 1991.

[47] Meng, R.L., Ramirez, D., Jiang, X., Chow, P.C. and Diaz, C. *et al.*, "Growth of large, defect-free pure C_{60} single crystals", *Applied Physics Letters*, Vol-59, No. 26, pp 3402-3413, 1991.

[48] Abrefah, J., Olander, D.R., Balooch M. and Siekhaus W.J., "Vapor pressure of Buckminsterfullerene", *Applied Physics Letters*, Vol-60, No. 11, pp 1313-1314, 1992.

[49] Dresselhaus, M.S., Dresselhaus, G., "Fullerenes and Fullerene Derived Solids as Electronic Materials", *Annual Review of Materials Science*, Vol-25, pp 487-523, 1995.

[50] Taylor, R., Hare, J.P., Abdul-Sada, A.K. and Kroto, H.W., "Isolation, separation and characterisation of the fullerenes C_{60} and C_{70}: the third form of carbon", *Journal of Chemical Society Chemical Communication*, Vol-20, pp 1423-1425, 1990.

[51] Johnson, R.D., Meijer, G. and Bethune, D.S., "C_{60} has icosahedral symmetry", *Journal of American Chemical Society*, Vol-112, No.24, pp 8983-84, 1990.

[52] Dresselhaus, M.S., Dresselhaus, G. and Eklund, P.C., "Fullerenes", *Journal of Material Research*, Vol-8, No. 8, pp 2054-97, 1993.

[53] Dresselhaus, G., Dresselhaus, M.S. and Eklund, P.C., "Symmetry for lattice modes in C_{60} and alkali-metal-doped C_{60}", *Physics Review B*, Vol-45, No. 12, pp 6923-6930, 1992.

[54] Stephens, P.W., Mihaly, L., Lee, P.L., Whetten, R.L. and Huang, S.M. *et al.*, "Structure of single-phase superconducting K_3C_{60}", *Nature*, Vol-351, No. 6328, pp 632-634, 1991.

[55] Fischer, J.E., Heiney, P.A., McGhie, A.R., Romanow, W.J. and Denenstein, A.M. *et al.*, "Compressibility of Solid C_{60}", *Science*, Vol-252, No. 5010, pp 1288-1290, 1991.

[56] Fischer, J.E., Heiney, P.A. and Smith, A.B. III., "Solid-state chemistry of fullerene-based materials", *Accounts of Chemical Research*, Vol-25, No. 3, pp 112-118, 1992.

[57] Kortan, A.R., Kopylov, N., Glarum, S.H., Gyorgy, E.M. and Ramirez, A.P. *et al.*, "Superconductivity at 8.4 K in calcium-doped C_{60}", *Nature*, Vol-355, No. 6360, pp 529-532, 1992.

[58] David, W.F., Ibberson, R.M., Matthewman, J.C., Prassides, K. and Dennis, T.J.S. *et al.*, "Crystal structure and bonding of ordered C_{60}", *Nature*, Vol-353, No. 6340, pp 147-149, 1991.

[61] Woo, S.J., Lee, S.H., Kim, E., Lee, K.H. and Lee, Y.H. *et al.*, "Bulk modulus of the C_{60} molecule via the tight binding method", *Physics Letter A*, Vol-162, No. 6, pp 501-505, 1992.

[62] Fischer, J.E., Heiney, P.A., "Order and disorder in fullerene and fulleride solids", *Journal of Physics and Chemistry of Solids*, Vol-54, No. 12, pp 1725-1757, 1993.

[63] Saito, S., Oshiyama, A., "Electronic and geometric structures of C_{70}", *Physics Review B*, Vol-44, No. 20, pp 11532-11535, 1991

[64] Wang, L.S., Conceicao, J., Jin, C. and Smalley, R.E., "Threshold photodetachment of cold C^-_{60}", *Chemical Physics Letter*, Vol-182, No. 1, pp 5-11, 1991.

[65] de Vries, J., Steger, H., Kamke, B., Menzel, C. and Weisser, B. *et al.*, "Single-photon ionization of C_{60}- and C_{70}-fullerene with synchrotron radiation: determination of the ionization potential of C_{60}", *Chemcal Physics Letter*, Vol-188, No. 3-4, pp159-162, 1992.

[66] Steger, H., de Vries, J., Kamke, B., Kamke, W. and Drewello, T., "Direct double ionization of C_{60} and C_{70} fullerenes using synchrotron radiation", *Chemical Physics Letters*, Vol- 194, No. 4-6, pp 452-456, 1992.

[67] Heiney, P.A., Vaughan, G.B.M., Fischer, J.E., Coustel, N. and Cox, D. E. *et al.*, "Discontinuous volume change at the orientational-ordering transition in solid C_{60}", *Physics Review B*, Vol-45, No. 8, pp 4544-4547, 1992.

[68] Rao, A.M., Zhou, P., Wang, K.A., Hager, G.T. and Holden J.M. *et al.*, *Science*, Vol-259, pp 955-957, 1993.

[69] Dresselhaus, G., Dresselhaus, M.S. and Mavroides, J.G., "Spin-orbit interaction in graphite", *Carbon*, Vol-4, No. 3, pp 433-440, 1966.

[70] Shi, X.D., Kortan, A.R., Williams, J.M., Kini, A.M., Saval, B.M. and Chaikin, P.M., "Sound velocity and attenuation in single-crystal C_{60}", *Physics Review Letter*, Vol-68, No. 6, pp 827-830, 1992.

[71] Yu, R.C., Tea, N., Salamon, M.B., Lorens, D. and Malhotra, R., "Thermal conductivity of single crystal C_{60}", *Physics Review Letter*, Vol-68, No. 13, pp 2050-2053, 1992.

[72] Ren, S.L., Wang, Y., Rao, A.M., McRae, E. and Hager, G.T. *et al.*, "Ellipsometric determination of the optical constants of C_{60} (Buckminsterfullerene) films", *Applied Physics Letter*, Vol-59, No. 21, pp 2678-2680, 1991.

[73] Wang, Y., Holden, J.M., Rao, A.M., Lee, W.T. and Hager, G.T. *et al.*, "Interband dielectric function of C_{60} and M_6C_{60} (M=K,Rb,Cs)", *Physics Review B*, Vol-45, No. 26, pp 14396-14399, 1992.

[74] Diederich, F., Whetten, R.L., "Beyond C60: the higher fullerenes", *Accounts of Chemical Research*, Vol-25, No. 3, pp 119-126, 1992.

[75] Kikuchl, K., Nakahara, N., Wakabayashi, T., Suzuki, T.S. and Shiramaru, T. *et al.*, "NMR characterization of isomers of C_{78}, C_{82} and C_{84} fullerenes", *Nature*, Vol-357, No. 6374, pp 142-145, 1992.

[76] Manolopoulos, D.E., Fowler, P.W., "Structural proposals for endohedral metal—fullerene complexes", *Chemical Physics Letter*, Vol-187, No. 1-2, pp 1-7, 1991.

[77] Fleming, R.M., Rosseinsky, M.J., Ramirez, A.P., Murphy, D.W. and Tully, J.C. *et al.*, "Preparation and structure of the alkali-metal fulleride A_4C_{60}", *Nature*, Vol-352, No. 6337, pp 701-703, 1991.

[78] Fleming, R.M., Ramirez, A.P., Rosseinsky, M.J., Murphy, D.W. and Haddon, R.C. *et al.*, "Relation of structure and superconducting transition temperatures in A_3C_{60}", *Nature*, Vol-352, No. 6338, pp 787-788, 1991.

[79] Heiney, P.A., Fischer, J.E., McGhie, A.R., Romanow, W.J. and Denenstein, A.M. *et al.*, "Orientational ordering transition in solid C_{60}", *Physics Review Letter*, Vol-66, No. 22, pp 2911-2914, 1991.

[79a] Heiney, P.A., Fischer, J.E., McGhie, A.R., Romanow, W.J. and Denenstein, A.M. *et al.*, "Heiney *et al*. reply", *Physics Review Letter*, Vol-67, No.11, pp 1468, 1991.

[80] Harris, A.B., Sachidanandam, R., "Orientational ordering of icosahedra in solid C_{60}", *Physics Review B*, Vol-46, No. 8, pp 4944-4957, 1992.

[81] Vaughan, G.B., Heiney, P.A., Fischer, J.E., Luzzi, D.E. and Ricketts-Foot, D.A. *et al.*, "Orientational Disorder in Solvent-Free Solid C_{70}", *Science*, Vol-254, No. 5036, pp 1350-1353, 1991.

[82] Verheijen, M.A., Meekes, H., Meijer, G., Bennema, P. and de Boer, J.L. *et al.*, "The structure of different phases of pure C_{70} crystals", *Chemical Physics*, Vol-166, No. 1-2, pp 287-297, 1992.

[83] Van Tendeloo, G., Amelinckx, S., Verheijen, M.A., van Loosdrecht, P.H.M. and Meijer, G., "New orientationally ordered low-temperature superstructure in high-purity C_{60}", *Physics Review Letter*, Vol-69, No. 7, pp 1065-68, 1992.

[84] Vaughan G. B. M., Heiney P. A., Cox D. E., McGhie A. R., Smith A. L., Strongin R. M., et al., *Chemcal Physics*, 1995.

[85] McGhie, A.R., Fischer, J.E., Stephens, P.W., Cappelletti, R.L. and Neumann, D.A. *et al.*, "Phase transitions in solid C_{70}: Supercooling, metastable phases, and impurity effect", *Physics Review B*, Vol-49, No. 18, pp 12614-12618, 1994.

[86] Armbruster, J.F., Romberg, H.A., Schweiss, P., Adelmann, P. and Knupfer, M. *et al.*, *Z. Physics B,* Vol-95, pp 469-474, 1994.

[87] Herzberg, G., "Molecular Spectra and Molecular Structure", Princeton: Van Nostrand, 1945.

[88] Saito, S., Oshiyama, A., "Cohesive mechanism and energy bands of solid C_{60}", *Physics Review Letter*, Vol-66, No.20, pp 2637-2640, 1991.

[89] Negri, F., Orlandi, G. and Zerbetto, F., "Low-lying electronic excited states of Buckminsterfullerene anions", *Journal of American Chemical Society*, Vol-114, No. 8, pp 2909-2913, 1992.

[90] Oshiyama, A., Saito, S., Hamada, N. and Miyamoto, Y., "Electronic structures of C_{60} fullerides and related materials", *Journal of Physics and Chemistry of Solids*, Vol-53, No. 11, pp 1457-1471, 1992

[91] Jost, M.B., Troullier, N., Poirier, D.M., Martins, J.L and Weaver, J.H. *et al.*, "Band dispersion and empty electronic states in solid C_{60}: Inverse photoemission and theory", *Physics Review B*, Vol-44, No. 4, pp 1966-1969, 1991.

[92] Weaver, J.H., "Fullerenes and fullerides: photoemission and scanning tunneling microscopy studies", *Accounts of Chemistry Research*, Vol-25, No. 3, pp 143-149, 1992.

[93] Benning, P.J., Poier, D.M., Ohno, T.R., Chen, Y. and Jost, M.B. *et al.*, "C_{60} and C_{70} fullerenes and potassium fullerides", *Physics Review B*, Vol-45, No. 12, pp 6899-6903, 1992.

[94] Ajie, H., Alvarez, M.M., Anz, S.J., Beck, R.D. and Diederich, F. *et al.*, "Characterization of the soluble all-carbon molecules C_{60} and C_{70}", *Journal of Physical Chemistry*, Vol-94, No.24, pp 8630-8633, 1990.

[95] Pichler, T., Matus, M., Korti, J. and Kuzmany, H., "Electronic transitions in K_xC_{60} ($0 \leqslant x \leqslant 6$) from *in situ* absorption spectroscopy", *Solid State Communications*, Vol-81, No. 10, pp 859-862, 1992.

[96] Sibley, S.P., Argentine, S.M. and Francis, A.H., "A photoluminescence study of C_{60} and C_{70}", *Chemical Physics Letter*, Vol-188, Vol-3-4, pp 187-193, 1992.

[97] Nakayama, A., Suzuki, K., Enoki, T., di Vittorio, S.L. and Dresselhaus, M.S. *et al.*, "Magnetic properties of activated carbon fibers", *Synthetic Metals*, vol-57, No. 1, pp 3736-3741, 1993.

[98] Matus, M., Kuzmany, H. and Sohmen, E., "Self-trapped polaron exciton in neutral fullerene C_{60}", *Physics Review Letter*, Vol-68, No. 18, pp 2822-2825, 1992.

[99] Wang, Y., Holden, J.M., Rao, A.M., Eklund, P.C. and Venkateswaran, U. *et al.*, "Optical absorption and photoluminescence in pristine and photopolymerized C_{60} solid films", *Physics Review B*, Vol-51, No. 7, pp 4547-4556, 1995.

[100] Sohmen, E., Fink, J., "Electron-energy-loss studies of Rb_xC_{60} and Rb_xC_{70} (x=0, 3, and 6)", *Physics Review B*, Vol-47, No. 21, pp 14532-14540, 1993.

[101] Birks, J.B., "Photophysics of Aromatic Molecules", Wiley, London, 970.

[102] Hung, R.R., Grabowski, J.J., "A precise determination of the triplet energy of carbon (C_{60}) by photoacoustic calorimetry", *Journal of Physical Chemistry*, Vol-95, No. 16, pp 6073-6075, 1991.

[103] Ebbesen, T.W., Tanigaki, K. and Kuroshima, S., "Excited-state properties of C_{60}", *Chemical Physics Letter*, Vol-181, No. 6, pp 501-504, 1991.

[104] Arbogast, J.W., Darmanyan, A.P., Foote, C.S., Rubin, Y. and Diederich, F.N. *et al.*, "Photophysical properties of sixty atom carbon molecule (C_{60})", *Journal of Physical Chemistry*, Vol-95, No.1, pp 11-12, 1991

[105] Tutt, L.W., Boggess, T.F., "A review of optical limiting mechanisms and devices using organics, fullerenes, semiconductors and other materials", *Progress in Quantum Electronics*, Vol-17, No. 4, pp 299-338, 1993.

[106] Tutt, L.W., Kost, A., "Optical limiting performance of C_{60} and C_{70} solutions", *Nature*, Vol-356, No. 6366, pp 225-26, 1992.

[107] Nissen, M.K., Wilson, S.M. and Thewalt, M.L.W., "Highly structured singlet oxygen photoluminescence from crystalline C_{60}", *Physics Review Letter*, Vol-69, No. 16, pp 2423-2426, 1992.

[108] Ruoff, R.S., Beach, D., Cuomo, J., McGuire, T., Whetten, R.L. and Diederich, F., "Confirmation of a vanishingly small ring-current magnetic susceptibility of icosahedral buckminsterfullerene", *Journal of Physical Chemistry*, Vol-95, No. 9, pp 3457-3459, 1991.

[109] Haddon, R.C., Schneemeyer, L.F., Waszczak, J.V., Glarum, S.H. and Tycko, R. *et al.*, "Experimental and theoretical determination of the magnetic susceptibility of C_{60} and C_{70}", *Nature*, Vol- 350, No. 6313, pp 46-47, 1991.

[110] Prato, M., Suzuki, T., Wudl, F., Lucchini, V. and Maggini, M., "Experimental evidence for segregated ring currents in C_{60}", *Journal of The American Chemical Society*, Vol-115, No. 17, pp 7876-7877, 1993.

[111] Allemand, P.M., Khemani, K.C., Koch, A., Wudl, F. and Holczer, K. *et al.*, "Organic Molecular Soft Ferromagnetism in a FullereneC_{60}", *Science*, Vol-253, No. 5017, pp 301-302, 1991.

[112] Tanaka, K., Okada, M., Okahara, K. and Yamabe, T., "Electronic structure of C_{70}", *Chemical Physics Letters*, Vol-202, No.5, pp 394-398, 1993.

[113] Wang, Y., "Photoconductivity of fullerene-doped polymers", *Nature*, Vol-356, No. 6370, pp 585-587, 1992.

[114] Orczyk, M.E., Swedek, B., Zieba, J., Prasad, P.N., "Nonlinear Optical Properties of Organic Materials", VII ed. GR Mohlmann, SPIE Opt. Eng. Press, Bellingham, WA, pp 166-177, 1994

[115] Tong, Q.Y., Eom, C.B., Gösele, U. and Hebard, A.F., "Materials with a Buried C_{60} Layer Produced by Direct Wafer Bonding", *Journal of Electrochemical Society*, Vol-141, No. 10, pp L137-L138, 1994.

[116] Sariciftci, N.S., Heeger, A.J., "Reversible, metastable, ultrafast photoinduced electron transfer from semiconducting polymers to Busckminsterfulllerene and in the corresponding donor/acceptor heterojunctions", *International Journal of Modern Physics B*, Vol- 8, No. 3, pp 237-74, 1994.

[117]Neugebauer, H., Loi, M.A., Winder, C., Sariciftci, N.S., Cerullo, G., Gouloumis, A., Vazquez, P. and Torres, T., "Photophysics and photovoltaic device properties of phthalocyanine–fullerene dyad:conjugated polymer mixtures", *Solar Energy Materials and Solar Cells*, Vol-83, No. 2-3, pp 201-209, 2004.

[118] Kojima, N., Sugiura, Y. and Yamaguchi, M., "Optical properties of C_{60}/a-C superlattice structures for solar cell applications", No. 18-19, *Solar Energy Materials and Solar Cells*, Vol-90, pp 3394-3398, 2006.

[119] Gardiner, D.J., "Practical Raman Spectroscopy", Springer-Verlag, 1989.

[120] Placzek G., *Hdb. der Radiologie*, Vol-VI., No. 2, pp 209, 1934.

[121] Khanna, R.K., D. D. Stranz, and B. Donn, "A spectroscopic study of intermediates in the condensation of refractory smokes: Matrix isolation experiments of SiO", *Journal of Chemical Physics*, Vol-74, No. 4, PP 2108, 1981.

[122]"Fake drugs caught inside the pack". BBC News. 2007-01-31. Retrieved 2008-12-08. http://news.bbc.co.uk/2/hi/health/6314287.stm

[123]"Irish Classic Is Still a Hit (in Calfskin, Not Paperback)" - New York Times. http://www.nytimes.com/2007/05/28/world/europe/28kells.html

[124]"Raman spectroscopy portends well for standoff explosives detection". Ben Vogel (29 August 2008). Jane's. http://www.janes.com/products/janes/defence-security-report.aspx?ID=1065927739

[125] Jeanmaire, D.L., van Duyne, R.P., "Surface Raman Electrochemistry Part I. Heterocyclic, Aromatic and Aliphatic Amines Adsorbed on the Anodized Silver Electrode", *Journal of Electroanalytical Chemistry*, Vol-84, No. 1, pp 1-20, 1977.

[126]Chao, R.S., Khanna, R.K. and Lippincott, E.R., "Theoretical and experimental resonance Raman intensities for the manganate ion", *Journal of Raman Spectroscopy*, Vol-3, No. 2-3, pp 121-131, 1975.

[127] Kneipp, K. *et al*., "Surface-enhanced non-linear Raman scattering at the single-molecule level", *Journal of Chemical Physics*, Vol-247, No. 1, pp 155-162, 1999.

[128] Matousek, P., Clark, I.P., Draper, E.R.C. *et al*., "Subsurface Probing in Diffusely Scattering Media Using Spatially Offset Raman Spectroscopy", *Applied Spectroscopy*, Vol-59, No.4, pp 393-400, 2005.

[129] Barron, L.D., Hecht, L., McColl, I.H. and Blanch, E.W., "Raman optical activity comes of age", *Molecular Physics,* Vol-102, No.8, pp 731-744, 2004.

[130] Schrader, B., Bergmann, G. and Fresenius, Z., *Analytical Chemistry*, pp 225-230, 1967.

[131] Matousek, P., Parker, A.W., "Bulk Raman Analysis of Pharmaceutical Tablets", *Applied Spectroscopy*, Vol-60, No. 12, pp 1353-1357, 2006.

[132] Matousek, P., Stone, N., "Prospects for the diagnosis of breast cancer by noninvasive probing of calcifications using transmission Raman spectroscopy", *Journal of Biomedical Optics*, Vol-12, No. 2, pp 024008, 2007.

[133] Lee, E.H., Hambree Jr., D.M., Rao, G.R. and Mansur, L.K., "Raman scattering from ion-implanted diamond, graphite, and polymers", *Physics Review B*, Vol-48, pp 15540-15551, No. 21, 1993.

[134] Ferrari, A.C. and Robertson, J., "Resonant Raman spectroscopy of disordered, amorphous, and diamondlike carbon", *Physics Review B*, Vol-64, No. 7, pp 075414, 2001 and references therein.

[135] Casiraghi, C., Ferrari, A.C. and Robertson, J., "Raman spectroscopy of hydrogenated amorphous carbons", *Physics Review B*, Vol-72, No. 8, pp 085401, 2005.

[136] Dong, Z.H., Zhou, P. Holden, J.M., Eklund, P.C., Dresselhaus, M.S. and Dresselhaus, G., "Observation of higher-order Raman modes in C_{60} films", *Physics Review B*, Vol-48, No. 4, pp 2862-2865, 1993.

[137] Wang, K.A., Rao, A.M., Eklund, P.C., Dresselhaus, M.S. and Dresselhaus, G., "Observation of higher-order infrared modes in solid C_{60} films", *Physics Review B*, Vol-48, No. 15, pp 11375-11380, 1993.

[138] Frum, C.I., Engleman Jr., R., Hedderich, H.G, Bernath, P.F., Lamb, L.B. and Huffman, D.R., "The infrared emission spectrum of gas-phase C_{60} (buckmisterfullerene)", *Chemical Physics Letter*, Vol-176, No. 6, pp 504-508, 1991.

[139] Eklund, P.C., Zhou, P., Wang, K.A., Dresselhaus, G. and Dresselhaus, M.S., "Optical phonon modes in solid and doped C_{60}", *Journal of Physics and Chemistry of Solids*, Vol-53, No. 11, pp 1391-1413, 1992.

[140] Chase, B., Herron, N. and Holler, E., "Vibrational spectroscopy of fullerenes (C_{60} and C_{70}). Temperature dependant studies", *Journal of Physical Chemistry*, Vol- 96, No. 11, pp 4262-4266, 1992.

[141] Dresselhaus, M.S., Dresselhaus, G. and Eklund, P.C., "Science of Fullerenes and Carbon Nanotubes", Academic Press, New York, 1996.

[142] Horoyski, P.J., Thewalt, M. L.W. and Anthony, T.R., "Raman Fine Structure in Crystalline C_{60}: The Effects of Merohedral Disorder, Isotopic Substitution, and Crystal Field", *Physics Review Letter*, Vol-74, No. 1, pp 194-197, 1995.

[143] Tycko, R., Dabbagh, G., Rosseinsky, M.J., Murphy, D.W., Ramirez, A.P. and Fleming, R.M., "Electronic properties of normal and superconducting alkali fullerides probed by ^{13}C nuclear magnetic resonance", *Physics Review Letter*, Vol-68, No. 12, pp 1912-1915, 1992.

[144] Copley, J.R.D., David, W.I.F. and Neumann, D.A., "Structure and dynamics of buckyballs", *Neutron News*, Vol-4, pp 20-28, 1993.

[145] van Loosdrecht, P.H.M., van Bentum, P.J.M. and Meijer, G., "Rotational ordering transition in single-crystal C_{60} studied by Raman spectroscopy", *Physics Review Letter*, Vol-68, No. 8, pp 1176-1179, 1992.

[146] Matus, M., Winter, J. and Kuzmany, H., "Electronic Properties of Fullerenes", *Springer series in Solid State Sciences*, Vol-117, pp 255-258, Springer, Berlin, 1993.

[147] Li, X.P., Lu, J. P. and Martin, R.M., "Ground-state structural and dynamical properties of solid C_{60} from an empirical intermolecular potential", *Physics Review B*, Vol-46, No. 7, pp 4301-4303, 1992.

[148] Jishi, R.A., Mirie, R.M. and Dresselhaus, M.S., "Force-constant model for the vibrational modes in C_{60}", *Physics Review B*, Vol-45, No. 23 pp 13685-13689, 1992.

[149] Quong, A.A., Pederson, M.R. and Feldman, J.L., "First principles determination of the interatomic force-constant tensor of the fullerene molecule", *Solid State Communications*, Vol-87, No. 6, pp 535-539, 1993.

[150] Feldman, J.L., Broughton, J.0., Boyer, L.L., Reich, D.E. and Kluge, M.D., "Intramolecular-force-constant model for C_{60}", *Physics Review B*, Vol-46, No. 19, pp 12731-12736, 1992.

[151] Guha, S., Menendez, J., Page, J.B., Adams, G.B., Spencer, G.S., Lehman, J.L., Giannozzi, P. and Baroni, S., "Isotopically resolved Raman spectra of C_{60}", *Physics Review Letter*, Vol-72, No. 21, pp 3359-3362, 1994.

[152] Dresselhaus, M.S., Dresselhaus, G. and Eklund, P.C., "Raman Scattering in Fullerenes", J*ournal of Raman Spectroscopy*, Vol-27, No. 3-4, pp 351-371, 1996.

[153] Fletcher, R., Powell, M.J.D., "A rapidly convergent descent method for minimization", *Computer Journal*, Vol-6, pp 163-168, 1963.

[154] Islam, M. S., "Spectral photoresponse of n-carbon/p-silicon heterostructure", M. Sc. Engineering Thesis, pp 48-54, Department of Electrical and Electronic Engineering, Bangladesh University of Engineering and Technology, 2002.

[155] Sze, S.M., "Physics of Semiconductor Devices", Wiley Eastern Limited, New Delhi, India, 1981.

[156] Dasgupta, D., Demichelis, F., Pirri, C. F. and Tagliaferro, A., "π bands and gap states from optical absorption and electron-spin-resonance studies on amorphous carbon and amorphous hydrogenated carbon films", *Physics Review B*, Vol-43, No. 3, pp 2131-2135, 1991.

[157] Moll, M.L., "The evaluation of the theory of the current-voltage characteristics of p-n junctions", *Proc IRE*, Vol-46, pp 1076, 1958.

[158] Rusop, M., Mominuzzaman, S.M., Soga, T., Jimbo, T. and Umeno, M., "Nitrogen doped n-type amorphous carbon films obtained by pulsed laser deposition with a natural camphor source target for solar cell applications", *Journal of Physics: Condensed Matter*, Vol-17, pp 1929-1946, 2005.

[162] Schwan, J., Ulrich, S., Batori, V., Ehrhardt, H. and Silva, S.R.P., "Raman spectroscopy on amorphous carbon films", *Journal of Applied Physics*, Vol-80, No. 1, pp 440-447, 1996 and references therein.

[163] Tamor, M. and Vassel, W., "Raman ''fingerprinting'' of amorphous carbon films", *Journal of Applied Physics*, Vol-76, No. 8, pp 3823-3830, 1994.

[164] Gussoni, M., Castiglioni, C. and Zerbi, G., "Spectroscopy of Advanced Materials", edited by Clark R.J. and Hester, R.E., Wiley, New York, pp251, 1991.

[165] Ehrenfreund, E., Vardeny, Z., Brafman, O. and Horovitz, B., "Amplitude and phase modes in *trans*-polyacetylene: Resonant Raman scattering and induced infrared activity", *Physics Review B*, Vol-36, No. 3, pp 1535-1553, 1987.

[166] Hernandez, V., Castiglioni, C., Del Zoppo, M. and Zerbi, G., "Confinement potential and π-electron delocalization in polyconjugated organic materials", *Physics Review B*, Vol-50, No. 14, pp 9815-9823, 1994.

[167] Kleinesorge, B., Ferrari, A.C., Robertson, J., Milne, W.I., Waidmann, S. and Hearne, S., "Bonding regimes of nitrogen in amorphous carbon", *Diamond Related Materials*, Vol-9, No. 3-6, pp 643, 2000.

[168] Gogotsi, Y.G., Yoshimura, M., "Formation of carbon films on carbides under hydrothermal conditions", *Nature*, Vol-367, No. 6464, pp 628-630, 1994

[169] Zhou, P., Rao, A.M., Wang, K., Robertson, J.D., Eloi, C., Meier, M.S., Ren, S.L., Bi, X.X., Eklund, P.C. and Dresselhaus, M.S., "Photo-assisted structural transition and oxygen diffusion in solid C_{60} films", *Applied Physics Letter*, Vol-60, No. 23, pp 2871-2873, 1992.

[170] Dzwilewski, A., Wågberg, T. and Edman, L., "C_{60} field-effect transistors: Effects of polymerization on electronic properties and device performance", *Physics Review B*, Vol-75, No. 7, pp 075203, 2007.

[171] Tunistra, F. and Koenig, J., "Raman Spectrum of Graphite", *Journal of Chemical Physics*, Vol-53, No. 3, pp 1126-1130, 1970.

[172] Dillon, R.O., Woollam, J.A. and Katkanant, V., "Use of Raman scattering to investigate disorder and crystallite formation in as-deposited and annealed carbon films", *Physics Review B*, Vol-29, No. 6, pp 3482-3489, 1984.

[173] Tauc, J., Grigorovici, R. and Vancu, A., "Optical Properties and Electronic Structure of Amorphous Germanium", Physics Status Solidi, Vol-15, No. 2, pp 527-537, 1966.

Appendix I

Rapidly Convergent Method for Minimization

This method is described by R. Flecher and M. J. D. Powell. It is a powerful iterative method for finding a local minimum of a function of several variables.

Notation

It is convenient to describe the method in terms of the Dirac bra-ket notation (Dirac, 1958) applied to real vectors. In this notation the column vector (x_1 , x_2 , ... x_n)is written as $|\, x \rangle$. The row vector with these same elements is denoted by $\langle x \,|$. The scalar product of $\langle x \,|$and $|\, x \rangle$ is written $\langle x \,|\, y \rangle$ and we may note that

$$\langle x \,|\, y \rangle \equiv \sum_i x_i y_i \equiv \sum_i x_i y_i \equiv \langle y \,|\, x \rangle$$

The construction $|\, x \rangle\langle y \,|$, however, denotes a linear operator with matrix elements $Dij = x_i y_j$ so that $|\, x \rangle\langle y \,| \neq \langle x \,|\, y \rangle$. A general linear operator or matrix will be denoted by a capital letter in bold type. It then follows that say $\boldsymbol{H}|\, x \rangle$ is a column vector, $\langle x \,|\, \boldsymbol{H}|$ is a row vector and $\langle x \,|\, \boldsymbol{H}|\, x \rangle$ is a scalar.

We reserve $f$to denote the function of interest, $|\, x \rangle$ to denote its arguments and $|\, g \rangle$ to denote its gradient. Hence the standard quadratic form in n dimensions

$$f = f_o + \sum_{i=1}^{n} a_i X_i + \frac{1}{2} \sum_{i=1}^{n} \sum_{j=1}^{n} G_{ij} X_i X_j$$

becomes in this notation

$$f = f_o + \langle a \,|\, x \rangle + \frac{1}{2} \langle x \,|\, \boldsymbol{G} \,|\, x \rangle \qquad (1)$$

and also

$$|\, g \rangle = |\, a \rangle + \boldsymbol{G}|\, x \rangle \qquad (2)$$

The method

If we consider the quadratic form (1) then, given the matrix $G_{ij} = \frac{\partial^2 f}{\partial xi \partial xj}$, we can calculate the displacement between the point $|\, x \rangle$ and the minimum $|\, x_o \rangle$ as

$$|\, x_o \rangle - |\, x \rangle = - G^{-1} |\, g \rangle \qquad (3)$$

In this method the matrix G^{-1} is not evaluated directly; instead a matrix H *is* used which may initially be chosen to be any positive definite symmetric matrix. This matrix is modified after the i^{th} iteration using the information gained by moving down the direction

$$|\, s^i \rangle = - H^i |\, g^i \rangle \qquad (4)$$

in accordance with (3). The modification is such that$|\, \sigma^i \rangle$, the step to the minimum down the line

$$|\, x \rangle = |\, x^i \rangle + \lambda |\, s^i \rangle$$

is effectively an eigenvector of the matrix $H^{i+1}\, G$. This ensures that as the procedure converges H tends to G^{-1} evaluated at the minimum.

It is convenient to take the unit matrix initially for H so that the first direction is down the line of steepest descent.

Let the current point be $|\, x^i \rangle$ with gradient $|\, g^i \rangle$ and matrix H^i. The iteration can then be stated as follows.

Set $|\, s^i \rangle = - H^i |\, g^i \rangle$

Obtain α^i such that $f(|\, x^i \rangle + \alpha^i |\, s^i \rangle)$ is a minimum with respect to λ along $|\, x^i \rangle + \lambda |\, s^i \rangle$ and $\alpha^i > 0$. We will prove that α^i can always be chosen to be positive.

Set $|\, \sigma^i \rangle = \alpha^i |\, s^i \rangle \qquad (5)$

Set $|\, x^{i+1} \rangle = |\, x^i \rangle + |\, \sigma^i \rangle$

Evaluate $f(|\, x^{i+1} \rangle)$ and $|\, g^{i+1} \rangle$ noting that $|\, g^{i+1} \rangle$ is orthogonal to $|\, \sigma^i \rangle$, that is

$$\langle\, \sigma^i |\, g^{i+1} \rangle = 0 \qquad (6)$$

Set $|\, y^i \rangle = |\, g^{i+1} \rangle - |\, g^i \rangle$

Set $H^{i+1} = H^i + A^i + B^i \qquad (7)$

Where $A^i = \frac{|\, \sigma i \rangle \langle\, \sigma i\, |}{\langle\, \sigma i\, | y i \rangle}$

$$B^i = \frac{-Hi|yi\rangle\langle yi|Hi}{\langle yi|Hi|yi\rangle}$$

Set $i = i + 1$ and repeat.

There are two obvious and very useful ways of terminating the procedure, and they arise because $|s^i\rangle$ tends to the correction to $|x^i\rangle$. One is to stop when the predicted absolute distance from the minimum $\langle s^i|s^i\rangle^{1/2}$ is less than a prescribed amount, and the other is to

finish when every component of $|s^i\rangle$ is less than a prescribed accuracy. Two additional safeguards have been found necessary in automatic computer programs. The first is to work through at least n (the number of variables) iterations, and the second is to apply the tests to $|\sigma^i\rangle$ as well as to $|s^i\rangle$.

The method of obtaining the minimum along a line is not central to the theory. The suggested procedure is given in the later section.

The minimum on a line

A simple algorithm is given for estimating the parameter α^i. A point $|y^i\rangle$ is chosen on $|x^i\rangle + \lambda|s^i\rangle$ with $\lambda > 0$. Let f_x, $|g_x\rangle$, f_y and $|g_y\rangle$ denote the values of the function and gradient at the points $|x^i\rangle$ and $|y^i\rangle$. Then an estimate of α^i can be formed by interpolating cubically, using the function values f_x and f_y and the components of the gradients along $|s^i\rangle$.

This is given by

$$\frac{\alpha i}{\lambda} = 1 - \frac{\langle gy|si\rangle + w - z}{\langle gy|si\rangle - \langle gx|si\rangle + 2w}$$

where $w = (z^2 - \langle g_x|s^i\rangle\langle g_y|s^i\rangle)^{1/2}$

and $z = \frac{3}{\lambda}(f_x - f_y) + \langle g_x|s^i\rangle + \langle g_y|s^i\rangle$.

A suitable choice of the point $|y^i\rangle$ is given by $|y^i\rangle = |x^i\rangle + \lambda|s^i\rangle$ where

$$\eta = \text{MINIMUM OF}\{1, \frac{-2(fx - fo)}{\langle gx|si\rangle}\}$$

f_o is the predicted lower bound f (| x ›), for example zero in least-squares calculations. This value of η ensures that the choice of | y^i› is reasonable.

It is necessary to check that f (| x^i› + α^i | s^i ›) is less than both f_x and f_y. If it is not, the interpolation must be repeated over a smaller range. Davidon suggests one should ensure that the minimum is located between | x^i› and | y^i› by testing the sign of ‹ g_Y | s^i › and comparing f_x and f_y before interpolating. Extensive details of this stage can be found in Davidon's report.

Appendix II

Data of the Fitted Curve of Raman Spectra

INTENSITY PEAK TABLE

	D-peak	F-peak	G-peak
Nitrogen Free	2.5254	0.9333	2.8048
4 mTorr NPP	1.1266	0.6260	1.0810
10 mTorr NPP	1.8584	0.8821	1.9946
30 mTorr NPP	1.3291	0.6112	1.4305
60 mTorr NPP	0.4187	0.2273	0.4410
200 mTorr NPP	0.2512	0.1363	0.2542
500 mTorr NPP	0.0873	0.0816	0.0843

POSITION TABLE

	D-peak	F-peak	G-peak
Nitrogen Free	1357.4	1529.3	1592.1
4 mTorr NPP	1362.2	1537.9	1600.6
10 mTorr NPP	1349.5	1525.6	1593.3
30 mTorr NPP	1345.7	1516.2	1592.0
60 mTorr NPP	1339.5	1508.1	1591.7
200 mTorr NPP	1340.4	1503.7	1591.6
500 mTorr NPP	1335.4	1503.1	1587.2

FWHM TABLE

	D-peak	F-peak	G-peak
Nitrogen Free	227.2200	129.8400	88.1100
4 mTorr NPP	231.8600	137.9500	91.5800
10 mTorr NPP	213.3100	135.6300	84.6300
30 mTorr NPP	204.0300	143.7500	84.6300
60 mTorr NPP	163.4600	149.5500	85.7900
200 mTorr NPP	132.1600	150.7000	90.4300
500 mTorr NPP	102.0100	219.1000	83.4700

INTEGRATED AREA RATIO TABLE

	I_d/I_g	I_d/I_f	I_f/I_g
Nitrogen Free	1.9620	5.0633	0.3875
4 mTorr NPP	2.1687	3.3126	0.6547
10 mTorr NPP	2.0098	3.6020	0.5580
30 mTorr NPP	1.9977	3.4533	0.5785
60 mTorr NPP	1.5841	2.3177	0.6835
200 mTorr NPP	1.3926	2.0308	0.6858
500 mTorr NPP	1.5634	0.5615	2.7843

GAUSSIAN PERCENTAGE TABLE

	D-peak	F-peak	G-peak
Nitrogen Free	0.6585	1.0000	0.2718
4 mTorr NPP	0.4731	1.0000	0.0776
10 mTorr NPP	0.5749	1.0000	0.2477
30 mTorr NPP	0.4754	1.0000	0.3248
60 mTorr NPP	0.4128	1.0000	0.1869
200 mTorr NPP	0.1711	1.0000	0.1818
500 mTorr NPP	0.2915	1.0000	1.0000

Declaration

It is hereby declared that this thesis or any part of it has not been submitted elsewhere for the award of any degree.

Signature of the candidate

_____

Ahmed Zubair

Dedication

To My Parents

Contents

List of Figures

List of Tables

Acknowledgements

I wish to offer my heartiest gratitude and profound respect to my thesis supervisor Dr. Sharif Mohammad Mominuzzaman, Professor, Department of Electrical and Electronic Engineering (EEE), Bangladesh University of Engineering and Technology (BUET), Bangladesh for giving me the opportunity to work with him and for his continuous guidance, suggestions and wholehearted supervision throughout the progress of this work. I am indebted to him for acquainting me with the world of advanced research.

I am grateful to the Head of Department, Electrical and Electronic Engineering (EEE), Bangladesh University of Engineering and Technology (BUET) for giving me permission to use the laboratory and other facilities of the department. I am grateful to my family and friends for their encouragement in my study. Finally, I am grateful to Almighty Allah for giving me strength and courage to complete the work.